Calcification & Fibrous Tissue Characteristics in Atherosclerotic Plaques

A Combined Analysis and Modeling Approach

Bas Vis

Technische Universiteit Delft

TU Delft

Erasmus MC
University Medical Center Rotterdam

Calcification & Fibrous Tissue Characteristics in Atherosclerotic Plaques

A Combined Analysis and Modeling Approach

by

Bas Vis

to obtain the degree of

Master of Science

in

Biomedical Engineering
- Biomaterials and Tissue Biomechanics -

at the Delft University of Technology,
to be defended publicly on Tuesday, February 19, 2019 at 11:00 AM.

Student number:	1527215	
Thesis committee:	Prof. dr. ir. A. A. Zadpoor,	TU Delft
	Dr. ir. J. Zhou,	TU Delft
	Dr. ir. M. K. Ghatkesar,	TU Delft
	Dr. ir. D. H. Plettenburg,	TU Delft
	Dr. ir. A. C. Akyildiz,	Eramus MC

This thesis is confidential and cannot be made public until February 19, 2020.

TU Delft

Erasmus MC
University Medical Center Rotterdam

Preface

All good things come to an end, and so does this great time I had during my master's programme in BioMedical Engineering. Going back to school after years of steady work is not particularly easy, but in the end, all I can look back at are the invaluable things I learned, and the great time I had while doing it. The second year of the master was dedicated to an internship, literature survey and graduation project, which I all performed at Erasmus Medical Center. For 16 months I was a guest at the Biomechanics Lab of the Biomedical Engineering Department, where I was welcomed as one of their own.

For this great experience I want to thank Ali Akyildiz in the first place, for your daily supervision, inexhaustive support, scientific input and frequent brainstorming sessions. Without your help this thesis would not be possible! Next I want to thank Frank Gijsen, for your expert opinions and invaluable insights during the many progress meetings we had. I also want to thank Hilary Barrett for sharing your knowledge on calcification mechanics and morphology. Astrid Moerman & Kim van Gaalen, thank you both for kindly sharing your histology datasets and providing me with the knowlegde to analyze them! Thank you Jie Zhou and Amir Zadpoor for reading and commenting on my reports.

Natuurlijk wil ik ook graag de mensen die dicht bij mij stonden tijdens deze intensieve periode en me motiveerden en steunden benoemen. Nienke, pa en ma, bedankt voor jullie mentale steun en inspiratie om deze master te volgen en tot een goed einde te brengen!

Bas Vis
Krimpen aan de Lek, January 2019

Abstract

Atherosclerotic plaque rupture is the main cause of acute myocardial infarction and stroke, the two leading causes of death worldwide. Rupture of plaque tissue is a mechanical event, where plaque stress or strain locally exceeds its strength. Biomechanical studies agree with histopathological findings that a large lipid pool and thin fibrous cap overlying the lipid pool increase the likelihood of rupture, by showing increased plaque stresses for these geometries. Another plaque morphological feature that is frequently encountered is calcification. However, its role in the vulnerability of plaques to rupture is not fully understood, and biomechanical modeling studies do not agree on the effect of calcifications on plaque stress. These studies used isotropic material properties for the anisotropic and collagen rich plaque tissue, and generally focused on the effect of calcification on lumen stress or cap stress. However, histopathological findings revealed tissue damage at the interface between calcification and surrounding tissue.

This study investigated stresses and strains at the interface between calcification and fibrous tissue, how these stresses and strains are influenced by local anisotropy of the fibrous tissue and how geometric features of the calcification are related to these metrics. A morphometric study was conducted first, to investigate and categorize different patterns of fiber alignment around the calcifications, and to measure the calcification geometric features including its location in the plaque, its shape and its size. Biomechanical models including the local anisotropic material properties were constructed next, based on the observations and measurements made in the morphometric analysis. Stress and strain metrics were investigated at the calcification boundary, and subsequently related to fiber patterns and calcification geometric features.

Hundred forty five calcifications were segmented and measured in the morphometric analysis, and surrounding fiber alignments were studied. The analysis revealed that four main fiber patterns in the fibrous tissue surrounding calcifications exist: the Attached pattern, Pushed Aside pattern, Encircling pattern and Random pattern. Collagen fibers are attached to the calcification in the Attached pattern, are pushed aside by the calcification in the second pattern, encircle the calcification in the third pattern, and show a disorganized alignment in the Random pattern. The Attached pattern was the most prevalent fiber pattern, and its corresponding calcifications had larger aspect ratios and were on average larger than the other three fiber patterns. Large peak stresses and strains at the calcification boundary were identified in the biomechanical models for the Attached pattern and Pushed Aside pattern, while these metrics showed generally lower peak values for the Encircling pattern and Random pattern. Peak values for all stress and strain metrics were attained at the tip of the calcifications. Multivariate analysis showed that stresses and strains are related to the calcification geometric features; calcification interface stress and strain increased if the calcification was closer to the lumen, had a larger length/width ratio and was larger in size.

Histopathological examination of plaques evidenced damage at the interface between calcification and fibrous tissue, potentially caused by an adverse mechanical state at this boundary. Most studies focused on stresses at the lumen or in the cap however, and this study for the first time specifically investigated stresses and strains at the calcification boundary while simultaneously introducing local fibrous tissue anisotropy in the computational models. Results show that peak stresses and strains can develop at this boundary, which will remain undiscovered if isotropic materials are used. This study was also the first to extensively analyze calcification geometric features and surrounding fiber alignment in relation to these interface stresses and strains. Peak values were found to be dependent on these features and fiber alignment patterns, indicating a relation between these characteristics and mechanical stability of the plaque. The findings of this study further increase the clinical relevance of finite element modeling in rupture risk prediction by showing previously undiscovered peak stress and strain values for interfaces and geometric configurations which already were deemed to be destabilizing in clinical and histopathological studies.

Contents

Nomenclature

Abbreviations

2D	Two dimensional
3D	Three dimensional
CCA	Common carotid artery
CT	Computed tomography
CVD	Cardiovascular disease
ECA	External carotid artery
FE	Finite element
HE	Hematoxylin & eosin
ICA	Internal carotid artery
LDL	Low-density lipoprotein
SMC	Smooth muscle cell

Geometric Parameters

A_{calc}	Calcification aspect ratio	[-]
D_{bif}	Longitudinal distance to bifurcation	[mm]
D_{fib}	Fiber affected distance	[mm]
D_{inner}	Inner radial distance	[mm]
D_{norm}	Normalized distance	[-]
D_{outer}	Outer radial distance	[mm]
L_{calc}	Calcification length	[mm]
L_{norm}	Normalized width multiplied with calcification aspect ratio	[mm]
L_{sp}	Length of the straight part of the plaque model / subregion	[mm]
Th_{cap}	Cap thickness	[mm]
W_{calc}	Calcification width	[mm]
W_{norm}	Normalized calcification width	[-]

Stress & Strain Metrics

$S_{MaxPrin}$	Maximum principal stress (deviatoric)	[Pa]
S_{11}	Stress along fibers (deviatoric)	[Pa]

S_{22}	Stress across fibers (deviatoric)	[Pa]
S_{12}	Shear stress	[Pa]
S_{Mises}	Von Mises stress	[Pa]
$E_{MaxPrin}$	Maximum principal strain	[-]
E_{11}	Strain along fibers	[-]
E_{22}	Strain across fibers	[-]
E_{22}	Shear strain	[-]

1 Introduction

Cardiovascular diseases (CVDs) are the leading causes of mortality, accounting for 31% of all deaths worldwide [1]. The vast majority of these deaths are due to ischemic heart disease and stroke, with a combined worth of over 15 million deaths annually. The total burden of these clinical events accumulate up to 18% of all healthy years of life lost in the world [2], proving that ischemic heart disease and stroke are also a source of severe disability. These adverse events are majorly triggered by rupture of atherosclerotic plaques and subsequent thrombus formation in the artery, occluding the vessel and causing myocardial infarction (heart attack) or stroke [3, 4].

1.1. Atherosclerosis

1.1.1. Healthy Artery Wall

Arteries are part of the circulatory system and carry oxygenated blood away from the heart to all cells and tissues in the body. The artery is made up of three distinct layers surrounding the blood containing cavity or lumen: the tunica adventitia, tunica media and tunica intima. The tunica adventitia is the outermost layer, composed of collagen fibers, and is responsible for the structural integrity of the vessel. The tunica media, a thick layer of circumferentially aligned smooth muscle cells (SMCs), is the middle layer and gives the artery its mechanical properties like burst pressure and compliance. The tunica intima is a thin sheet of endothelial cells lining the lumen, and is attached to an elastic membrane [5] (See Figure 1.1).

The carotid artery is one of the main vital arteries in the body, and supplies the brain and face with oxygenated blood. It starts as the common carotid artery (CCA), and splits up in the external carotid artery (ECA), supplying the face with oxygenated blood, and the internal carotid artery (ICA), supplying the brain (see Figure 1.2). Local hemodynamics makes branching and bifurcation points, and thus the junction between CCA, ICA and ECA, susceptible to atherosclerosis [8, 9].

1.1.2. Atherogenesis

Atherosclerosis is initiated by a local uptake of low-density lipoproteins (LDLs) in the vessel wall as a result of endothelial dysfunction, it is a chronic, systemic and progressive disease, and it can start as early as during childhood (first decade of life) [10]. The atherosclerotic part of the artery is called lesion, and atheroma or plaque in more advanced stages[11, 12]. It primarily affects the intima layer, but its degenerate effect is also observable in the media and adventitia layers of the vessel [13, 14]. Bad lifestyle habits such as smoking, lack of exercise, obesity and unhealthy diet are major risk factors for developing this disease, although genetics also play a role [15, 16]. The onset and progression of an atherosclerotic lesion is visualized in Figure 1.3, which will be used to illustrate the various stages of atherosclerosis described next.

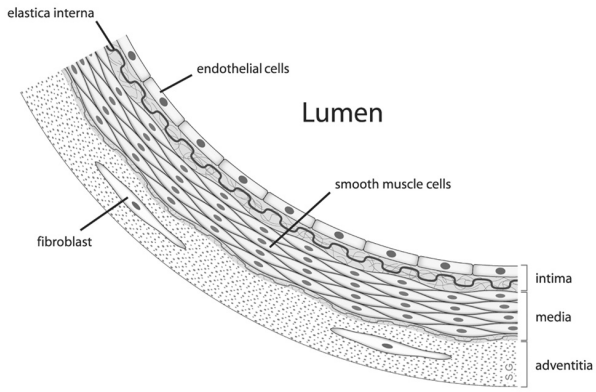

Figure 1.1: Idealized drawing of an artery wall cross-section with its three distinct layers: adventitia, media and intima. Figure adapted from [6]

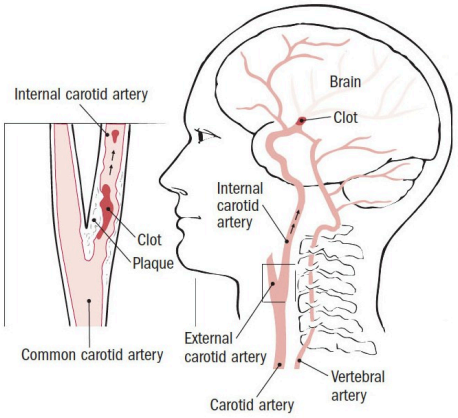

Figure 1.2: Schematic drawing of an atherosclerotic carotid artery with its branches; the internal carotid artery (ICA) and external carotid artery (ECA). Figure retrieved from [7]

Atherosclerosis is an inflammatory process, where the immune response of our body is activated to suppress the 'injury' to the vessel wall caused by the uptake of lipoproteins [17] (step 1 in Figure 1.3). Leukocytes are attracted to the site of injury (step 2 in Figure 1.3) as the LDLs in the vessel wall oxidize, where they then migrate into the vessel wall, proliferate and differentiate into macrophages to engulf the LDLs [18] (step 3 in Figure 1.3). Because of the overwhelming presence of these LDLs, the macrophages keep taking up the lipids until they end up as so-called foam cells, and become entrapped in the vessel wall (step 4 in Figure 1.3). Accumulation of these lipid-laden macrophages creates a fatty streak; the first visible sign of atherosclerosis [10].

Processes secondary to this lipid infiltration are the attraction and proliferation of smooth muscle cells in the intimal layer, which produce extracellular matrix, mostly collagen, as an attempt to encapsulate and thereby contain the disease [19] (step 5 in Figure 1.3). As the lesion progresses, the foam cells die and spill their lipid content, creating lipid pools in the process or necrotic cores if dead cell remnants are present [20, 21]. The thrombogenic content of lipid pools or necrotic cores are separated from the lumen by a layer of fibrous tissue, known as the fibrous cap. The ongoing and progressive nature of all these processes results in a thickening of the vessel wall. First this thickening is directed outwards to preserve the patency of the vessel, but later on this remodelling is not possible anymore, and the lesion encroaches on the lumen. This narrowing of the lumen is called stenosis [22, 23]. The lipid pools and parts of the fibrous tissue created by the smooth muscle cells can calcify in more progressed stages of atherosclerosis [24].

Rupture of the plaque can occur in advanced stages of atherosclerosis. Rupture of a plaque is a fissuring or failure of the plaque tissue, exposing its contents to the blood stream, and subsequently causing thrombus formation in the lumen (step 6 & step 7 in Figure 1.3). In the coronary arteries these flow obstructing thrombi cause ischemia in the heart muscle and subsequent myocardial infarction, and in the carotid arteries they cause ischemia in the brain and stroke (see Figure 1.2). Approximately three-quarters of deaths by myocardial infarction and stroke are the result of plaque rupture [25].

1.1.3. Plaque Calcification Development

Two distinct cellular mechanisms can be distinguished in calcification development in atherosclerotic plaques: a passive pathway, triggered by inflammation, and a subsequent active pathway, regulated by osteoblast-like and osteoclast-like cells, to subdue this inflammation [27]. The passive pathway is characterized by apoptotic cell bodies of macrophages and vascular SMCs and their matrix vesicles (small spherical bodies derived from the plasma membrane of the cells) in the inflammatory environment of the atherosclerotic lesion. These bodies and vesicles calcify, and agglomerate to become

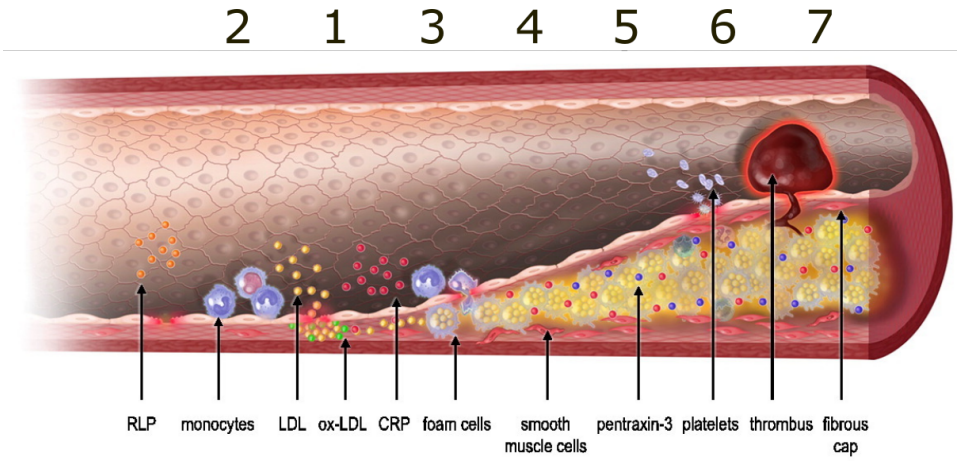

Figure 1.3: Progression of atherosclerosis in an artery. Figure adapted from [26].

small spherical calcifications in the µm range, known as microcalcifications (1–30 µm typically [28]). These microcalcifications, embedded between the collagen fibers of the plaque tissue and directed by the local orientation of the fibers in the plaque, can merge to become larger (macro) calcifications [28]. This process in turn stimulates the inflammatory response in which it originated, creating a positive feedback cycle [27].

As an adaptive healing response to stop the inflammation, surviving vascular SMCs might undergo osteogenic differentiation into osteoblast-like and osteoclast-like cells, resulting in the actively regulated mineralization of the plaque fibrous tissue akin to bone formation, with lamellar bone and bone marrow visible in developed structures [29, 30]. Large sheets of calcified plaque tissue in the millimeter range, to wall off the inflammation, are the result.

1.1.4. Treatment

Current treatment in carotid arteries is based on the degree of stenosis of the artery and the symptoms of the patient, with for example a 60% reduction in lumen area being the recommended threshold for intervention in asymptomatic patients [31]. Intervention can either be angioplasty with the placement of a stent to reopen the lumen, or an endarterectomy procedure [32]. Endarterectomy is the surgical procedure where the artery is cut open, and the plaque removed from within the artery to eliminate the possibility of events caused by these plaques.

However, only 1 out of 14 patients benefit from the surgery [33]. An important reason is that selection for this procedure is based on stenosis degree, and not rupture risk. The degree of stenosis is not a good predictor of plaque rupture; plaques can rupture at a significant lower level of stenosis than 60%, or plaques with a higher level of stenosis do not rupture at all [34]. Therefore, accurate markers for plaques at risk of fissuring are desirable.

1.2. Plaque Rupture Risk

Plaques that are susceptible to rupture, and develop intraluminal thrombi are called vulnerable plaques or high-risk plaques [35]. Rupture of a plaque is failure of the tissue, where structural stress in the plaque locally exceeds its strength and structural integrity is lost. Post-mortem studies on atherosclerotic arteries established some key identifiers of a vulnerable plaque: a large necrotic core or lipid pool, and a thin cap of fibrous tissue overlying this necrotic core or lipid pool are deemed to destabilize a plaque and predispose it to rupture [36, 37].

Rupture of these plaques is characterized by fissuring of the thin fibrous cap, exposing the lipid contents of the pool underneath to the blood stream. These findings are supported by biomechanical studies,

showing that stresses in the cap increase for decreasing values of cap thickness and increasing lipid pool size (e.g. see [38, 39]). However, not all plaque ruptures can be predicted using only these markers. Additional plaque markers are therefore needed to complete the definition of a vulnerable plaque. Calcification is another highly prevalent plaque constituent, and its role in plaque vulnerability received therefore considerable attention.

Imaging of coronary plaques using computed tomography (CT) revealed that the more calcified an atherosclerotic artery is, the higher the change of having an adverse event in the (near) future, and that having no calcification at all is a reliable indicator of a patient having a low risk of experiencing an event (e.g. see [40, 41]). High resolution intravascular imaging shows that the location of the calcifications is also important, with calcifications close to plaque rupture sites being more superficial (close to the lumen) than calcifications in intact plaques (e.g. see [42, 43]).

Stretching plaque tissue until the material fails shows that calcifications reduce the ultimate stress and stretch at which a plaque ruptures [44, 45], and that the plaque fissures at the interface between the calcification and the surrounding fibrous tissue [46–48]. Scanning electron microscopy images taken from these fissure sites shows that calcifications have different ways of interacting with the surrounding tissue, causing different fiber alignment patterns in the vicinity of the calcification (see Figure 1.4). This interface failure has also been observed *in-vivo*, after balloon angioplasty [49]. Analysis of carotid endarterectomy samples shows that these interface fissures also develop under physiological loading conditions [50], indicating that fibrous cap rupture is not the only failure mechanism; ruptures might also start or end at these interfaces. It is reasoned that the difference in stiffness between the calcification and the surrounding tissue causes mechanical instability of the plaque, and therefore an increased risk of rupture [42, 49].

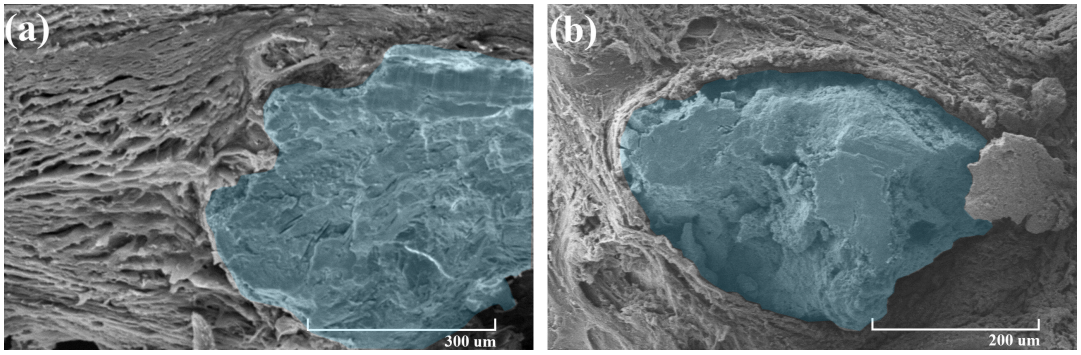

Figure 1.4: Scanning electron microscopy images taken from calcifications (highlighted in blue) in fibrous tissue, showing different fiber alignments. (a) Fibers of the tissue ending at the calcification boundary, (b) fibers of the tissue pushed to the side by the calcification. Figure adapted from Mulvihill *et al.* [47]

1.3. Plaque Biomechanics

As stated in the previous section, rupture of a plaque is a mechanical failure, and happens when structural stresses in the plaque exceed the the strength locally. Understanding what plaque features elevate these stresses is therefore of utmost importance in predicting plaque rupture. Structural stresses in plaques arise mainly from the blood flow, exerting shearing stresses at the vessel wall due to fluid friction, and stress normal to the vessel wall due to blood pressure. Due to the complexity of the plaque geometry, material behaviour and boundary conditions, it is not possible to calculate these stresses analytically, and numerical methods have to be employed. The finite element (FE) method is commonly used for this purpose, where biomechanical models are constructed of plaques, and structural stresses in the plaque tissue calculated [51].

1.3.1. Finite Element Modeling

In the finite element method, a continuum (here: the plaque geometry) is discretized in small elements (hence the name finite element method) to approximate solutions of equilibrium equations for each element separately. These equations are approximated iteratively in the solver of the software until convergence of the equilibrium is achieved. Plaque modeling started with the hallmark paper of Richardson, Davies and Born in 1989, showing that peak stresses in the plaque coincide with rupture sites [52]. Many modeling studies followed, showing that calculated plaque peak stresses correlate with clinical events [53, 54], and thus emphasizing the potential of biomechanical modeling in predicting which plaque features increase the risk of rupture.

The modeling process can be divided in three distinct phases: the preprocessing phase, the processing phase and the postprocessing phase. In the preprocessor phase the model is constructed and discretized in a mesh of small elements (see Figure 1.5a). Both simplified plaque geometries (e.g. see [55]) or realistic patient specific geometries (e.g. see [56]) are used in literature.

Constitutive equations relating stress to strain are needed to characterize the mechanical properties of different plaque materials. These relations range from the simple linear and isotropic Hooke's law for calcifications (e.g. see [55]), to complex strain energy density functions which describe hyperelastic fiber reinforced materials for vessel walls (e.g. see [57]). Blood pressure and boundary conditions (to fix the plaque in space for example) are applied to the model before it is sent to the solver of the software in the processing phase. Shearing forces due to fluid friction are typically a few orders of magnitude smaller than the normal stresses due to blood pressure, and are thus neglected in most studies (e.g. see [58]).

The equilibrium equations are solved in the processing phase, and in the postprocessor phase the calculated stresses are visualized. The calculated stress state at each point in the continuum cannot always be interpreted intuitively. Therefore, scalar representations of these stress states are used. Commonly used stress representations are Von Mises stress or maximum principal stress, but it is not fully clear which of the two is the best measure for plaque stress calculations [51]. The stress representation is plotted on the plaque geometry as a color map, showing intuitively the maximum values and gradients (see Figure 1.5b).

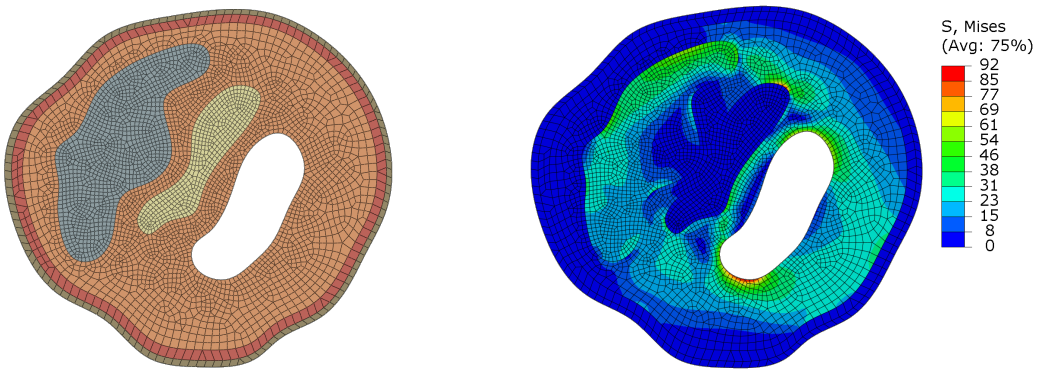

(a) (b)

Figure 1.5: 2D biomechanical model of a plaque cross-section. (a) Meshed model where gray is a large calcification, yellow is lipid pool, orange is fibrous tissue, and red and brown the media and adventitia respectively. (b) Stress contour plot of the same model, showing the Von Mises stress in kPa.

1.3.2. Plaque Calcification Modeling

Imaging studies and mechanical stretching studies indicate that calcifications alter the stress state in plaques in an unfavourable manner (see previous section), however, results from biomechanical studies show controversial results for certain calcification features like its presence or amount, and the

question how calcifications are mechanically related to vulnerability remains unanswered. Both micro and macro calcifications have been investigated in the biomechanical field.

Multiple studies found macro calcifications to be stress reducing; changing lipid pools into calcifications in FE models of plaques lowered stresses (Kiousis *et al.* [57]), and replacing the calcifications with fibrous tissue increased the stresses a little (Huang *et al.* [58]). The latter study also found that the larger the amount of calcification, the lower the stresses are. Placing a large calcification in the fibrous cap (Imoto *et al.* [59]), or next to the cap (Vengrenyuk *et al.* [60]) was found to lower the stress in the cap.

However, multiple other studies found a stress elevating effect of macro calcifications: Li *et al.* [61] found that calcifications in the cap *do* increase the cap stress. Another study found that plaques that caused adverse events had larger amounts of calcification, which were closer to the lumen than plaques that did not cause events (Brown *et al*. [54]). Teng *et al.* [53] also found that plaque stresses increased for increasing amount and individual size of calcifications, although this effect did plateau after a certain amount and size.

Most studies report the overall peak stress in a plaque, while one study specifically investigated the stress at the interface between calcification and fibrous tissue, a location of stiffness mismatch (Buffinton and Ebenstein [55]). It was found that this interface stress increases for increasing calcification size, calcification ellipticity (length divided by width) and decreasing distance from the lumen.

A series of studies aimed at micro calcifications revealed that these small inclusions in a fibrous cap are a cause of stress concentration (e.g. see Vengrenyuk *et al.* [60]). This stress concentration became even larger for microcalcifications with an elliptical shape, or if the distance between two micro calcifications decreased (e.g. see [62]. The assumed failure mode for these small inclusions is initial debonding at the surface of the calcifications, and a subsequent cavitation-like expansion of the created void [63].

1.4. Thesis Motivation & Outline

1.4.1. Motivation

Imaging studies and mechanical studies (stretching the plaque tissue until failure) show the importance of calcifications in relation with plaque rupture risk, but the biomechanical modeling field is undecided on the exact mechanisms or nature of this relation. Controversial results are found for macro calcifications mostly, showing no clear relation between stress and the rigid inclusions. Biomechanical models are simplified representations of reality, and choices made in simplifying this ground truth will inherently affect the accuracy of study outcomes. The more sophisticated these models are constructed, the closer they represent reality and the more accurate the outcomes will be.

One important requisite for these models to be accurate is a correct representation of the materials present in plaques. Most biomechanical modeling studies involving plaque calcifications used isotropic material models for the highly anisotropic fibrous tissue (e.g. see [53, 54, 58, 61, 64, 65]), while others used an orthotropic material model where different stiffnesses in radial and circumferential direction of plaque cross-sections is used (e.g. see [55, 59, 60, 66]).

However, from mechanical testing studies it is known that calcifications influence local anisotropy by interacting with the fibrous tissue, thereby creating different patterns of the collagen fibers in their vicinity (see Figure 3.2) [47]. The stiffness mismatch between the calcification and soft surrounding tissue is therefore complicated; the mismatch depends on the local orientation of the fibers with respect to the calcification.

Local stress and strain concentrations between the two plaque materials could lead to failure of the tissue, and subsequently fissuring of the plaque [50]. Knowing how local fiber alignment around the calcifications influence these peak stresses and strains at the calcification - fibrous tissue interface is

therefore important, and the absence of these representative local alignments in the current models therefore negatively impact the accuracy of study outcomes.

1.4.2. Objective & Outline

The objective of this thesis is to update biomechanical modeling of calcified carotid plaques by introducing fibrous tissue anisotropy, especially its local behaviour around calcifications, and to investigate how this sophisticated material behaviour in biomechanical models influence stress and strain calculations at the interface between calcifications and fibrous tissue. Subsequently, the influence of geometric features of calcifications on these stresses and strains will be investigated. The overarching goal is to make calcification modeling more accurate, and to take a first step in finding an answer to the question why biomechanical studies on calcification and plaque vulnerability show contradictory results. The research question is twofold, and can be stated as follows:

(i) How does local anisotropy of the fibrous tissue surrounding calcifications influence stresses and strains at the interface of these two plaque materials?

(ii) How are these interface stresses and strains influenced by the calcification geometric features?

The first part of this project is dedicated to the analysis of endarterectomy samples of human carotid plaques, to assess what patterns of fiber alignment around calcifications are present, where in the plaque they are found, and what the geometric features of the corresponding calcifications are. The outcome of this part of the study is the input for the actual modeling of the plaques. In Chapter 2 the methodology of analysis is explained, and in Chapter 3 the results of the morphometric analysis are presented.

The second part is on the modeling of the carotid plaques with realistic fiber alignment patterns around the calcifications. The geometry of the plaque is an idealized cross-section of a human carotid plaque, and in this idealized geometry the calcification with the local anisotropy is modeled. The parameters obtained in the first part of the project serve as input for these models, making this a parametric study where observed fiber alignment patterns, calcification locations, sizes and shapes are varied along parameter ranges found in the first part. In Chapter 4 the modeling methodology is presented, followed by the results and its interpretation in Chapter 5. Chapter 6 provides a general discussion, and concluding remarks are made in Chapter 7.

2

Plaque Analysis Methods

The first part of this study is a morphometric analysis of calcifications and the local fiber alignment of the surrounding fibrous tissue in human carotid plaques. Calcifications were segmented on histology images of carotid plaque endarterectomy samples, tissue fiber alignments were studied and dimensions and distances were quantified. A dataset of histology images was readily available for this purpose. The comprehensive dataset obtained in this part not only serves as input for the second part of this study (the modeling part), but is a study on its own, providing valuable information on calcifications and fibrous tissue structures in plaques.

2.1. Characteristics of the Available Database

2.1.1. Endarterectomy Samples

A database of histology images of human carotid endarterectomy samples (n = 37) was available for analysis. An endarterectomy is a surgical procedure to treat the carotid artery disease; the carotid artery is cut open, and plaque tissue removed from within the artery. Each of these endarterectomy samples was from a unique patient, from either the right or left carotid artery (see Figure 2.1 for a carotid endarterectomy sample).

The samples were cut in sections of 1 mm thickness in longitudinal direction of the artery, and from each section cross-sectional slices of 5 µm thickness were cut for different staining techniques, to highlight different tissues or structures. The samples were decalcified beforehand to make the cutting process possible (cutting trough this bone-like material will otherwise severely damage the samples and render them unusable for further analysis).

2.1.2. Histology Images

For each endarterectomy sample a hematoxylin & eosin (HE) staining was available of each 1 mm section (see Figure 2.2 for an HE stained cross-section). As previously mentioned, samples were decalcified, but sites of calcification were still visible on the HE stained slices because of calcification remnants. HE is a staining in histopathology that colors the collagen in the intima tissue (the fibrous tissue) pale pink and gives the calcification remnants a purplish hue. The collagen fibers and their orientations are visible as slender beams or wires running through the tissue. High aspect ratio gaps that are present in the fibrous tissue also indicate the fiber orientation; as the long side of these gaps are always parallel to the fiber direction (see Figure 2.2, lower left corner).

The stained slices were imaged with virtual microscopy, a technique where the images obtained with the microscope are digitized and send to a PC. The images were exported as high resolution (110000 $\times$ 47000 pixels typically) virtual slices in the Hamamatsu file format (VMS, VMU or NDPI). Computed

tomography (CT) scans were also available for a subset of these endarterectomy samples. Calcifications are easily discernible on CT images as bright white spots on the dark grey surrounding tissue (see lower right inset in Figure 2.2).

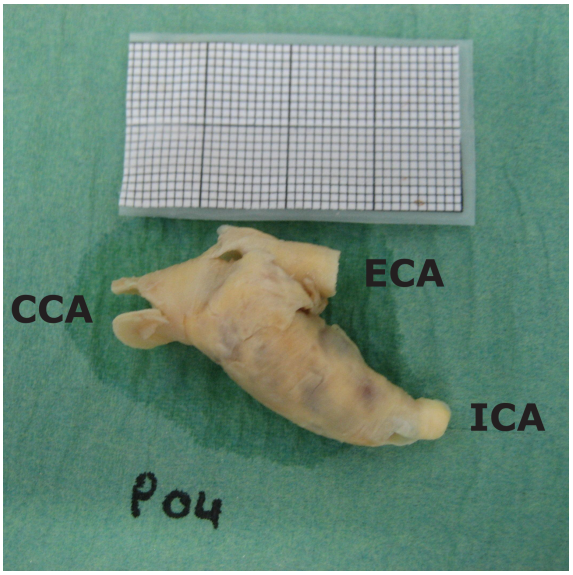

Figure 2.1: A carotid endarterectomy sample before slicing. The common carotid artery (CCA), internal carotid artery (ICA), and external carotid artery (ECA) are labeled in the image. The little squares on the scale are millimeters.

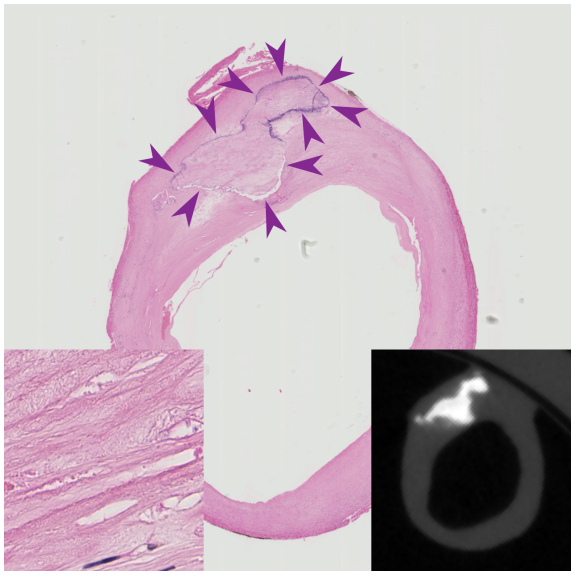

Figure 2.2: HE stained cross-section of a carotid plaque. Large calcification indicated with purple arrowheads. Lower left corner: high-power view of fibrous tissue, showing the fibers as slender beams and high aspect ratio gaps (white spaces) between the fibers. Lower right corner: CT image of same cross-section, white is calcification.

2.2. Histology Image Analysis

2.2.1. Initial Search & Selection

The HE stained slices (total amount of 685) from the above mentioned dataset were used for the analysis of the calcifications and the local fibrous tissue alignment in the plaques. An initial analysis of the slices was performed to obtain an overview of the different local fiber alignments around calcifications that are present, and to select eligible endarterectomy samples based on their quality. Location of the calcification in the artery was determined in the final analysis, it was therefore necessary to be able to discern different segments of the artery from each other (by locating the bifurcation point between CCA, ICA and ECA). Only samples for which this was possible, and thus not too damaged, were included in the study (n = 19). The cross-sections of these eligible endarterectomy samples were then systematically searched for intact calcification sites and local fibrous tissue alignments. the CT images that were available for a subset of endarterectomy samples were used to aid in the segmentation of calcifications.

2.2.2. Systematic Search

From the remaining 19 endarterectomy samples the HE stained cross-sections (n = 380) were systematically searched for calcifications, but first, the bifurcation point of the sample was established. The bifurcation point is defined as the apex or flow divider of the ICA and the ECA, visible as a thin wall dividing the lumens of the ICA and ECA on the histology cross-sections, and is used as starting point of the analysis (see Figure 2.3).

Histology at every 1 mm was available, however, every 3rd cross-section was selected for the analysis and this selection was considered to provide a good representation of plaque calcification. Starting from

the bifurcation point, steps of 3 mm were made throughout the plaque until the end of the plaque was reached, and analysis performed at each of these steps (see Figure 2.3, large arrow). The ECA typically contained little plaque material, or the plaque material was too damaged for histology processing, and the analysis was therefore limited to the CCA and ICA.

If analysis was not possible at a 3 mm step (damage of the tissue, no calcification present), a 1 mm step upwards (downstream) or downwards (upstream) would be made in the plaque, and corresponding cross-sections checked for calcifications and local fiber alignments (see Figure 2.3, small arrows). If an endarterectomy sample theoretically did not contain any measurable calcification with local fiber alignment, every 1 mm section would be examined in the end, and there was no chance of overlooking any calcification this way. A minimal distance of 2 mm was kept between analyzed cross-sections, as it was found in the initial analysis that large calcifications could occupy two successive slices that are 1 mm apart, and would otherwise be measured twice. The two small red arrows in Figure 2.3 show such a conflict.

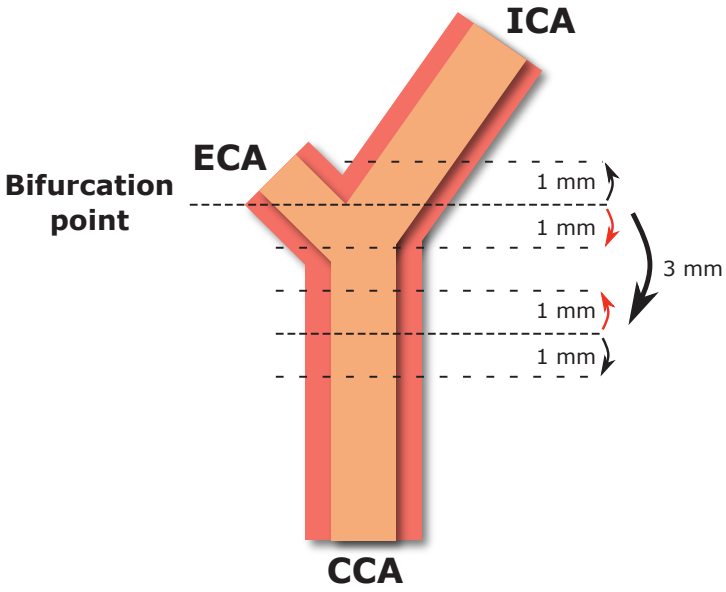

Figure 2.3: Sampling of the carotid plaque endarterectomies. Conflict of two successive slices indicated by the red arrows.

2.2.3. Observations, Measurements & Calculations

Observations and measurements were performed on the high resolution virtual slices created by the virtual microscope. The corresponding image files were accessed with NDP view 2 (Hamamatsu Photonics KK, Hamamatsu, Japan) and the build-in measurement tool was used for the actual measurements. First, the local fiber alignment around the calcification was analyzed and categorized in distinct patterns, and then measurements on calcification size, shape and location performed. Observation and classification of the fiber patterns of the calcifications was done by visually analyzing the structure, and the parameters relating to the geometric features of the corresponding calcification were quantified (see Figure 2.4). Some calcification geometric features were calculated from measured parameters. The observation, measurements and calculations are listed below:

1. Fiber pattern around the calcification, optionally its size: D_{fib}
2. Longitudinal location of the calcification, measured from the bifurcation point: D_{bif}
3. Cross-sectional location of the calcification: D_{norm}
   (a) Radial distance from lumen to center of calcification: D_{inner}
   (b) Radial distance from center of calcification to outer edge of plaque: D_{outer}

4. Shape of the calcification: A_{calc}
   (a) Length of the calcification: L_{calc}
   (b) Width of the calcification: W_{calc}
5. Size of the calcification: W_{norm}
6. Cap thickness: Th_{cap}

Classification of the fiber pattern and the parameters related to the calcification geometric features (list items 2–6) were regarded as essential for this study, and if one of them was rendered immeasurable due to damage of the histology slice, the calcification - fiber pattern combination was excluded from analysis. If this resulted in less than three eligible cross-sections per endarterectomy sample, the sample was excluded from analysis, as a minimum of three cross-section per sample was used as a inclusion criterion to assure that each sample delivered a significant contribution. Three endarterectomy samples were excluded because of this criterion, lowering the amount of included samples in this study to 16.

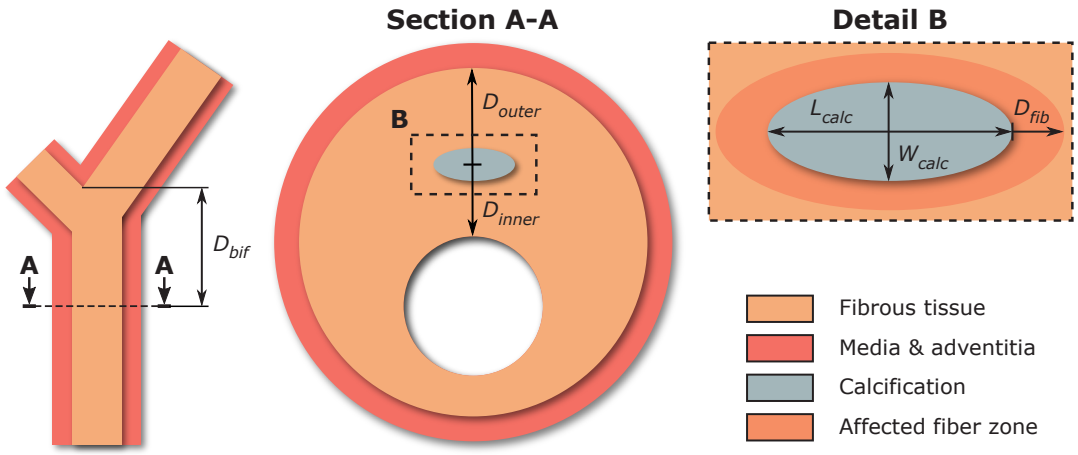

Figure 2.4: Measurements performed on the plaque cross-sections.

1. Fiber pattern

Distinct fiber patterns were obtained in the initial search of the histology images, and in the subsequent systematic search each segmented calcification was categorized accordingly. The main orientation of the fibrous tissue in the plaque was locally disrupted by the calcification. However, it was hard to determine at what point the main orientation transitions into this local orientation (D_{fib} in Figure 2.4), and this distance might not be the same in each direction. This distance was therefore regarded as an optional measurement, and calcifications were not excluded from the analysis if D_{fib} was not measurable.

2. Longitudinal location of the calcification

Longitudinal distance D_{bif} was measured to indicate where in the artery the calcification and its fiber pattern was found. Plaque initiation and progression is influenced by local blood flow patterns, and analysis of carotid plaques is therefore divided in literature in three different regions to reflect this location dependent behaviour. These regions are the bifurcation region, the CCA and the ICA (see Figure 2.5). The bifurcation region is defined as the region between the bifurcation point and 10 mm down in the CCA, in this region the plaque initiation and progression is influenced by turbulent blood flow, and differs from plaque formation in the CCA and ICA [67]. The CCA in turn shows little plaque development. D_{bif} was positive for calcifications in the ICA, and negative otherwise.

3. Cross-sectional location of the calcification

Location of the calcification in the plaque cross-section was determined by the radial distances D_{inner} & D_{outer}, both measured from the calcification center. These parameters on their own did not account for local plaque size however, and a normalized distance, with respect to the thickness of the plaque at the location of the calcification, was calculated from these two parameters. This normalized distance ranged from 0 at the lumen to 1 at the outer edge of the cross-section, and was calculated as follows:

$$D_{norm} = \frac{D_{inner}}{D_{inner} + D_{outer}}. \tag{2.1}$$

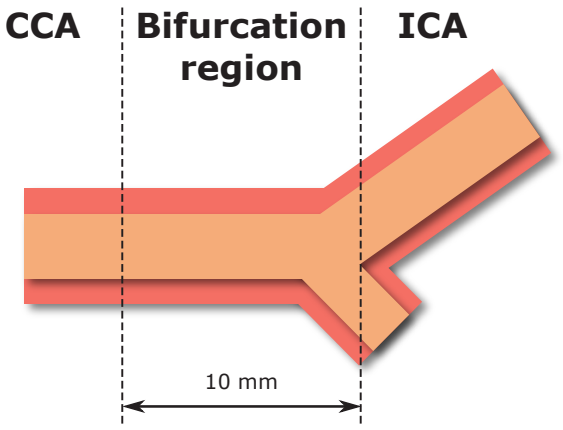

Figure 2.5: Distinct regions in the carotid plaque, used to reflect differences in plaque initiation and progression.

4. Shape of the calcification

A generalized elliptic shape was assumed for all calcifications, defined by their length L_{calc} (dimension in circumferential direction), and width W_{calc} (dimension in radial direction). From these dimensions the aspect ratios of the calcifications could be calculated:

$$A_{calc} = \frac{L_{calc}}{W_{calc}}. \tag{2.2}$$

If $A_{calc} = 1$ the calcification was a circle, if $A_{calc} > 1$ the calcification was an ellipse with its major axis aligned in circumferential direction, and if $A_{calc} < 1$ the calcification had its major axis aligned in radial direction of the plaque.

5. Size of the calcification

Not only the size of the calcification varied, but also the size of the plaque. To determine a calcification size with respect to the plaque itself at the location where the calcification was segmented, a normalized size could be calculated:

$$W_{norm} = \frac{W_{calc}}{D_{inner} + D_{outer}} \tag{2.3}$$

where W_{norm} is a normalized width. Together with the normalized width, a calcification size can be related to the size of the plaque at its respective location. A W_{norm} of 1 meant that the calcification occupied the plaque from the lumen up to the medial layer.

6. Cap thickness

In literature, an important marker for plaque vulnerability is cap thickness (see Section 'Vulnerable Plaque' in the introduction). Typically, this term is used for fibrous tissue overlying a lipid core, but is also used in calcification studies (e.g. see [55, 68]). This cap thickness could be calculated by taking half the width of the calcification from the inner radial distance:

$$Th_{cap} = D_{inner} - \frac{1}{2}W_{calc}. \tag{2.4}$$

2.3. Data Analysis

The measurements and calculations of the parameters were stored in a Microsoft Excel spreadsheet, and further analysis of the obtained data was performed in MATLAB (version 2017a), using the statistics toolbox. Measured and calculated parameter ranges were visualized in box plots (Q1, median & Q3) with whisker lengths of 1.5 $\times$ interquartile range (Q3 - Q1). Distinction in parameter range was made between fiber pattern categories. Significance of difference in parameters between fiber pattern categories was tested using the non-parametric Kruskal-Wallis *H* test. The null hypothesis was that samples from different fiber pattern categories were the same.

The measured parameters in Section 2.2.3 might be related to each other, and correlation between these parameters was tested with the Spearman's rank correlation test (r_s), a robust non-parametric correlation test which accounts for possible outliers in measurement data. The correlation coefficient r_s can take values between -1 and +1. A value of +1 indicates a perfect positive correlation between two parameters, -1 a perfect negative correlation, and 0 means no correlation between the parameters. The null hypothesis for this test was that there is no correlation.

3

Morphometric Analysis Results

The collagen fibers of the fibrous intima tissue are predominantly aligned in circumferential direction of the plaque, as an adaptation to the circumferential stretch and stress in the vessel wall due to blood pressure [69, 70]. This global orientation is locally disrupted by its interaction with calcifications in the tissue. How these interactions affect fiber alignment, how alignment patterns are distributed in the plaque, and what the corresponding locations, dimensions and shapes of the calcifications are, is presented next.

3.1. Fiber Alignment Characteristics

Four main local fiber alignment patterns were found during the initial analysis of the carotid endarterectomy samples (see Figure 3.1a-3.1d). The four fiber patterns are distinguishable from each other based on how the collagen fibers of the fibrous tissue are oriented locally in the vicinity of the calcifications:

1) In the first fiber pattern the fibrous tissue shows no local disruption caused by the calcification: the collagen fibers run straight into the calcification at its circumferential sides, and run alongside the calcification at its radial sides (see Figure 3.1a). Fiber structure is also visible inside the calcification, indicating that the fibrous tissue itself may be calcified in this specific fiber pattern. This explains why it seems that the fibers end up at the calcification boundary: the fibers do not actually end here, but go on as calcified fibers. This fiber pattern will be named the Attached pattern. 2) The second fiber pattern commonly encountered is where the calcification is embedded between the collagen fibers: the fibers are pushed aside by the calcification in radial direction. No fibers are attached to the calcification in this pattern, the slender beams have to get round the inclusion (see Figure 3.1b). In the remainder of the this report this fiber pattern will be named the Pushed Aside pattern. 3) Collagen fibers in the fibrous tissue encapsulate the calcification in the third detected fiber pattern: a band of fibers encircling the calcification is visible for this pattern (see Figure 3.1c), which will be named the Encircling pattern from now on. 4) No distinct fiber orientation is observable for the fourth and last main fiber pattern. The fibrous tissue is disorganized, showing a random orientation of its collagen fibers (see Figure 3.1d). This pattern will be named Random pattern.

Combinations of these four fiber patterns were also found; for example fibrous tissue encircling one half of the calcification, while at the other half the fibrous tissue is attached to the calcification (see Figure 3.1e) or fibers pushed aside at one half while the fibers are attached to the calcification at the other half (see Figure 3.1f).

3.2. Fiber Patterns

Sixteen carotid endarterectomy samples were analyzed in total, with a combined amount of 65 cross-sections (on average four per endarterectomy sample), resulting in 171 unique calcifications and their

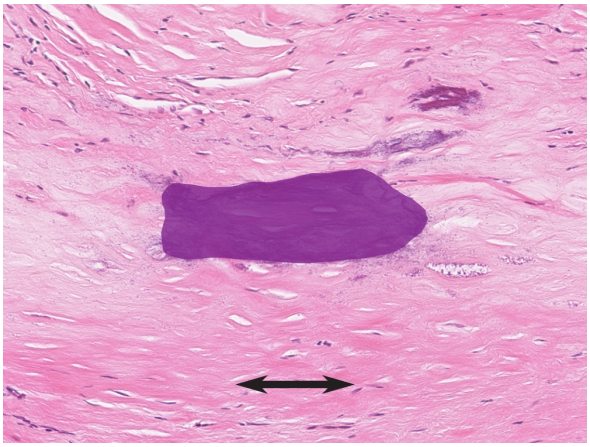

(a) Attached

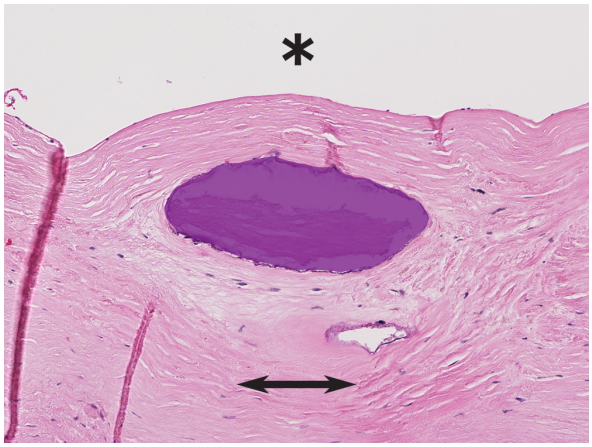

(b) Pushed Aside

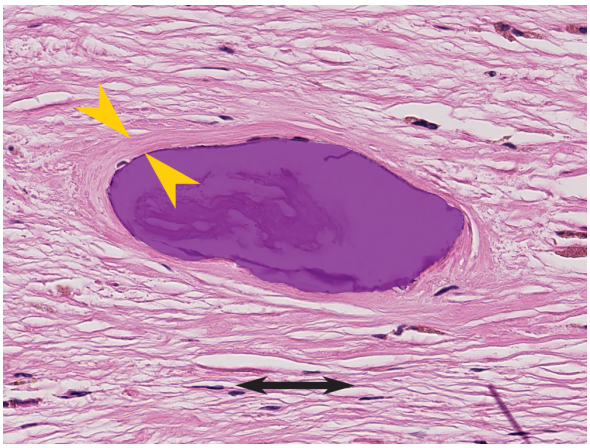

(c) Encircling

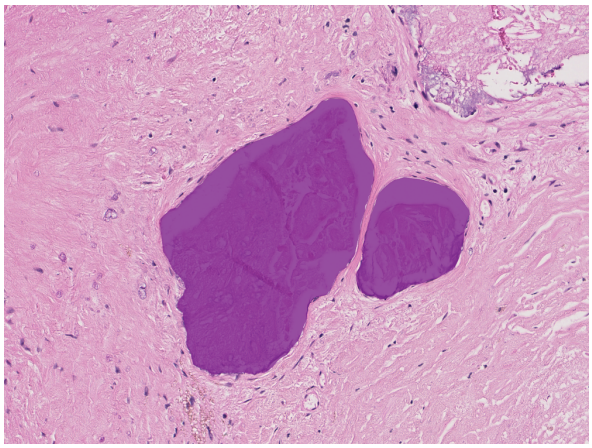

(d) Random

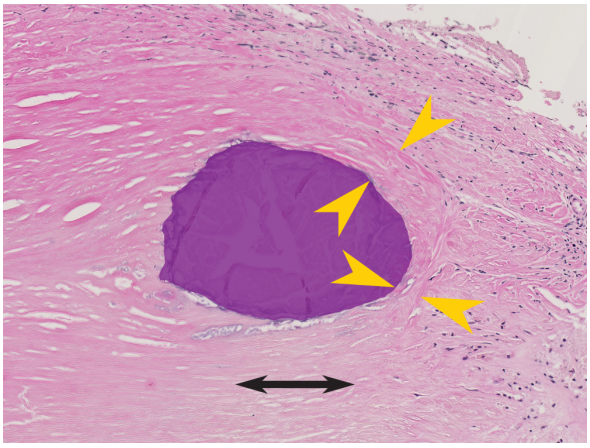

(e) Attached & Encircling

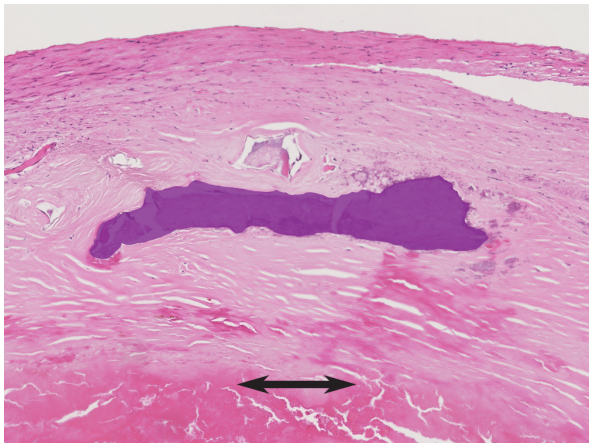

(f) Attached & Pushed Aside

Figure 3.1: Four main fibrous tissue patterns found in carotid plaques, and two examples of combinations of these fiber patterns, calcifications are highlighted in purple. Circumferential direction (and thus main fiber direction) indicated by double-headed arrow. (a) Fibrous tissue attached to calcification, (b) fibrous tissue pushed aside by calcification (asterisk is lumen), (c) fibrous tissue encircling the calcification (encircling fibers indicated by yellow arrowheads), (d) random orientation of the fibrous tissue surrounding the calcification, (e) combination of two fiber patterns: fibers attached to the calcification at the left side, fibers encircling at the right side (yellow arrowheads), and (f) a combination of fibers pushed aside by the calcification (left side) and fibers attached to the calcification (right side).

fiber patterns segmented, categorized and measured (on average two and a half per cross-section).

Distribution of the fiber patterns is visualized in the pie chart in Figure 3.2. The Attached fiber pattern (Figure 3.1a) is most prevalent, accounting for 38% (64 unique cases) of all fiber patterns. Second most prevalent is the Encircling pattern (Figure 3.1c), found in 23% (40 unique calcifications) of the cases. Third and fourth are the Pushed Aside (Figure 3.1b) and Random (Figure 3.1d) patterns, making up for 15% (25 cases) and 9% (16 cases) of all calcifications and their fiber patterns, respectively. Combinations of these four main fiber patterns constitutes 15% of all cases; the most prevalent combination, fibers attached to one side of the calcification combined with fibers pushed aside at the other side, accounting for 5% of all cases.

No calcifications and their fiber patterns were segmented in the CCA below the bifurcation region, with the most proximal calcification found at a distance of 6 millimeter from the bifurcation point. The most distal calcifications in the ICA were found at a distance of 18 mm from the bifurcation point. 70 Calcifications and their patterns were segmented in the bifurcation region, and 101 in the ICA. Distribution of the fiber patterns differs between the bifurcation region and the ICA: almost no Random pattern was found in the bifurcation region (1%), while it accounts for 15% of all cases in the ICA. The Attached and the Pushed Aside fiber patterns show little difference in distribution between the bifurcation and ICA, but the Encircling pattern is more prevalent in the bifurcation (29%) than in the ICA (20%), see bar graph in Figure 3.2.

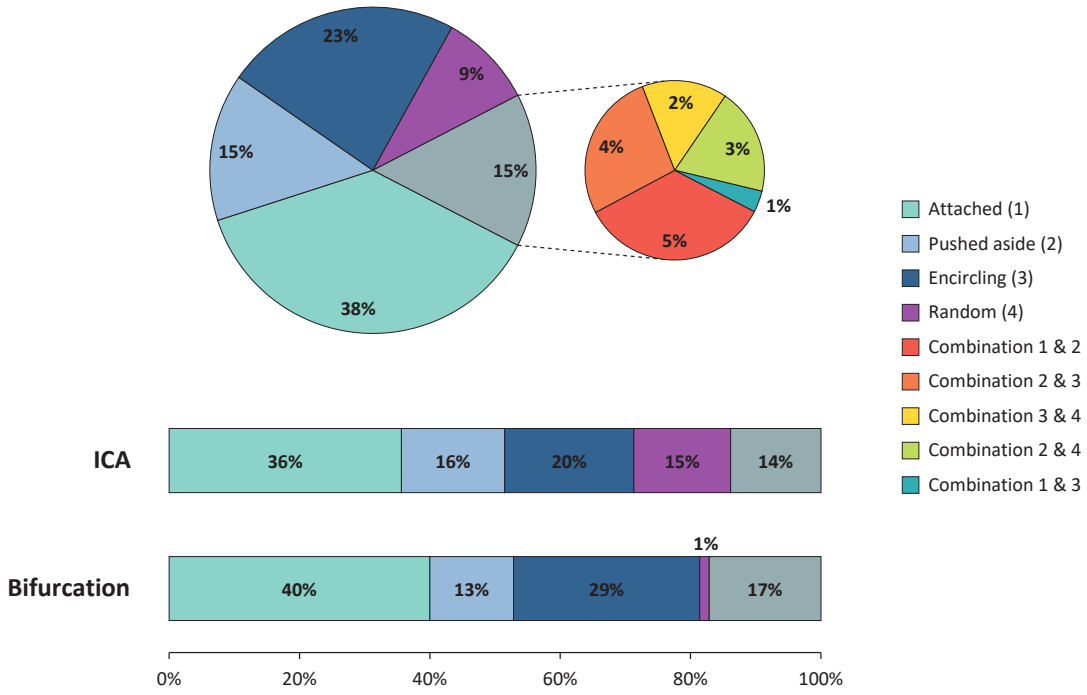

Figure 3.2: Distribution of the different types of fiber patterns and their combinations in the artery, pie chart: for the whole plaque, and bar graphs: divided per location in the artery.

3.3. Calcification Geometric Measurements

The measured and calculated parameters, as introduced in the previous chapter, will be discussed next. Results are non-normally distributed, as it can be seen from the skewedness of the boxplots presented next: uneven distances between quartiles 1 & 2 and the median, and uneven whisker lengths. The Kruskall-Wallis H test is thus appropriate here, as it does not assume normality of the measured data. Significant differences in measurement data between the different fiber patterns ($P < 0.05$) are indicated

with asterisks in the plots. Outliers (data points outside the 1.5 × interquartile range) are indicated with plus signs.

3.3.1. Longitudinal Location

A distinction in location of the different fiber patterns in the artery is already made in the bar graph in Figure 3.2, showing that the fiber pattern distribution may differ throughout the length of the plaque, especially for the Random pattern. Plotting the axial distance (D_{bif}) per fiber pattern emphasizes this difference: the Random pattern is grouped significantly higher in the artery (all data points, except for one, are in the ICA) than the other three fiber patterns (see Figure 3.3). No other significant differences are found between the four fiber patterns.

The boxplots also emphasizes that most of the calcifications and their fiber patterns are found in the ICA (101 vs 70 in the bifurcation region): the boxes are skewed towards the ICA (Median [Q1–Q3] value for all calcifications combined: 3 [-2–8]). The Encircling pattern has the most even distribution of data points in the bifurcation region and ICA; its median is the closest to the bifurcation point. This explains why it is relatively more prevalent in the bifurcation region than in the ICA (29% vs 20%): the other fiber patterns have a higher preference for the ICA.

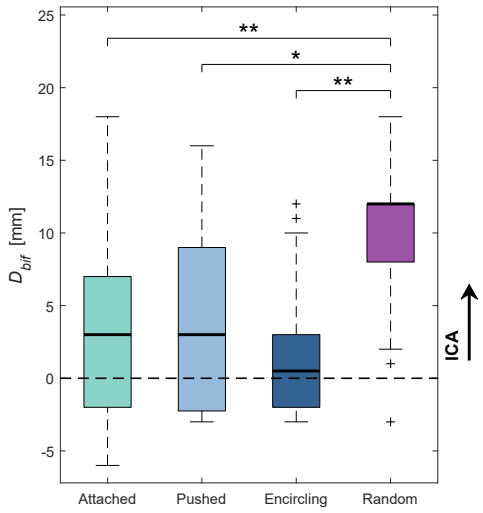

Figure 3.3: Axial distribution of the four main fiber patterns, measured from the bifurcation point. Dashed line indicates the bifurcation point. * Signifies $P < 0.05$, and ** signifies $P < 0.005$.

3.3.2. Cross-sectional Location

The location of the calcification in the cross-section of the plaque is defined by two parameters: D_{inner} & D_{outer}. D_{inner} is the distance from the lumen to the center of the calcification, and D_{outer} is the distance from the center of the calcification to the outer edge of the plaque. Distances for both D_{inner} and D_{outer} show large ranges, spanning millimeters, for each fiber pattern (see Figure 3.4a & 3.4b). Especially the Attached pattern shows large variability for both parameters, ranging to over 6 mm for D_{outer}, indicating that this fiber pattern can be found in large (width) plaques (see Figure 3.4b). The absolute distance to the lumen of this pattern is significantly smaller than that of the Encircling and Random patterns (see Figure 3.4a). The Random pattern is grouped closer to the outer edge of the plaque than the other fiber patterns, as can be seen in Figure 3.4b; the data points of this pattern are significantly lower (and thus closer to the outer edge) than the other fiber patterns.

As already noted, plaques have different sizes, with the Attached pattern being present in the larger plaques for example. The two parameters D_{inner} & D_{outer} do not account for this variability, and a

better way to display at what distance from the lumen the calcification - fiber pattern combinations are to be found is therefore needed. One way to do this is to normalize this distance, ranging from 0 at the lumen side to 1 at the outer wall (see Chapter 2 for the definition). Results of this normalization (D_{norm}) are plotted in Figure 3.4c. From these boxplots it can be appreciated that the Pushed Aside, Encircling & Random pattern distributions are skewed towards the outer edge of the plaque, with their medians above the equidistant line at D_{norm} = 0.5 (dashed line in the figure). The Random pattern is significantly closer to the outer edge of the plaque than the other three fiber patterns, and the Attached pattern is almost evenly distributed between the lumen and the outer edge. The median [Q1–Q3] value for D_{norm} for all calcifications combined is 0.65 [0.37–0.82].

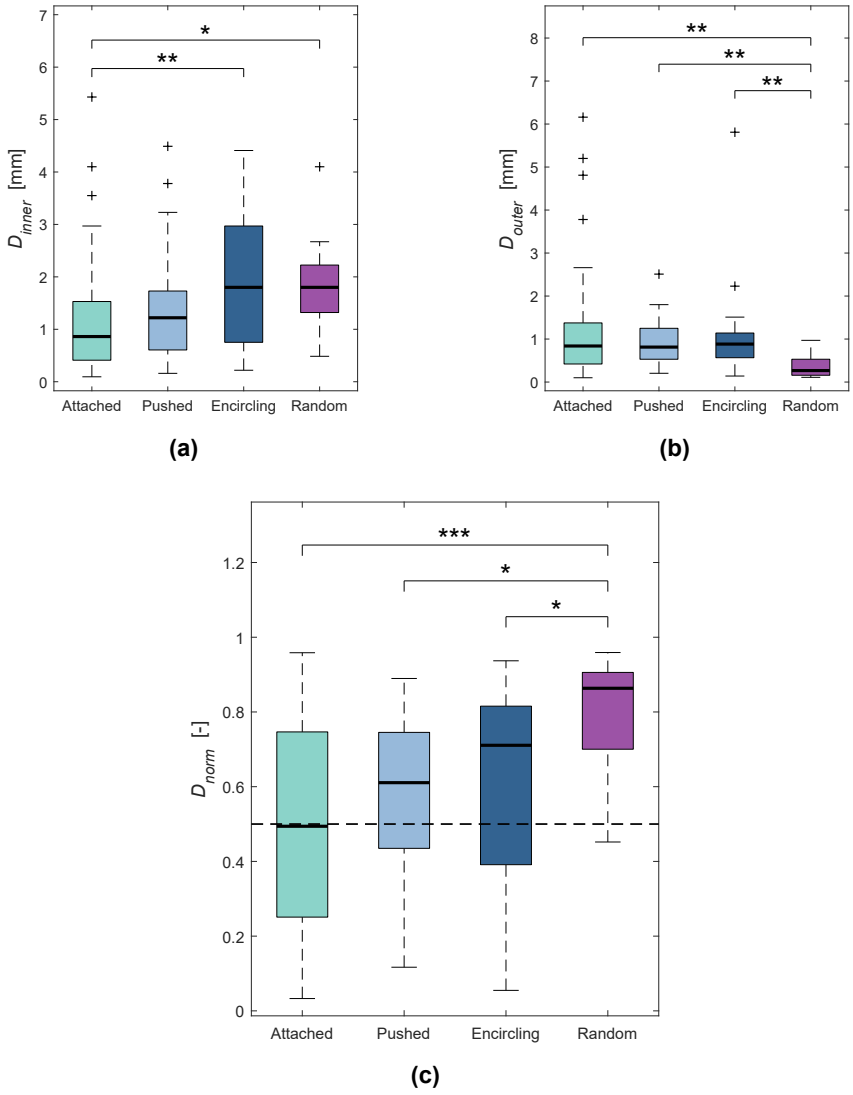

Figure 3.4: Inner, outer and normalized distance of the calcification in the plaque cross-section. (a) Absolute distance from the lumen to the center of the calcification, (b) absolute distance from center of the calcification to the outer edge of the plaque, and (c) the normalized distance in the plaque. Dashed line in (c) is equidistant between the lumen and the outer edge of the plaque. * Signifies P < 0.05, ** signifies P < 0.005 and *** signifies P < 0.0005.

3.3.3. Shape and Size of the Calcification

A generalized shape is assumed for the calcifications; an ellipse, defined by its length (L_{calc}) and width (W_{calc}). The length of the calcification is measured in circumferential direction of the plaque, and the

width in radial direction. Aspect ratio (A_{calc}) is length divided by width, meaning that calcifications with an aspect ratio of larger than one have their major axis aligned with the lumen and calcifications with an aspect ratio smaller than one have their major axis aligned in radial direction. Results for length measurements are plotted in Figure 3.5a, results for width in Figure 3.5b, and the corresponding aspect ratios are plotted in Figure 3.5c with a dashed line indicating an aspect ratio of one. The largest variation was found for the Attached pattern, for all three parameters. Length of calcifications with this fiber pattern can be up to 3.5 mm and width can reach 3 mm, while other calcifications do not reach 2 mm for length and 1.5 mm for width (see Figure 3.5a & 3.5b). The aspect ratio of calcifications with the Attached pattern can reach values up to 18.3, while other calcifications do not surpass aspect ratios of 4.1. By far most of the calcifications have their major axis aligned with the lumen (parts of the box plots above the dashed line in Figure 3.5c), but for all four fiber patterns it is also possible to have calcifications with their major axis aligned in radial direction (see parts of the box plots below the dashed line in Figure 3.5c). The median [Q1:Q3] value for the aspect ratio for all calcifications is 1.97 [1.23–3.02], emphasizing the fact that most calcifications have their major axis aligned with the lumen of the plaque.

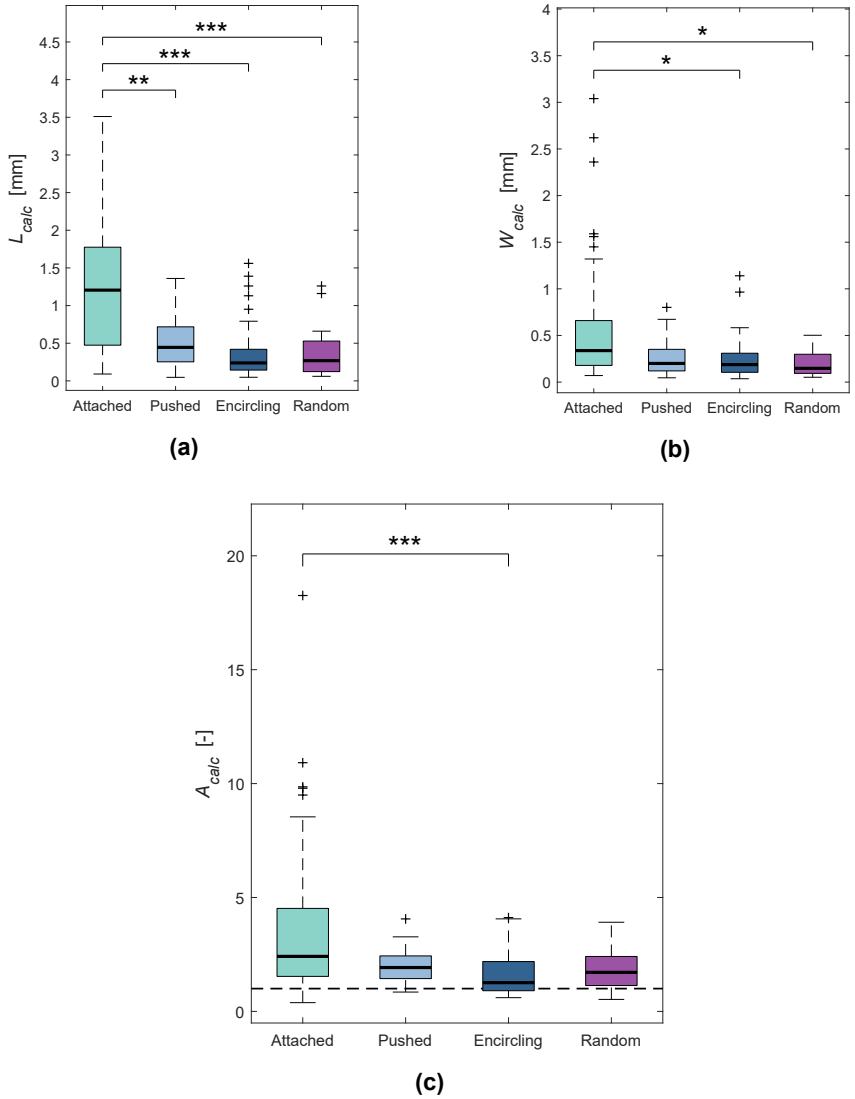

Figure 3.5: Length, width and aspect ratio of the segmented calcifications. (a) Length, measured in circumferential direction of the plaque, (b) width, measured in radial direction, and (c) aspect ratio, length divided by width. * Signifies P < 0.05, ** signifies P < 0.005 and *** signifies P < 0.0005.

Like for the location in the plaque of the calcification and its fiber pattern, the size of the calcification can be normalized, to account for the variability in plaque size between measurements. This is done by dividing the width of the calcification (W_{calc}) by the sum of the radial distances (D_{inner} & D_{outer}), as explained in Chapter 2. Values of this parameter range from 0 to 1, with the limit 0 indicating that the calcification occupies no plaque space, and the limit 1 indicating that the calcification occupies the whole width of the plaque. This parameter, combined with the aspect ratio of the calcification, describes the generalized and normalized calcifications in the plaque. Results are plotted in Figure 3.6. Calcifications with the Attached pattern show the largest range in calculated values of W_{norm}; going as low as 0.02 and as high as 0.96. The lowest value however, is found for the Pushed Aside pattern: 0.01. The highest value for the other three fiber patterns is 0.58, for the Pushed Aside pattern. The median [Q1–Q3] value for W_{norm} for all calcifications is 0.12 [0.05–0.23].

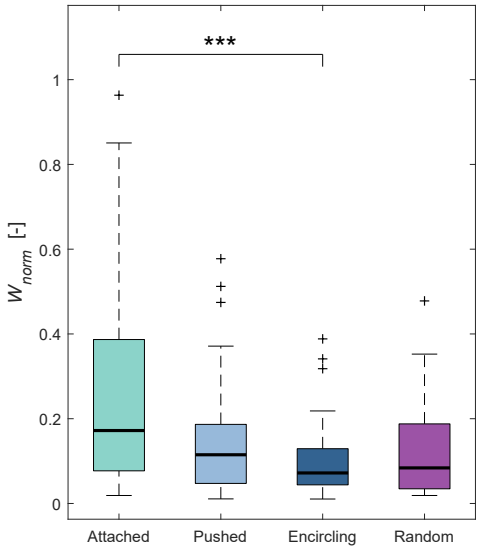

Figure 3.6: Normalized width of the calcifications (width divided by sum of D_{inner} & D_{outer}). *** Signifies P < 0.0005.

3.3.4. Cap Thickness

In literature, cap thickness is an important geometric determinant of plaque vulnerability, with 65 µm being the critical thickness value for cap thickness in coronary arteries [71], and 200 µm for carotid arteries [72]. Studies reported that calcifications close to the lumen can destabilize a plaque [43], and thus, similarly to lipid pools, cap thickness can also be defined for calcifications [55, 68]. However, no critical values (like for lipid pools) are used in literature for calcifications. Calculations of cap thickness (see Chapter 2 for definition) for the segmented calcifications are shown in Figure 3.7.

The smallest cap thickness is found for the Attached pattern, with calcifications adjacent to the lumen. Smallest cap thicknesses for the other three fiber patterns are 0.07 mm for the Encircling pattern, 0.09 mm for the Pushed Aside pattern, and 0.28 mm for the Random pattern. Cap thicknesses of the Attached pattern are significantly smaller than those of the Encircling pattern and Random pattern. The median [Q1–Q3] cap thickness for all calcifications combined is 0.96 [0.32–2.03].

3.3.5. Fiber Interaction Pattern Size

For the Attached pattern, by definition, it is not possible to measure the pattern size D_{fib}; the fibers themselves are calcified, with no observed change in their alignment in this process. Furthermore, there is no clear distance measurable for the Pushed Aside pattern and the Random pattern; both gradually change from the calcification specific fiber pattern to the main preferential orientation, which is circumferential to the lumen. Therefore, only the Encircling pattern needed to be measured; this fiber

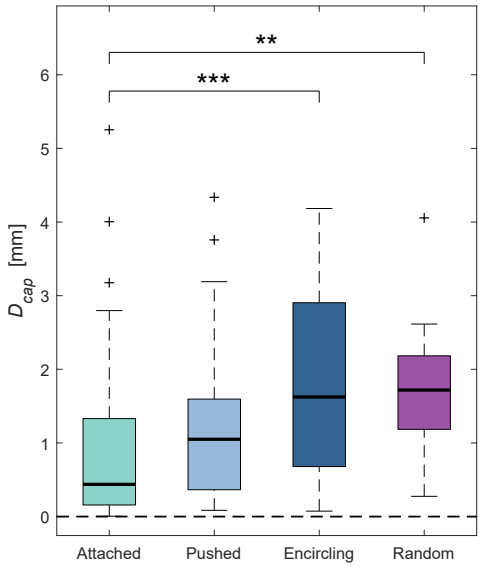

Figure 3.7: Cap thickness of fibrous tissue between calcification and lumen. Dashed line is the lumen. ** Signifies P < 0.005 and *** signifies P < 0.0005.

pattern alignment is very local with a clear transition from the encircling fibers to the main preferential orientation.

The thickness of the band of fibers encircling the calcification is measured (distance between the yellow arrows in Figure 3.1c). Thickness of this band could change moderately along the circumference of the calcification, therefore, a representative part of this fiber pattern was chosen for each measurement. Measurements of this distance are shown in Figure 3.8. From this plot it can be appreciated that the thickness of the band of the encircling fibers shows little variation for most measurements: 0.012 mm to 0.021 mm [Q1–Q3], with a median value of 0.015 mm. The thickness of this band of fibers does not correlate with the length (r_s = 0.387, P = 0.014) or width of the calcification (r_s = 0.299, P = 0.061), suggesting that this parameter does not depend on the calcification size.

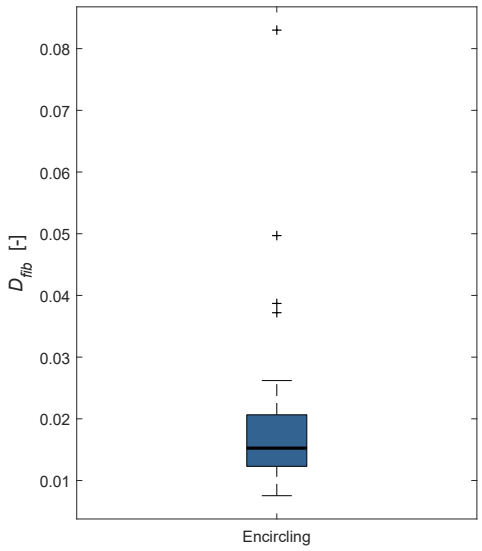

Figure 3.8: Thickness of Encircling fiber pattern.

3.4. Correlations

The Spearman's rank correlation test is used to investigate if parameters are related to each other. This test accounts for the outliers that are present in most of the parameter ranges (see the plus signs in the boxplots of this chapter) and for non-normality (skewedness of the box plots) of the data by ranking the variables first. The ranks of the data arrays of the two parameters are tested for possible correlation. The better these ranks match, the stronger is the correlation. A correlation coefficient r_s of 1 indicates perfect positive correlation (association of ranks), r_s of -1 perfect negative correlation, and r_s = 0 indicates that there is no correlation at all. However, there is no consensus for r_s values between these limits, with studies reporting values as close to zero as 0.03 as meaningful correlations [73]. In this study, r_s values < -0.500 or > 0.500 that pass the statistical significance test (P < 0.05) are reported as strong correlations.

3.4.1. Correlations for All Fiber Patterns Combined

First, the correlations of all parameters for all four fiber patterns combined are calculated. The results are shown in Table 3.1. Both measured and calculated parameters are present in this table. The calculated parameters are normalized distance (D_{norm}), aspect ratio (A_{calc}), normalized width (W_{norm}) and cap thickness (Th_{cap}) (positions 4, 7, 8 & 9 in Table 3.1 respectively).

Table 3.1: Spearman's correlation for all parameters, for the four fiber patterns combined. $|r_s|$ > 0.500 Values are highlighted in bold.

		Correlations (r_s)								
		1	*2*	*3*	*4*	*5*	*6*	*7*	*8*	*9*
1	D_{bif}	1								
2	D_{inner}	0.217*	1							
3	D_{outer}	-0.262*	-0.405*	1						
4	D_{norm}	0.282*	**0.843***	**-0.815***	1					
5	L_{calc}	-0.113	-0.140	0.168*	-0.186*	1				
6	W_{calc}	-0.064	-0.082	0.220*	-0.195*	**0.727***	1			
7	A_{calc}	-0.082	-0.120	-0.081	-0.011	**0.530***	-0.125	1		
8	W_{norm}	-0.082	-0.377*	0.057	-0.292*	**0.627***	**0.860***	-0.114	1	
9	Th_{cap}	0.207*	**0.950***	-0.467*	**0.850***	-0.302*	-0.285*	-0.060	**-0.539***	1

* Correlation is significant at the P < 0.05 level.

The longitudinal location of the calcification D_{bif} is not strongly correlated to any of the other parameters, meaning that location of the calcification in the artery does not predict its cross-sectional location, its size or shape.

Normalized distance to the lumen D_{norm} is the inner radial distance divided by the plaque thickness (sum of both inner and outer radial distance D_{inner} & D_{outer}, see Chapter 2, Section 2.2.3 for the explanation and formulas of the calculated parameters). A strong positive correlation is appreciable between D_{norm} and D_{inner} (r_s = 0.843, P < 0.0005), and a strong negative correlation between D_{norm} and outer radial distance D_{outer} (r_s = -0.815, P < 0.0005). The positive correlation means that the normalized distance increases along with inner radial distance, the second correlation is negative because D_{norm} *decreases* as D_{outer} *increases*, and hence the negative sign. This is not surprising as the inner radial distance is also a measure of distance to lumen, and the larger the outer radial distance, the smaller the inner radial distance (in general), explaining why this distance is negatively correlated to normalized distance.

Aspect ratio A_{calc} is calcification length L_{calc} divided by width W_{calc}. A moderate positive correlation is observable between A_{calc} and L_{calc} (r_s = 0.530, P < 0.0005). However, it has no correlation with

W_{calc} (r_s = -0.125, P = 0.135). This indicates that aspect ratio is moderately correlated to calcification length. Reason for this moderate correlation might be that for many cases the width of the calcification increases along with the length (r_s = 0.727, P < 0.0005), thus signifying a general increase in calcification size and thereby diminishing the separate contributions of these two parameters.

Normalized width W_{norm} is calculated by dividing calcification width W_{calc} by plaque width (sum of D_{inner} & D_{outer}). Table 3.1 shows that W_{norm} has a weak negative correlation with D_{inner} (r_s = -0.377, P < 0.0005) and no correlation with D_{outer} (r_s = 0.057, P = 0.494). However, it has a strong positive correlation with W_{calc} (r_s = 0.860, P < 0.0005), making the absolute calcification width the best predictor for the normalized calcification width. A moderate positive correlation is also observable between W_{norm} and calcification length L_{calc} (r_s = 0.627, P < 0.0005), meaning that for increasing width the length of the calcification also increases, confirming the argument made in the previous paragraph that width might increase along with length.

The cap thickness Th_{cap} is calculated by subtracting half of the calcification width W_{calc} from the inner radial distance D_{inner}, and shows a strong positive correlation with the latter (r_s = 0.950, P < 0.0005), and thus also indirectly with D_{norm} (r_s = 0.850, P < 0.0005). However, it shows a weak negative correlation with calcification width W_{calc} (r_s = -0.285, P = 0.0005). This indicates that the inner radial distance is the main driving parameter for the calcification cap thickness, and that the width of the calcification has in most cases not much influence on this thickness. A possible reason for this weak correlation is that only large values of W_{calc} correlate with the cap thickness: a small calcification can either have a small or large cap thickness, but a large width calcification which occupies most of the plaque can only have a small cap thickness. This becomes visible if W_{calc} is plotted against Th_{cap}; for large values of W_{calc} the cap thickness can only be small (Figure 3.9a), while for small values Th_{cap} can be either small or large. Normalized width W_{norm} is a better measure of how much plaque width is occupied by the calcification, and thus a better predictor of the cap thickness. This is reflected in the correlation between Th_{cap} and W_{norm}: r_s = -0.539, P < 0.0005 (versus r_s = -0.285, P = 0.0005 of Th_{cap} and W_{calc}). Normalized calcification width is plotted against cap thickness in Figure 3.9b, showing the clearer trend of decreasing values for cap thickness as calcification width increases compared to Figure 3.9a.

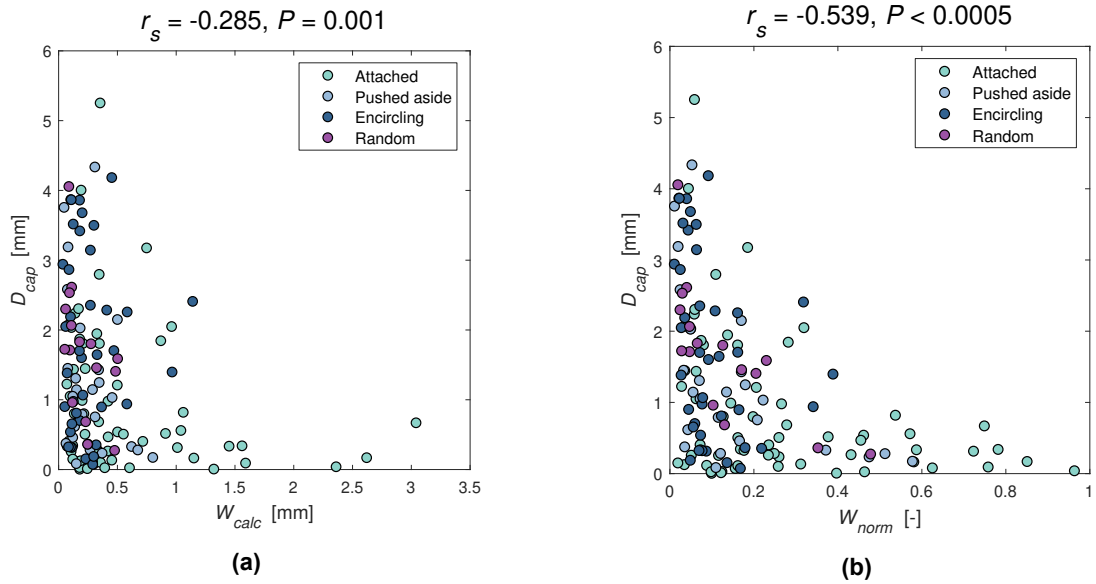

Figure 3.9: Scatter plot of cap thickness Th_{cap} versus absolute calcification width W_{calc} (a) and normalized calcification width W_{norm} (b). Corresponding correlations are shown above the graphs.

The only correlation between two independently measured parameters, although not very strong, is between calcification length L_{calc} and calcification width W_{calc} (r_s = 0.727, P < 0.0005). A scatter plot of both the parameters is shown in Figure 3.10. Both the length and the width of a calcification increase

as the overall size of the calcification increases, causing this correlation. This confirms the correlation between W_{norm} and L_{calc} (r_s = 0.627, P < 0.0005) described earlier. High aspect ratio calcifications with their long axis aligned circumferentially or radially are the cause of the outliers in the plot of Figure 3.10.

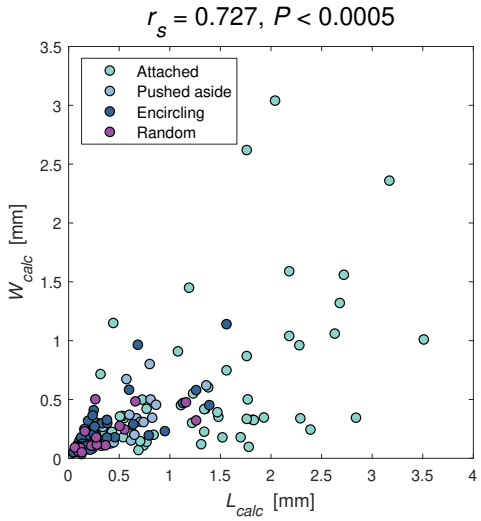

Figure 3.10: Scatter plot of calcification length L_{calc} and width W_{calc}, with the corresponding correlation shown above the graph.

3.4.2. Correlations Per Fiber Pattern

Some correlations calculated for the individual fiber patterns show results different than all patterns combined. A correlation was defined as weaker if for the individual fiber pattern r_s < 0.500 while for the grouped patterns r_s > 0.500, and stronger if for the individual fiber pattern r_s > 0.500 while for the grouped patterns r_s < 0.500. Since the Random pattern has a small sample size of only 16 segmented calcifications, correlations for this fiber pattern are less relevant. The Random pattern is therefore not addressed in this subsection. For the separate correlation tables of the four fiber patterns the reader is referred to Appendix A.

Attached pattern

The Attached pattern has three correlations that are stronger compared to the correlations of the grouped fiber patterns:

1. D_{outer} & D_{inner}: r_s = -0.515, P < 0.0005 (Increase in $|r_s|$ of 0.110)
2. W_{norm} & A_{calc}: r_s = -0.549, P < 0.0005 (Increase in $|r_s|$ of 0.435)
3. Th_{cap} & D_{outer} : r_s = -0.645, P < 0.0005 (Increase in $|r_s|$ of 0.178)

The negative correlation between D_{outer} and D_{inner} means that outer radial distance *decreases* as inner radial distance *increases*. The reason that this correlation shows up for this fiber pattern might be that the size of the plaque for the Attached pattern has less variability than for the four fiber patterns combined; the two distances added together gives the plaque thickness. See Figure 3.11a for a scatter plot of these two parameters.

Outer radial distance D_{outer} decreases as cap thickness Th_{cap} increases for this fiber pattern. This too might indicate that the plaque size for the Attached pattern shows less variability compared to the four fiber patterns combined, like it is reasoned for D_{outer} & D_{inner}. The decreasing trend between Th_{cap} & D_{outer} is plotted in Figure 3.11c.

The stronger correlation between W_{norm} & A_{calc} indicates that for this fiber pattern the *width* of the calcification is a predictor of the aspect ratio, while for all fiber patterns combined the *length* of the calcification is a predictor of aspect ratio (see Table 3.1). This relation is plotted in Figure 3.11b.

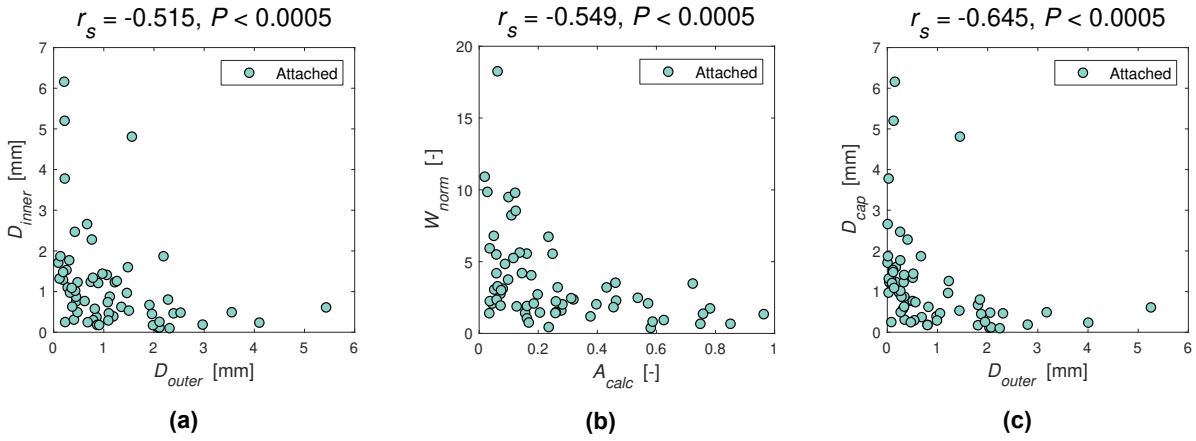

Figure 3.11: Three relevant correlations for the Attached pattern that are not present for the four fiber patterns combined. (a) Correlation between inner radial distance D_{inner} and outer radial distance D_{outer}, (b) correlation between normalized width W_{norm} and aspect ratio A_{calc}, and (c) correlation between cap thickness Th_{cap} and outer radial distance D_{outer}. Corresponding correlations are shown above the graphs.

Weaker correlations are found for A_{calc} & L_{calc} (decrease in r_s of 0.184), W_{norm} & L_{calc} (decrease in r_s of 0.198) and Th_{cap} & W_{norm} (decrease in r_s of 0.211), indicating that there are no relevant correlations for these combinations for the Attached pattern, while for the fiber patterns combined these correlations are relevant.

Pushed Aside & Encircling patterns

Correlations for these two fiber patterns are very similar to the correlations of the four fiber patterns combined. For the Pushed Aside pattern no stronger correlations are found, but one weaker correlation: relevant correlation is lost for A_{calc} & L_{calc} (decrease in r_s of 0.258). For the Encircling pattern there is no stronger correlation found either, but two small decreases: A_{calc} & L_{calc} (decrease in r_s of 0.092) and Th_{cap} & W_{norm} (decrease in r_s of 0.090).

4

Plaque Modeling Approach

Through a comprehensive morphometric analysis, profound knowledge of different types of local fibrous tissue alignment patterns, and calcification geometric features was obtained in the previous part of this project. The next step was to use this knowledge as input for the following part: the computational modeling of plaques with realistic fibrous tissue alignment patterns for structural stress and strain investigation. 2D finite element plaque models were generated, to study the effect of different collagen fiber patterns around the calcifications on interface stresses and strains, and how these stresses and strains are influenced by the calcification geometric features. Therefore, to focus on these objectives only, no other plaque components like lipid pools were included in the FE models.

Physical loading conditions were simulated as closely as possible, without introducing case-specific plaque geometries which would unavoidably give rise to geometry-specific peak stresses or strains. Calcification-specific models were created by using the unique measurements for the four main fiber patterns, resulting in 64 unique models for the Attached pattern, 25 for the Pushed Aside pattern, 40 for the Encircling pattern, and 16 for the Random pattern. Methods of constructing these models and extracting the results are discussed in this chapter. All FE modeling was performed in ABAQUS (ABAQUS/CAE, 2016, DS Simulia, Providence, RI).

4.1. Computational Model

4.1.1. Model Geometry

To impose the loading conditions on the calcifications with the local fiber patterns as realistic as possible, a representative plaque model was created. It was required for this model to be able to fit the wide measurement ranges obtained in the previous part of this study, but must also be as consistent as possible, as changing geometries, apart from the calcification and the surrounding fiber pattern, results in different loadings on this region of interest. Hence, the model was chosen to consist of 1) a subregion, which includes the calcification and surrounding fibrous tissue with corresponding fiber pattern, and 2) a macro plaque model in which the subregion was embedded. No other plaque constituents were modeled as the focus of the study was to investigate the impact of individual calcifications, and to prevent any possible influence of other plaque components. 2D cross-sectional geometries were constructed, and building of these 2D models was done in the preprocessor of ABAQUS.

Because of the 2D cross-sectional geometry, a general assumption for the third (longitudinal) direction was needed. This can be either a plane-stress or a plane-strain assumption. The plane-stress assumption is for thin structures where stress in the third dimension (out of the thin plane) is assumed to be zero, and in the plane-strain assumption it is assumed that the strain out of plane is zero. This is true for geometries for which the dimension out of plane is large (with respect to the dimension in the cross-sectional plane), and where the geometry and loading conditions do not change significantly along the third direction. Because stresses and strains at the calcification interface in the cross-sectional plane

were investigated, the plaque can be assumed as a long tube of unchanging geometry and loading, and the plane-strain assumption was used.

Macro model

The macro plaque model was generated based on the geometric measurement data of carotid arteries reported before in the literature. An idealized atherosclerotic arterial cross-section with circular structural layers was used to to represent the generic plaque shape, a visualization of such a cross-section is given in Figure 4.1.

A healthy intima layer is just one layer of cells thick, and lumen diameter measurements of healthy carotid arteries could therefore be used to determine the inner diameter of the media layer. For this an average value of 5.6 mm (average of the average values for the CCA and ICA) was found [74]. Lumen diameter was calculated assuming a stenosis level of 60% using the European Carotid Surgery Trial (ECST) method; calculating the ratio between narrowed lumen and the original diameter [75]. This resulted in a lumen diameter of 2.2 mm. Most vulnerable plaques have an eccentric stenosis [76], meaning that the lumen center has an offset from the artery center. Therefore, a representative value for this offset (eccentricity index of 0.8, see Figure 1 & 2 in [76]) was used in the plaque model, which resulted in a plaque thickness of 2.8 mm at the thickest portion of the plaque tissue (see Figure 4.1). The average wall thicknesses for the media and adventitia were found to be 0.80 mm and 0.27 mm respectively [77], yielding the diameters shown in Figure 4.1.

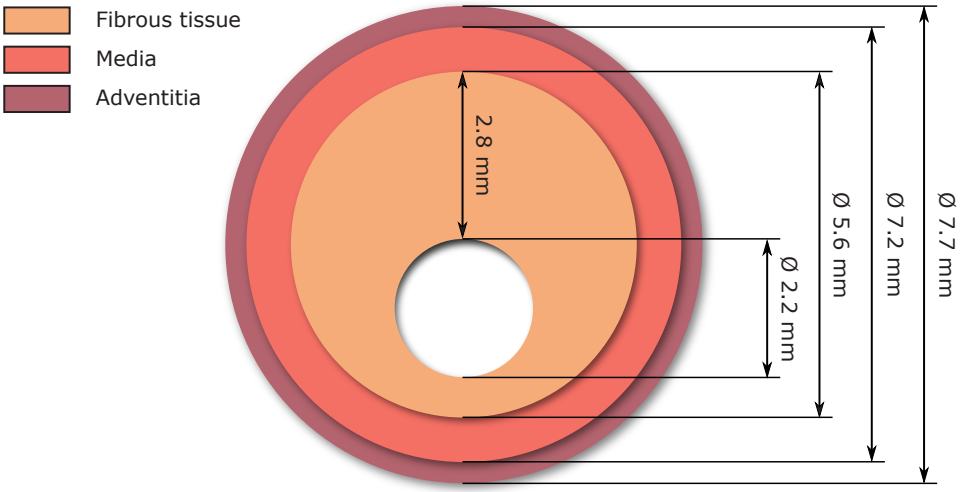

Figure 4.1: Macro geometry of the plaque, without the calcification subregion.

Subregion with calcification

The calcification and its surrounding fibrous tissue pattern was captured in a dedicated subregion. This subregion was included in the macromodel by embedding it in the midregion of the macromodel (see Figure 4.2). The size of the macromodel varied with different calc size.

The calcification was assumed to have an elliptic shape. Its size was based on the W_{norm} and A_{calc} (length is W_{norm} multiplied with A_{calc}, displayed as L_{norm} in Figure 4.2), and location on D_{norm} in the submodel. Every uniquely segmented calcification and its fiber pattern was modeled for the four main patterns, and thus 145 unique models were constructed (64 for the Attached pattern, 25 for the Pushed Aside pattern, 40 for the Encircling pattern, and 16 for the Random pattern).

The length of the straight part of the model (L_{sp} in Figure 4.2) was the calcification length multiplied with a constant factor of 1.3, to accommodate the fiber patterns. The reason for this construction was to keep the loading on the calcification constant, irrespective of the size of the calcification, which was not possible for a perfectly circular plaque as in Figure 4.1. After applying blood pressure, tensile stresses

develop in a plaque model which mainly follow the curvature of the lumen. A small calcification in such a model would then be loaded by these tensile stresses in approximately the same direction as its major axis, but for larger calcifications this loading would occur with an angle to the major axis, thereby creating different loading conditions in the two cases. Many observations in the morphometric analysis as well as observations in literature (e.g. see Figure 1D in [78]) indicate straightened segments in the plaque due to the calcifications, subsequently leading to elliptic lumen shapes and justifying the choice made for the calcification subregion in this study. Furthermore, the average lumen area for the FE models was 15.1 mm^2 (standard deviation of 11.9 mm^2), which is comparable with *in-vivo* measurements of highly stenotic lumen areas: 17.0 mm^2 (10.6 mm^2) [79]. The plaque geometry is symmetrical, and therefore only half of the plaque cross-section had to be constructed in ABAQUS.

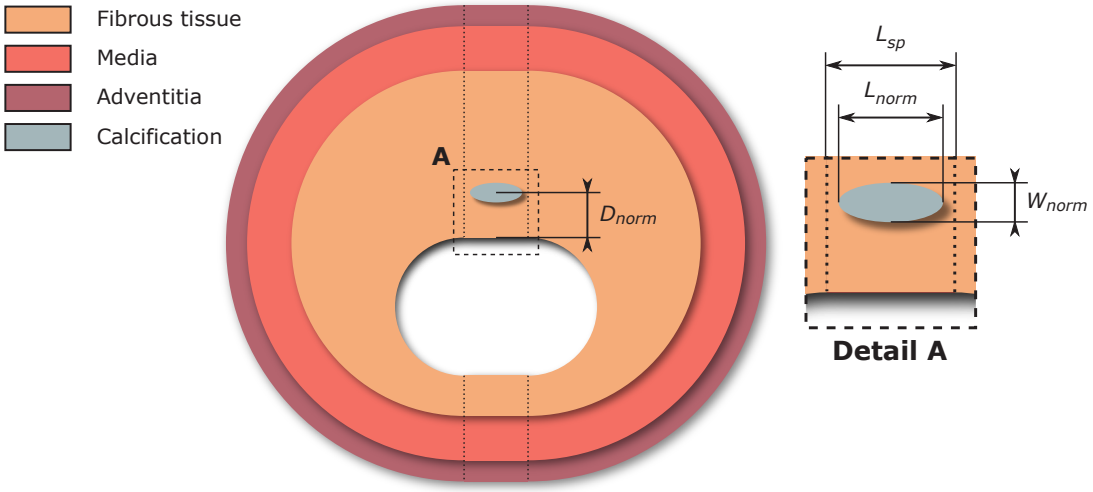

Figure 4.2: Plaque model, including the variable region of interest. The region between the dotted lines is the straight plaque.

4.1.2. Material Models

Arterial walls & fibrous tissue

Arterial walls and the thickened intima (the fibrous tissue) show a non-linear stress-strain response, and due to fluid being trapped in the structure, are nearly incompressible [80]. Collagen fibers are highly prevalent in all three layers of the atherosclerotic artery (adventitia, media & thickened intima), and cause these three layers to be anisotropic in stiffness. Many (calcification) modeling studies describe the anisotropic non-linear fibrous tissue as isotropic and hyperelastic (e.g. see [64]), and some introduce anisotropy by using a linear elastic orthotropic material, with a separate stiffness modulus for the radial and circumferential direction of the plaque (e.g. see [55]). Few studies [57, 70] combine both anisotropy and hyperelasticity, by using the Holzapfel-Gasser material model, which combines both material behaviours.

The Holzapfel-Gasser material model was used in this study, with a strain energy density function formulated as follows:

$$\Psi = \Psi_{iso} + \Psi_{aniso} \tag{4.1}$$

where Ψ_{iso} describes the isotropic matrix material response of the fibrous tissue, and Ψ_{aniso} describes the embedded fibers contribution. The two terms are specified as follows:

$$\Psi_{iso} = \frac{\mu}{2}\left(I_1 - 3\right), \tag{4.2}$$

$$\Psi_{aniso} = \frac{k_1}{2k_2}\left(\exp\left\{k_2\left[\kappa\left(I_1 - 3\right) + \left(1 - 3\kappa\right)\left(I_4 - 1\right)\right]^2\right\} - 1\right). \tag{4.3}$$

I_1 is the first invariant (trace) of the right Cauchy-Green deformation tensor, and $I_4 = (\lambda_1 \cos\alpha)^2 + (\lambda_2 \sin\alpha)^2$ is a pseudo invariant, where λ_1 & λ_2 are the stretch ratios along and across the fibers respectively, and α is the local fiber angle in the cross-sectional plane. Fibers in the matrix can have a dispersion, and this is captured in the parameter $\kappa \in [0, 1/3]$. If κ = 0 the fibers are perfectly aligned, and if κ = 1/3 the fibers are completely dispersed, effectively making the material isotropic (but still hyperelastic). μ, k_1 & k_2 are material constants. μ is the shear modulus, and is related to linear stiffness modulus for small deformations via $E = 2\mu(1+\nu)$, with ν being the Poisson's ratio. For incompressible materials (ν = 0.5) this relation reduces to $E = 3\mu$. The stiffness of the fibers is determined by k_1 and k_2. Values for the material constants for the media and adventitia were obtained from Akyildiz *et al.* [38], and for fibrous tissue values from Douglas *et al.* [70] were used. See Table 4.1 for the values for each respective artery layer.

Calcification

A linear elastic material model (Hooke's law) was used to describe the stiffness response of the calcification, its stiffness value, or E modulus, was chosen from the nano indentation study of Ebenstein *et al.* [81]. A wide range for the stiffness modulus was found in this study, but the lower values might be caused by accidental indentation of fibrous tissue remnants that were still attached to the calcifications, and thus a value of the upper part of this range was chosen. The calcification was further assumed to be (nearly) incompressible. See Table 4.1 for the stiffness modulus E and Poisson's ratio ν of the calcification.

Table 4.1: Tissue material parameters used for the constitutive relations in the plaque model.

Tissue	E (GPa)	ν	μ (kPa)	k_1 (kPa)	k_2	κ
Adventitia			5.86	2069.42	394.28	0.20
Media			2.24	65.76	76.87	0.27
Fibrous tissue			56	41080	1749.6	0.136
Calcification	2	0.49				

4.1.3. Fiber Implementation

The fiber material model defined by Equation 4.3 has a fiber angle α as variable in the invariant I_4, this fiber angle is the orientation of the collagen fibers in the arterial walls and fibrous tissue. A description of the fiber orientation for each of the four main patterns was therefore needed to complete the material implementation in ABAQUS.

Fiber orientation in macro model

For the adventitia and media the fibers were aligned circumferentially with the walls themselves, and for the fibrous tissue the fibers were aligned concentric with the lumen, as this was found to be the preferred orientation in literature [70]. The global fiber orientations for the circular part of the plaque model were implemented using local circular coordinate systems, one concentric with the adventitia and media, and one concentric with the lumen. The straight (variable) part of the model had a parallel fiber orientation, tangent with the fibers of the circular (fixed) part of the model. See the left part of Figure 4.3 for the global fiber orientation.

Fiber alignment in subregion

The global orientation in the variable straight part of the plaque (region of interest) was aligned with the lumen and thus horizontal. At the interface with the embedded calcification this horizontal alignment was altered, depending on the fiber pattern type.

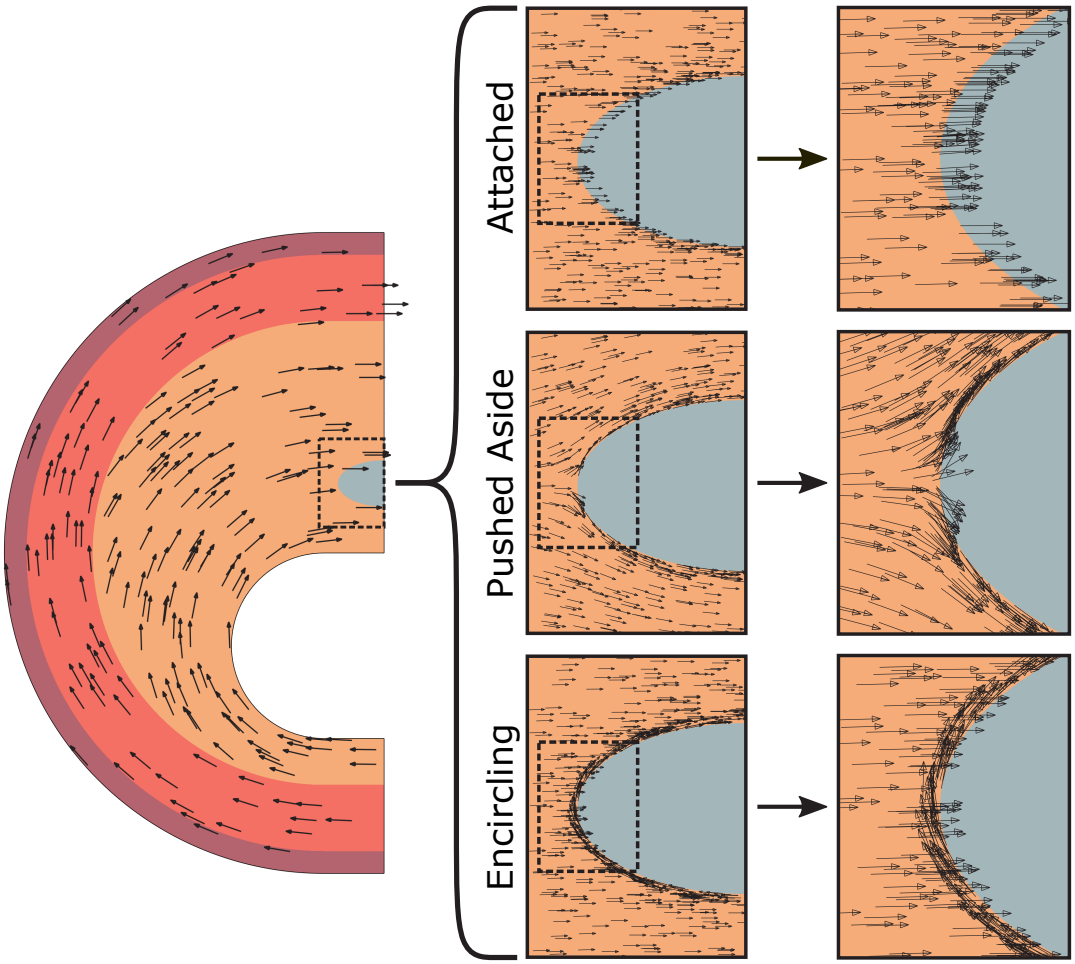

Figure 4.3: Global and local orientation of the collagen fibers in the plaque model, with black arrows indicating the orientation. Left part of the figure: global orientation for adventitia, media and intima (fibrous tissue). Right part of the figure: local orientation for the Attached pattern (top), Pushed Aside pattern (middle), and Encircling pattern (bottom). The random pattern is not shown in this figure.

For the Attached pattern there was no need to change the global orientation locally; as it is explained in the morphometric analysis in Chapter 3, Section 3.1, the global or main fiber orientation is not disrupted by the calcification. The fibers run past the calcification at the radial sides (side close to the lumen and side far from the lumen), and end up at the calcification at its circumferential sides. The right side of Figure 4.3 shows close ups of the unaltered global orientation at the calcification interface.

The Pushed Aside pattern is characterized as a calcification being embedded between fibers. Calcifications grow in size over time, and for this pattern a possible explanation for its appearance is that this growing pushes the collagen fibers in which it is embedded aside. To mimic this pattern, solutions from potential flow theory were used. In potential flow theory, analytical solutions can be obtained for frictionless, irrotational (no vorticity) and incompressible flows around obstacles, by defining a potential function $\phi(x, y)$ and a stream function $\psi(x, y)$ (in case of a 2D flow field). The stream function describes streamlines of the fluid around the obstacle, and the potential function describes velocity potential lines, which are perpendicular to the streamlines. Analysis of this flow is done via a technique called conformal mapping, where these two functions are combined in $w(z) = \phi + i\psi$, where $z = x + iy$ and i is the imaginary unit. Fiber orientation could then be obtained by calculating the angle between the vertical velocity u and horizontal velocity u of the flow velocity field:

$$\frac{\mathrm{d}w}{\mathrm{d}z} = u - iv. \tag{4.4}$$

The starting point is a potential flow field of a horizontal free stream obstructed by a circle, and is defined

by the following formula:

$$w(z) = V_\infty \left(z + \frac{R^2}{z} \right), \tag{4.5}$$

where V_∞ is the free stream velocity and R the radius of the circle. An example of streamlines for a flow around a circular obstacle is plotted in Figure 4.4a. As calcifications are assumed to be elliptic, a solution is needed for a potential flow over an ellipse. This is done by transforming the solution for a circle into a flow over an ellipse. Such a transformation can be done through a Joukowski transformation, and is done by transforming $z = x + iy$ to $\zeta = \chi + i\eta$ via:

$$\zeta(z) = z + \frac{\lambda^2}{z}, \tag{4.6}$$

where λ is the transformation parameter which determines the resulting shape of the circle. For a transformation to an ellipse λ is related to the ellipse semi-major axis a, semi-minor axis b and circle radius R via:

$$a = R + \frac{\lambda^2}{R} \tag{4.7}$$

$$b = R - \frac{\lambda^2}{R}. \tag{4.8}$$

For a given ellipse length and width the unknown transformation factor λ and corresponding circle radius R can be calculated with these two functions.

A transformation of the circle in Figure 4.4a to an ellipse is shown in Figure 4.4b. Potential flow calculations and Joukowski transformations were performed in MATLAB using a custom made script. This script read the geometry of the straight variable part of the ABAQUS model, its calcification and the centroids of the mesh elements in this part. The coordinates of this geometry were in the ζ-plane (the calcification is an ellipse), and via inverse Joukowski transformation the coordinates of the geometry were transformed to the z-plane (where the calcification is a circle). A potential flow was subsequently simulated over the circular calcification (Equation 4.5). Velocity components were then derived (Equation 4.4) and fiber angles calculated. The fiber angles could then be incorporated in the original mesh element coordinates in the ζ-plane, after which a new input file for ABAQUS was written by the script containing the fiber orientations. An example of this is shown on the right side in Figure 4.3, where the

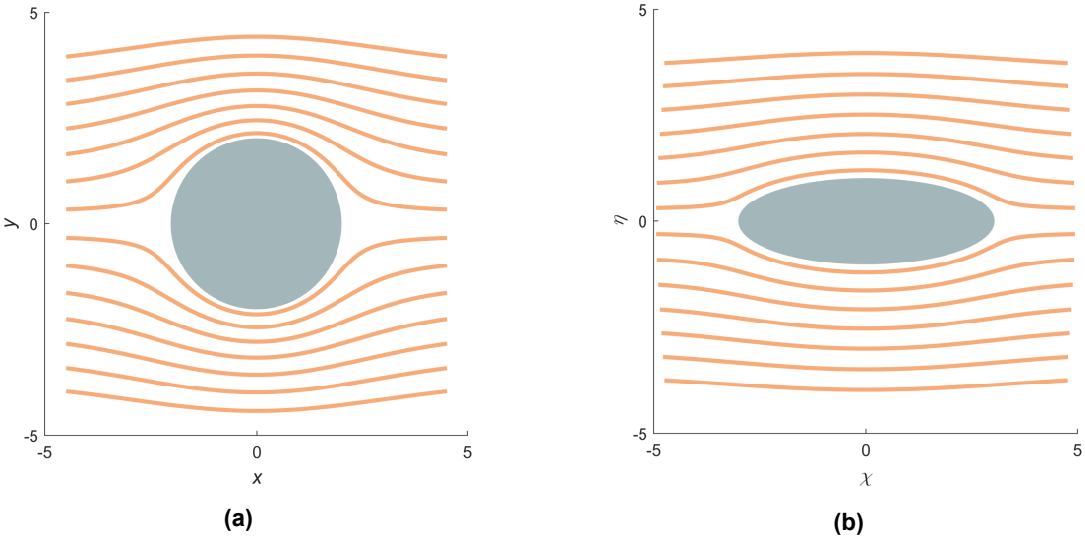

Figure 4.4: Potential flow streamlines of a free stream obstructed by a circular shaped object (a), and an ellipse shaped object (b).

black arrows indicate the angle between velocity components u & v, and are tangent to the streamlines as shown in Figure 4.4a & Figure 4.4b. For background information on potential flow theory and derivation of the formulas presented in this section, the reader is referred to Appendix B.

The Encircling fiber pattern was defined as a layer of fibers around the interface of the calcification, of which the fiber orientation was tangent to the calcification boundary. The thickness of this layer has little variability (Chapter 3, Section 3.3.5), and this variability does not depend on either calcification length (Spearman's rank correlation: r_s = 0.387, P = 0.014) or width (r_s = 0.299, P = 0.061). Therefore, the median value of 0.015 mm was chosen for all FE models for this fiber pattern. The right part of Figure 4.3 shows an example of this fiber pattern in a ABAQUS model.

Randomly oriented fibers, as observed in the fourth main fiber pattern, can be modeled by setting the dispersion parameter κ in the material model in Equation 4.3 to 1/3, making the material isotropic. This was done for the straight region of interest of the model, while the rest of the model still kept its global orientation. This situation can be compared to most of the calcification studies, which used an isotropic hyperelastic material model for the fibrous tissue.

4.1.4. Mesh

Element type

To capture peak stresses accurately at the curved calcification-tissue interface, quadratic elements were used. These elements have three interpolation points at each edge, and follow the curvature of the calcification interface therefore more accurately than same-sized linear elements, which only have two interpolations points per edge. Meshing of the plaque model was done using quadrilateral elements, which are not sensitive to overly stiff behaviour like triangular elements. As incompressible materials were used, hybrid formulation had to be selected to calculate hydrostatic pressure separately, which is normally calculated via volume change of the elements. For efficiency, the reduced integration scheme is used. This resulted in CPE8RH (continuum, plane strain, 8-node, reduced integration, hybrid formulation) elements.

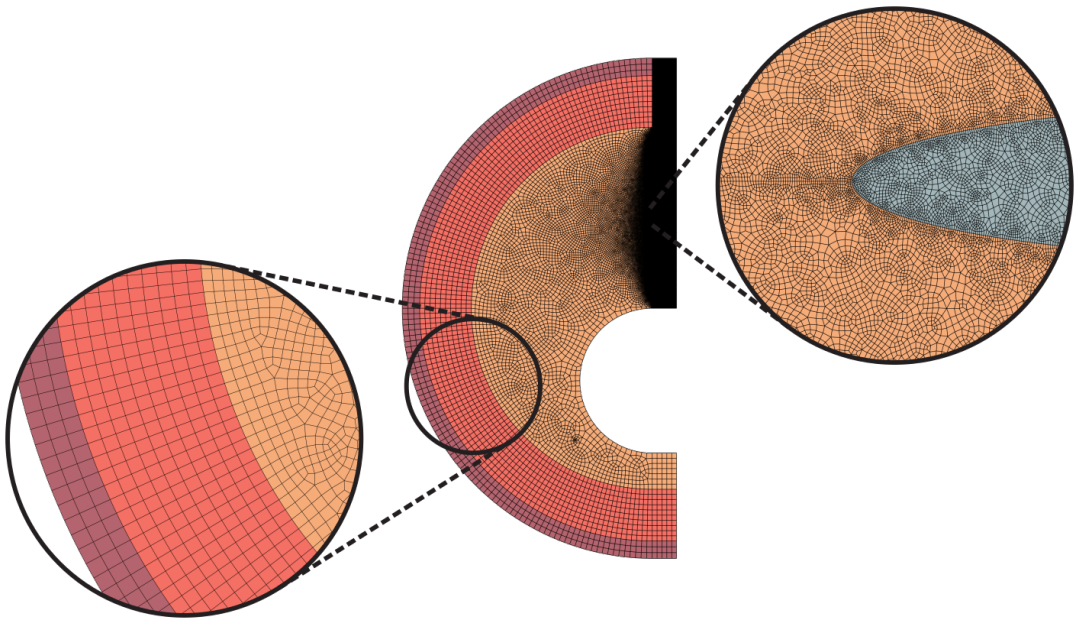

Figure 4.5: Example of a meshed model with a high aspect ratio calcification. Detail views show the larger global element size (left) and small local element size, with even smaller element size at the tip of the calcification (right).

Element size

An element size of ~0.1 mm was chosen for the macro (circular) part of the model, a smaller element size for the subregion with the calcification and the mesh was further refined at the calcification-tissue border, depending on the size of the calcification (~20 µm for the largest calcification, ~0.2 µm for the smallest calcification). For greater calcification aspect ratios the mesh density at the tip of the calcification was even further increased, to capture high curvature accurately. If the calcification was close to the lumen, a higher mesh density was applied between the lumen and the calcification. An example of a small high aspect ratio calcification and its corresponding mesh is given in Figure 4.5. For more example meshes, the reader is referred to Appendix C.

4.1.5. Loading & Boundary Conditions

A static pressure loading of 18.7 kPa was applied uniformly to the lumen of the models, representing an intraluminal peak-systolic pressure of 140 mmHg. The quasi-static implicit solver was used to calculate the deformation and stresses in the model. A symmetry boundary condition was applied to the vertical centerline. Only vertical displacement in y direction was allowed along this edge to maintain this symmetry. Furthermore, the top point on this edge was fixed for all displacements and rotations, to prevent rigid body motions. See Figure 4.6 for a plaque model with its loading and boundary conditions visualized.

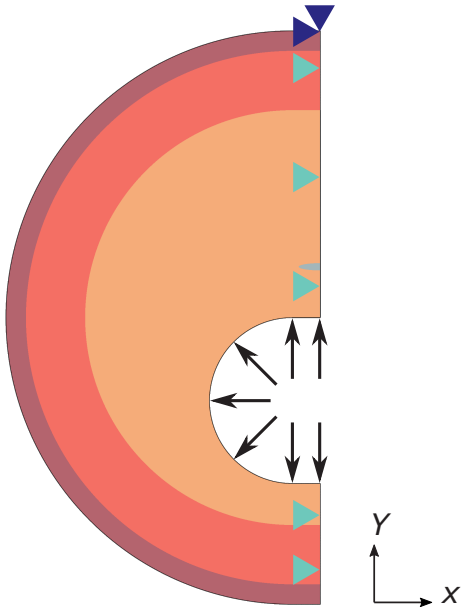

Figure 4.6: Loading and boundary conditions on the plaque model. Black arrows are the intraluminal pressure, light blue arrowheads are the symmetry boundary condition and the dark blue arrowheads represent the fixed point to prevent rigid body motions.

4.1.6. Stress & Strain Extraction

The focus of this study was stresses at the interface between the calcification and the fibrous tissue, where rupture might initiate. Calcifications are assumed to be much stronger than the surrounding fibrous tissue, and stresses were thus extracted at the fibrous tissue side of this interface. In ABAQUS, a path was created along the interface, and stress values extracted along this path. Path distance was normalized, starting at 0 at the lower side of the calcification and ending at 1 at the upper side of the calcification (see Figure 4.7).

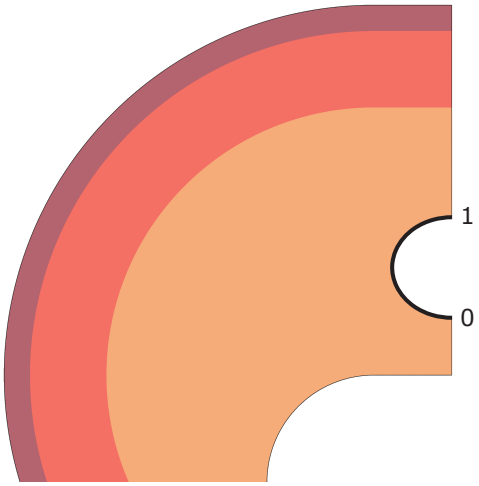

Figure 4.7: Normalized path in the fibrous tissue at the calcification interface. 0 Is the starting point, 1 is the end point. Calcification is removed from the geometry.

The failure mechanism of fibrous tissue is unknown, and for this reason there is no consensus on what stress metric to use as failure criterion [51]. For the same argument, also strain metrics can be reported here. Therefore, various stress and strain metrics were extracted at the interface, which are listed below:

Stress
- $S_{MaxPrin}$
- S_{11}
- S_{22}
- S_{12}
- S_{Mises}

Strain
- $E_{MaxPrin}$
- E_{11}
- E_{22}
- E_{12}

The 1 direction was defined along the fibers, and 2 across the fibers. These directions were thus unique for each fiber pattern, and local. For the random pattern the 1 and 2 directions were the circumferential and radial directions, as this was an isotropic material without defined local fiber orientation. It can be reasoned that there are different ways in which the fibrous tissue might fail, caused by different stress/strain components. Cartoons of these different mechanisms are shown in Figure 4.8. Over-stretching of fibers is caused by stress/strain in the 1 direction: S_{11} & E_{11} (Figure 4.8B), pulling apart of the fibers is caused by stress/strain in the 2 direction: S_{22} & E_{22} (Figure 4.8C), and a shearing or sliding of the fibers, caused by shearing stress/strain: S_{12} & E_{12} (Figure 4.8D).

Von Mises stress S_{Mises} and maximum principal stress and strain ($S_{MaxPrin}$ & $E_{MaxPrin}$) are failure criteria calculated from the stress or strain tensor. Maximum principle stress or strain are commonly used for failure of brittle materials, where the principal stress or strain reaches the failure value for that material in an uniaxial tension test. Von Mises stress is a energy density measure. It assumes that material fails when the stored distortion energy exceeds the maximum amount of distortion energy that can be stored in the material during an uniaxial tensile test, before failure occurs.

The stress tensor for incompressible materials is composed of two parts: the hydrostatic pressure and the deviatoric stress, and is formulated as follows:

$$\boldsymbol{\sigma} = \begin{bmatrix} \sigma_{11} & \sigma_{12} & \sigma_{13} \\ \sigma_{21} & \sigma_{22} & \sigma_{23} \\ \sigma_{31} & \sigma_{32} & \sigma_{33} \end{bmatrix} = -p\mathbf{I} + \mathbf{S}. \tag{4.9}$$

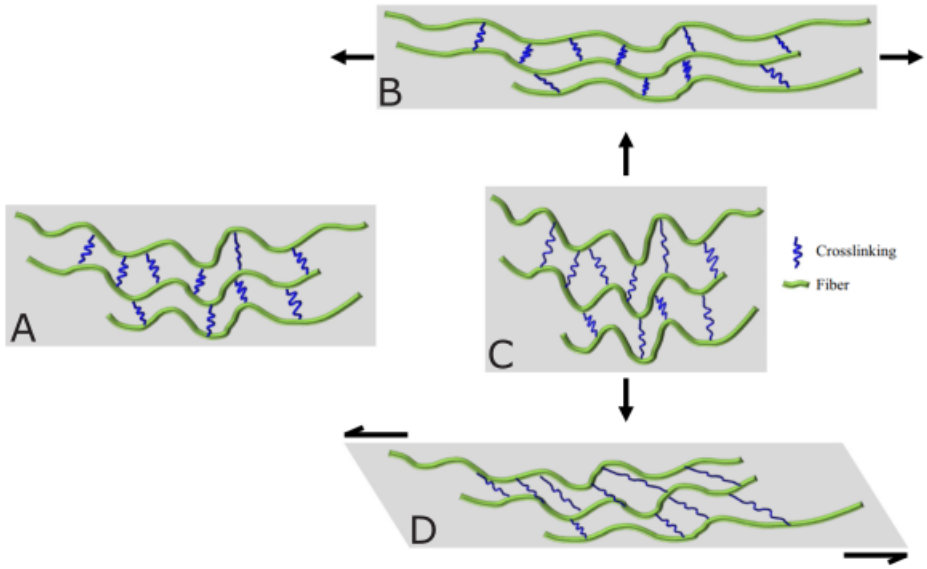

Figure 4.8: Different failure mechanisms for fibrous tissue. A) material at rest, B) overstretching of the fibers, C) pulling apart of the fibers, and D) shearing between fibers. Figure adapted from [70].

The hydrostatic pressure p is the average of the three normal stresses acting on an element: $-\frac{1}{3}\,\mathrm{tr}\,(\boldsymbol{\sigma})$ and is multiplied with the identity matrix $\mathbf{I}$. In compressible materials, the hydrostatic pressure term p is related to volume change. However, the plaque tissue is incompressible, and thus all deformations in this tissue are caused by the *distortional* part of the stress tensor: the deviatoric stress $\mathbf{S}$. As this study focused on stresses and strains that cause damage, only the deviatoric part of the stress was analyzed. ABAQUS on default reports the stress tensor $\boldsymbol{\sigma}$, so the hydrostatic pressure p had to be manually subtracted from stress metrics $S_{MaxPrin}$, S_{11} & S_{22}. Von Mises stress is already based on the deviatoric part only, and is calculated as follows: $S_{Mises} = \sqrt{\frac{3}{2}\mathbf{S} : \mathbf{S}}$.

4.2. Data Analysis

The interface paths and the corresponding values for each of the nine stress and strain metrics were stored in Microsoft Excel spreadsheets, which were then read in MATLAB for further analysis using the statistics toolbox. Peak values of the nine stress and strain metrics were extracted from the paths, along with the location of this value along this interface path.

As the tissue is unlikely to fail due to compressive stress, only positive values were reported for the metrics. For the shearing between fibers the sign of the peak value is not important, and it is to be noted that Von Mises stress is always positive.

Peak stress and strain results were visualized in box plots (Q1, median & Q3) with whisker lengths of $1.5\times$ interquartile range (Q3 - Q1). Distinction was made between fiber patterns. The Kruskal-Wallis H test was used to determine if there were significant differences between fiber patterns.

One hundred forty-five unique FE models were constructed, all with unique calcification geometric features (D_{norm}, W_{norm} & A_{calc}). To analyze what effect these geometrical features had on the stress and strain outcomes, multiple regression models were constructed where the three geometric parameters were used as predictors for the stress/strain metric outcomes. These models were equations where the stress or strain was the outcome, and the three parameters were the independent variables predicting the outcome. The null hypothesis in these models was that a term had no contribution to the stress or strain outcome, and a t-test was used to test this null hypothesis. An F-test was used to test the general goodness of fit of the regression model, where the null hypothesis was that the fit of the calculated

model is the same as the fit of a model without predictive terms (a constant term in the equation only).

Regression models for different metrics could be the same if the different metrics showed the same response to changes in the three parameters, so a Pearson correlation test (r_p) between the peak values of the nine metrics was performed beforehand. r_p values range from -1 to 1, r_p = -1 indicates perfect negative correlation, r_p = 1 perfect positive correlation and r_p = 0 no correlation at all.

The predictors (D_{norm}, W_{norm} & A_{calc}) have different data ranges: D_{norm} and W_{norm} have a theoretical range of [0,1], and A_{calc} starts at ~0.6 and goes up to ~18. Hence, the parameters were standardized by taking the z-score. This way, the coefficients in the regression model could be directly compared to each other: if, for example, the coefficient for A_{calc} was twice as large as for D_{norm} in predicting Von Mises stress, it means that the effect of A_{calc} was twice as large compared to D_{norm}.

An extra set of four FE models were created, all with the same dimensions for the plaque and calcification, but with as difference the four patterns, to identify the impact of fiber pattern on stress and strain metrics only. For W_{norm} the median value of all four fiber patterns combined was chosen: 0.12, combined with a common high value for aspect ratio (A_{calc} = 3.9) and placed close to the lumen (D_{norm} = 0.15). These last two aspects are deemed to make a plaque more vulnerable [43, 46]. A fifth model was created with the same plaque dimensions, but without a calcification, where the fibers where aligned with the lumen everywhere. This model was used to compare the peak stress at the lumen with the peak stress at the interface of the other four models.

5

Modeling Results

In this chapter the results to answer the main questions will be presented: how to asses the influence of local anisotropy of the fibrous tissue on the plaque biomechanics at the interface of the calcification, using stress/strain metrics identified in Chapter 4, and secondary to this the influence of the calcification geometric features. The morphometric analysis (see Chapter 3) provided the essential geometric information for the FE models, and three parameters, normalized with respect to plaque size, were used to construct 2D FE models of plaque cross-sections (see Chapter 4). Each individual measurement corresponding to the four main patterns was modeled, and thus 145 unique models, each containing a unique calcification, were build. Peak values for the nine biomechanical metrics and their corresponding locations will be presented, and multiple regression models where stress and strain is predicted by the driving parameters will be constructed. This chapter will first present a direct comparison between the four main fiber patterns, to asses the impact of fiber pattern on a subset of the nine metrics for the same calcification geometry.

5.1. Influence of Fiber Pattern

The 145 unique measurements and corresponding models do not allow for a direct comparison between the four main fiber patterns. Therefore, four additional models, sharing the same geometry, were created, in which only the fiber pattern at the calcification interface was different. The calcification had a normalized distance D_{norm} of 0.15, a normalized width W_{norm} of 0.12 and an aspect ratio A_{calc} of 3.9 (see Section 4.2 in Chapter 4). A fifth model, with the same geometry but without a calcification, was created to obtain relevant lumen stresses as a comparison to interface stresses. Fibers are aligned with the lumen throughout the whole fibrous tissue for this model.

Only a subset of the stress metrics was chosen for this direct comparison; those that can be most easily interpreted in relation to failure of the material, and could serve as illustration of the directionality of the stresses (compression and stretching of the fibers): Stress along fibers (S_{11}), stress across fibers (S_{22}) and shear stress between fibers (S_{12}). Stresses for the whole normalized extraction path (see Section 4.2, Chapter 4) are plotted, together with the maximum stress at the lumen.

The comparison models and the stress extraction at the lumen and calcification interface for the Attached pattern are visualized in Figure 5.1. On the left of this figure the model geometries are shown, with on the top row the fifth model without calcification for lumen stress extraction, and on the bottom row the model with calcification. The center section of the figure shows the stress contour plots for stress along fibers S_{11}, with the stress path starting and ending points indicated with a 0 and 1 respectively. The lumen stress path is shown in the top row, and the calcification interface stress path is shown in the bottom row. A high stress region is visible at the lumen, caused by the intraluminal pressure and the curvature of the lumen. The stresses extracted at the normalized paths are visualized at the right section of the figure, showing the high stress at the curved section of the lumen (top row) and a high stress concentration at the calcification interface (bottom row). The location of this peak stress

corresponds with the tip of the calcification. Due to the small scale of this peak stress region, it is not clearly visible in the stress contour plot.

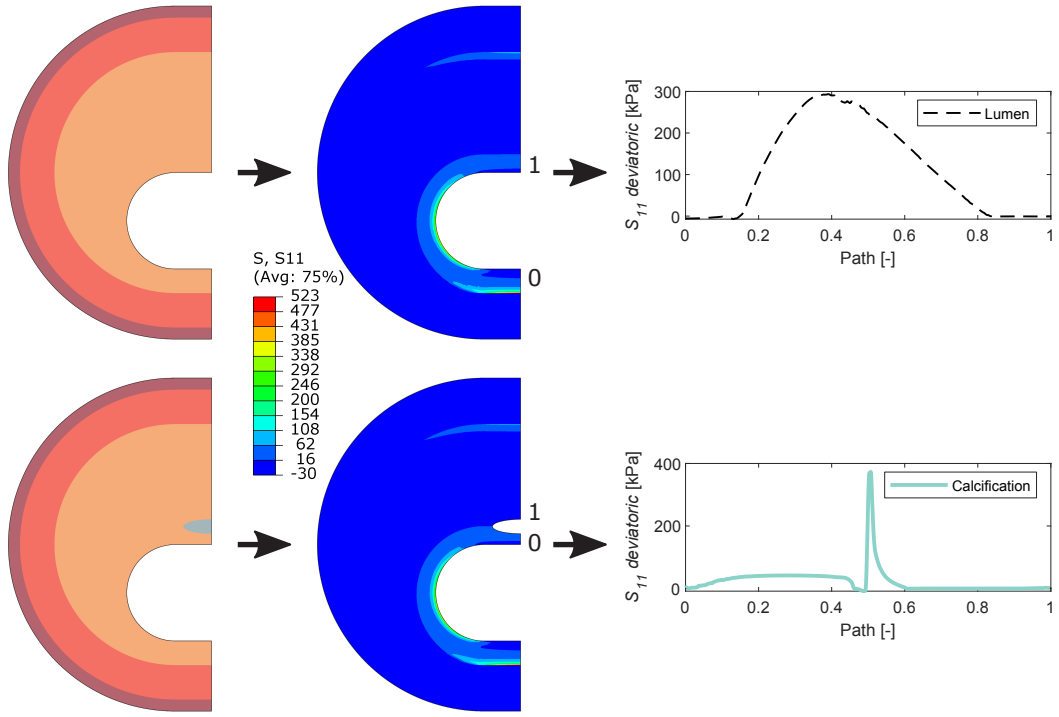

Figure 5.1: Stress extraction for the comparison models. Left section: model geometry, middle section: stress contour plots for stress along fibers, and right section: stress paths for lumen stress and calcification interface stress.

5.1.1. Deviatoric Stress Along Fibers

Stress along fibers S_{11} at the interface of the four fiber patterns, and the maximum value attained at the lumen are plotted in Figure 5.2. For this stress the positive peak values are assumed to cause the damage (overstretching of the fibers), and this stress is thus compared to the maximum positive value at the lumen: 293 kPa. From the lower center of the calcification (normalized path distance of 0) towards the upper center (path distance of 1) S_{11} has low values up to a distance of ~0.5, where peak values are observed for all four fiber patterns.

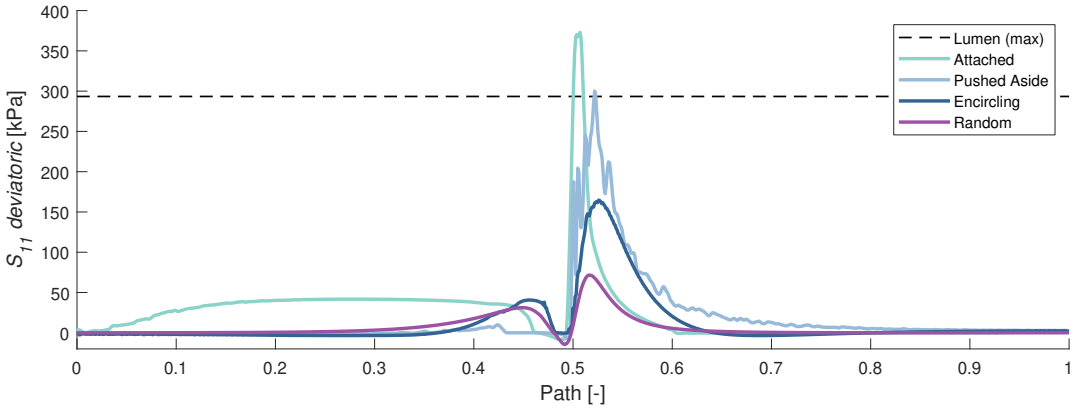

Figure 5.2: Comparison of stress along fibers (S_{11}) between the four fiber patterns, and in relation to the lumen stress.

A large difference in stresses can be observed, with the largest interface stress for the Attached pattern (373 kPa), followed by the Pushed Aside pattern (300 kPa), then the Encircling pattern (165 kPa), and the smallest value for the Random pattern (72 kPa). A possible explanation for this order is that the high stiffness fibers of the Attached pattern are most closely aligned with the circumferential stretch of the plaque, followed by a less close alignment of the Pushed Aside and Encircling pattern. The Random pattern has no alignment at all, and the fibers of this pattern experience the least amount of stretch at the interface. The Attached and Pushed Aside pattern have interface stresses as large or larger than the maximum stress at the lumen for this metric and specific geometry, indicating that the stress at the interface can exceed the stress at the lumen.

5.1.2. Deviatoric Stress Across Fibers

Stress across fibers for the four fiber patterns and the lumen are plotted in Figure 5.3. For this stress the positive peaks correspond with stretching of the matrix material in which the fibers are embedded, thereby pulling the fibers apart. It is assumed that the material fails this way, and not due to compression of the tissue (negative peak values).

From Figure 5.3 it can be appreciated that the magnitudes of the negative peaks are larger than those of the positive peaks. However, the small positive peaks can still be larger than the largest positive peak value attained at the lumen (5.8 kPa), with the largest peak belonging to the Random pattern (16.1 kPa), followed by the Pushed Aside (9.0 kPa) and Attached pattern (8.9 kPa). The Encircling pattern has a peak value (0.6 kPa) lower than the peak value at the lumen. Blood pressure in the lumen results in compressive stresses in radial direction throughout the plaque, resulting in the higher negative peaks observed in Figure 5.3. The peaks are in general lower than the peaks for stress along fibers, as fibers are the load bearing structures in reinforced materials, not the matrix in which the fibers are embedded. Again, the maximum values are attained close to a normalized path distance of 0.5.

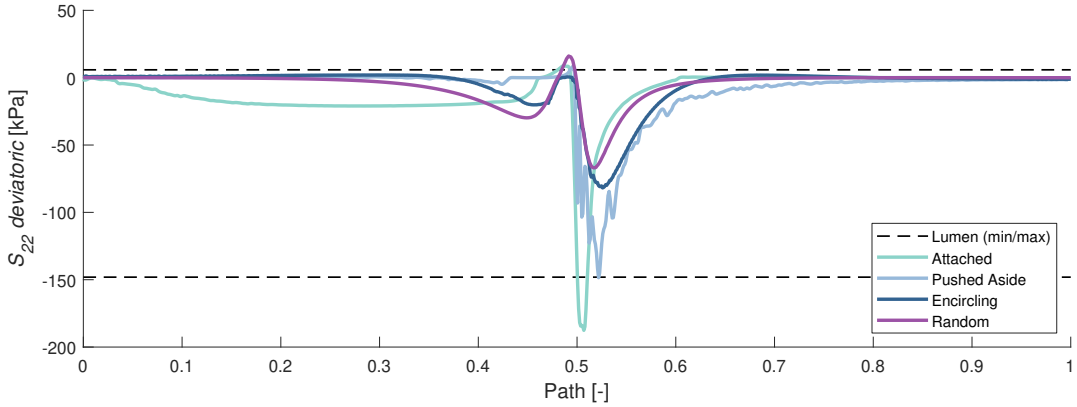

Figure 5.3: Comparison of stress across fibers (S_{22}) between the four fiber patterns, and in relation to the lumen stress.

5.1.3. Shear Stress Between Fibers

The shear stress between fibers for the four fiber patterns and for the lumen are plotted in figure 5.4. For this stress metric the maximum absolute value is important, as it is assumed that the direction of the shearing does not play a role in the material failure. It can be observed in Figure 5.4 that for all fiber patterns both the positive peak and the negative peak are much larger than the maximum value (3.5 kPa) and minimum value (-4.2 kPa) attained at the lumen for this metric. The Random pattern has the largest absolute peak (81.0 kPa), followed by the Attached pattern (72.0 kPa), Pushed Aside pattern (56.3 kPa), and the smallest value for the the Encircling pattern (31.5 kPa). A possible explanation for the low shear stress at the lumen is that the fibrous tissue is compressed uniformly in radial direction there, the material only having a normal loading component (the blood pressure). At the interface of the calcification the stress state becomes more complex, giving rise to shear stresses as well.

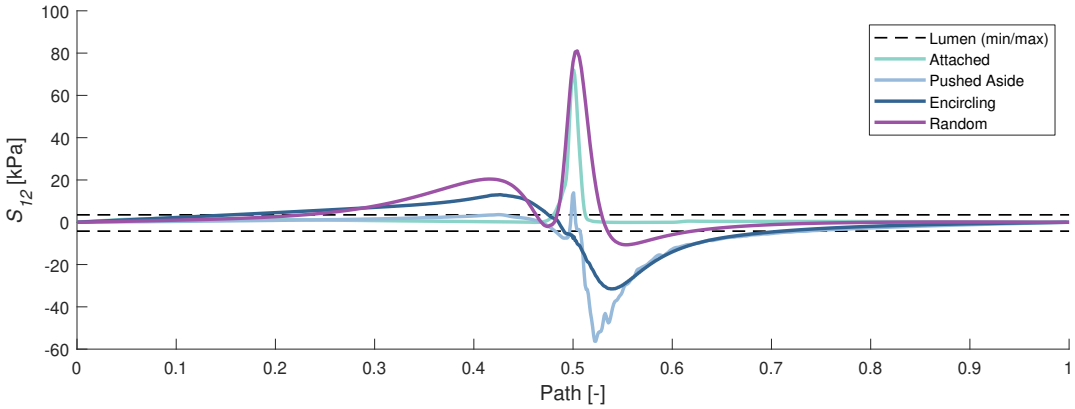

Figure 5.4: Comparison of shear stress between fibers (S_{12}) between the four fiber patterns, and in relation to the lumen stress.

5.2. Peak Stress and Strain

The highest stress and strain values at the interface are extracted from the 145 models, for some metrics (maximum principal stress & strain, stress & strain in 1 direction and stress & strain in 2 direction) only the highest positive values were extracted and for the other metrics (shear stress & strain, and Von Mises stress) the highest absolute values were extracted (see previous section, and Chapter 4, Section 4.2 for an explanation). Only tissue stresses are reported (median and quartiles 1 & 3 [Q1–Q3]), as fibrous tissue is expected to fail before calcifications do (ruptures are observed in the tissue, not in the calcifications).

Like for the plaque measurements in Chapter 3, results are non-normally distributed (skewed box plots). The Kruskall-Wallis H test is thus appropriate here too. Significant differences in measurement data between fiber pattern patterns ($P < 0.05$) are indicated with asterisks in the plots. Outliers (data points outside the 1.5 × interquartile range) are indicated with plus signs. The location where these peak values are attained might be important for the vulnerability (likelihood of mechanical failure) or stability of the plaque, and are thus reported as well. These locations are visualized as scatter plots of each stress/strain metric against the normalized path distances, ranging from 0 (center of calcification, luminal side) to 1 (abluminal center, see Figure 4.7 in Chapter 4).

5.2.1. Peak values

Deviatoric maximum principal stress S_{MaxPrin}

The overall median [Q1–Q3] peak value for the maximum principal stress is 91.8 kPa [5.3–261.2]. The Attached pattern has the largest peak values for this stress metric (276.8 kPa [156.1–542.6]), which are significantly higher than the peak values of the other three fiber patterns (see Figure 5.5a). It also has large outliers, as high as 2650.2 kPa. The Pushed Aside pattern has significantly higher peak values (85.2 kPa [41.3–165.3]) than the Encircling or Random pattern, which have median peak values close to zero: 4.5 kPa [2.1–20.9] and 2.4 kPa [1.0–5.1] respectively.

Deviatoric stress along fibers S_{11}

The results of this stress metric are almost the same as for the maximum principal stress, with the same significant differences, but slightly lower values (see Figure 5.5b). This indicates that the maximum principal stress is predominantly composed of stress along fibers, and in the same direction. The overall median peak value is 86.8 kPa [4.6–260.5]. The median peak value for the Attached pattern is 274.4 kPa [155.3–535.2], and for the Pushed Aside pattern 85.1 kPa [41.3–164.0]. The medians for the Encircling and Random patterns are again close to zero: 3.0 kPa [1.5–20.5] and 2.2 kPa [0.5–4.6] respectively.

Deviatoric stress across fibers S_{22}

The peak stresses across fibers are in general much lower compared to maximum principal stress and stress along fibers, with a median peak value for all fiber patterns combined of 3.6 kPa [0.7–13.8]. The Attached and Pushed Aside patterns have both significantly higher peak values for stress across fibers than the Encircling and Random patterns (see Figure 5.5c). The Pushed Aside pattern show higher peak values (21.3 kPa [7.9–33.1]) than the Attached pattern (7.7 kPa [3.7–15.8]), although this difference is not significant. The peak values for the Encircling and Random patterns are again close to zero: 0.4 kPa [0.2–0.9] and 0.3 kPa [0.0–1.6] respectively.

Shear stress between fibers S_{12}

Shear stresses are in general lower than the stresses along fibers, but higher than the stresses across fibers. In overall, the median for peak values is 10.8 kPa [2.2–39.3]. The largest values are for the Attached pattern, with a median peak value of 45.2 kPa [20.8–93.1] and outliers up to 689.5 kPa (see Figure 5.5d). These values are significantly higher than those of the other three fiber patterns, the Pushed Aside pattern: 4.8 kPa [2.7–16.0], Encircling pattern: 1.5 kPa [0.4–4.7] and Random pattern: 1.6 kPa [0.7–4.0].

Von Mises stress S_{Mises}

The Von Mises stress shows the same trends as the maximum principal stress and the stress along fibers, but the peak values are higher: the median peak value for the four fiber patterns combined is 137.7 kPa [9.0–391.8]. The median peak value for the Attached pattern is 415.2 kPa [234.2–813.9], with the outliers as high as 3975.5 kPa (see Figure 5.5e). The median peak value for the Pushed Aside pattern is 127.8 kPa [61.9–248.2], for the Encircling pattern 7.6 kPa [3.6–31.4], and for the Random pattern 4.1 kPa [1.7–8.7].

Maximum principal strain $E_{MaxPrin}$

The median peak value for maximum principal strain is 0.034 [0.010–0.079]. For this strain metric the Pushed Aside pattern (0.024 [0.010–0.037]), Encircling pattern (0.007 [0.002–0.018]) and Random pattern (0.010 [0.004:0.020]) are not significantly different from each other, while the Attached pattern is significantly higher than these three: 0.090 [0.056–0.129] (see Figure 5.5f).

Strain along fibers E_{11}

Strains along fibers are smaller than the maximum principal strains, with an overall median peak value of 0.003 [< 0.001–0.008]. The median peak value for the Encircling pattern (< 0.001 [< 0.001–< 0.001]) is significantly lower than for the other three fiber patterns (Attached pattern: 0.006 [0.004–0.010, Pushed Aside pattern: 0.002 [0.001–0.004], and Random pattern: 0.009 [0.002–0.018]), see Figure 5.5g. The Attached pattern also has significant higher peak values than the Pushed Aside pattern.

Strain across fibers E_{22}

The overall median peak value for the strain across fibers is 0.009 [0.001–0.033]. The peak values for the Attached pattern (0.031 [0.014–0.054]) and Pushed Aside pattern (0.017 [0.006–0.030]) are significantly higher than those of the Encircling pattern (< 0.001 [< 0.001–0.001]) and the Random pattern (0.002 [< 0.001–0.006]), see Figure 5.5h.

Shear strain between fibers E_{12}

The peak values for the shear strain between fibers show the same characteristics as the peaks for the maximum principle strain, but with lower values; approximately half of the values for maximum principal strain. The overall median value for the peak shear strains is 0.065 [0.017–0.150]. The median peak value for the Pushed Aside pattern (0.031 [0.020–0.067]), Encircling pattern (0.013 [0.004–0.037]) and the Random pattern (0.014 [0.006–0.033]) are close together (see Figure 5.5i). The peak values for the Attached pattern are significantly higher (0.180 [0.112–0.257]).

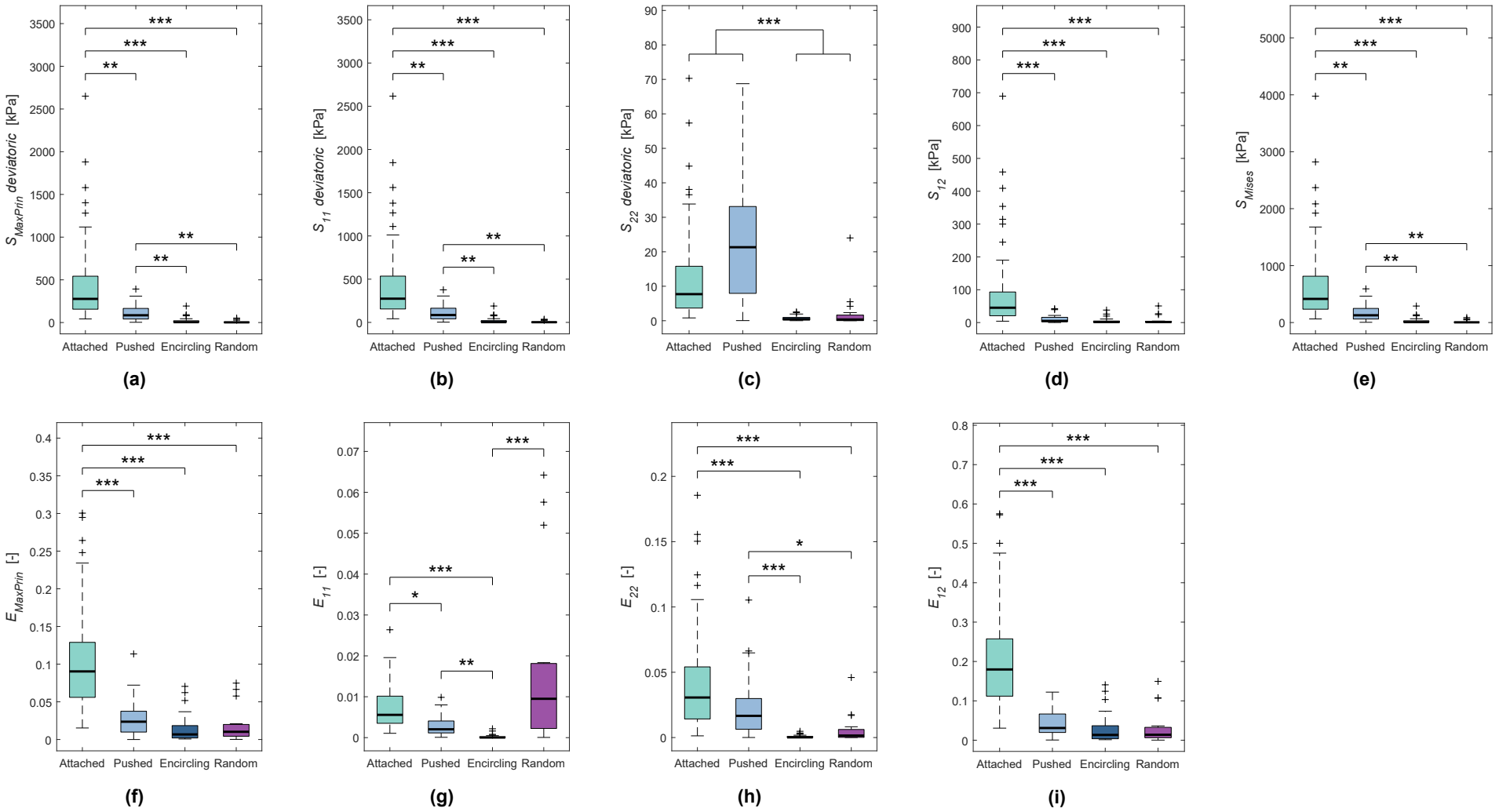

Figure 5.5: Peak values for each stress and strain metric. (a) Maximum principal stress, (b) stress along fibers, (c) stress across fibers, (d) shear stress between fibers, (e) Von Mises stress, (f) Maximum principal strain, (g) strain across fibers, (h) strain across fibers, (i) shear strain between fibers. * Signifies $P < 0.05$, ** signifies $P < 0.005$ and *** signifies $P < 0.0005$.

5.2.2. Peak Locations

In overall, most peak values of the nine stress and strain metrics are attained at a normalized path distance of ~0.5 (see Figures 5.6a-5.6i). This location is at the circumferential tip of the calcification (see Figure 4.7 in Chapter 4). For low stress and strain peak values the locations show variation between 0 and 1, but for the shear stress (S_{12}) and strain (E_{12}), and strain across fibers (E_{22}) there is a preference for path locations < 0.5 observable (see Figures 5.6d, 5.6i & 5.6h). This corresponds with the lumen side of the calcification.

Attached pattern

It can be observed that the peak values at a path length of ~0.5 are mostly from the Attached pattern (except for strain along fibers, see Figure 5.6g), which in general has the largest peak values for all stress and strain metrics. Also the lower peak values of the Attached pattern are close to 0.5, while the peak values for the other fiber patterns spread out along the path at these low levels, see for example Figure 5.6i. Only for low values of stress and strain across fibers (S_{22} & E_{22}) this fiber pattern has peak path locations different than 0.5 (see Figure 5.6c & 5.6h).

Pushed Aside pattern

This fiber pattern has its peak path locations, like the Attached pattern, close to the normalized path length of 0.5, also for lower values of the peak stresses and strains. However, for lower values of the maximum principal strain and shear strain there are also path locations between 0 and 0.5 (see Figure 5.6f & 5.6i).

Encircling pattern

The peak path locations for this fiber pattern show large variability in grouping: for maximum principal stress ($S_{MaxPrin}$) and strain ($E_{MaxPrin}$), stress along fibers (S_{11}) and Von Mises stress (S_{Mises}) the peak path location shifts toward 0.5 for larger metric values (Figure 5.6a, 5.6f, 5.6b & 5.6e), but this is not the case for the other metrics. However, the peak values of these metrics are all close to zero (Figure 5.6c, 5.6d, 5.6g, 5.6h & 5.6i). For the shear stress and strain between fibers (S_{12}, E_{12}) there is a preference for the peak value to be at a normalized path length of ~0.2, at the calcification side close to the lumen (see Figure 5.6i).

Random pattern

This fiber pattern also has its peak values close to zero for many stress/strain metrics, and thus peak value locations spread out along the normalized path. However, the larger peak values attained for the stress/strain metrics were at the tip of the calcification (normalized path of 0.5, see for example Figure 5.6c or 5.6f). For strain along fibers (E_{11}) the peak value locations show different behaviour than the other fiber patterns, with peak path locations deviating from 0.5 where the other fiber patterns are at 0.5. But for this random pattern the 1 and 2 directions are the circumferential and radial directions, and not defined as along and across fibers.

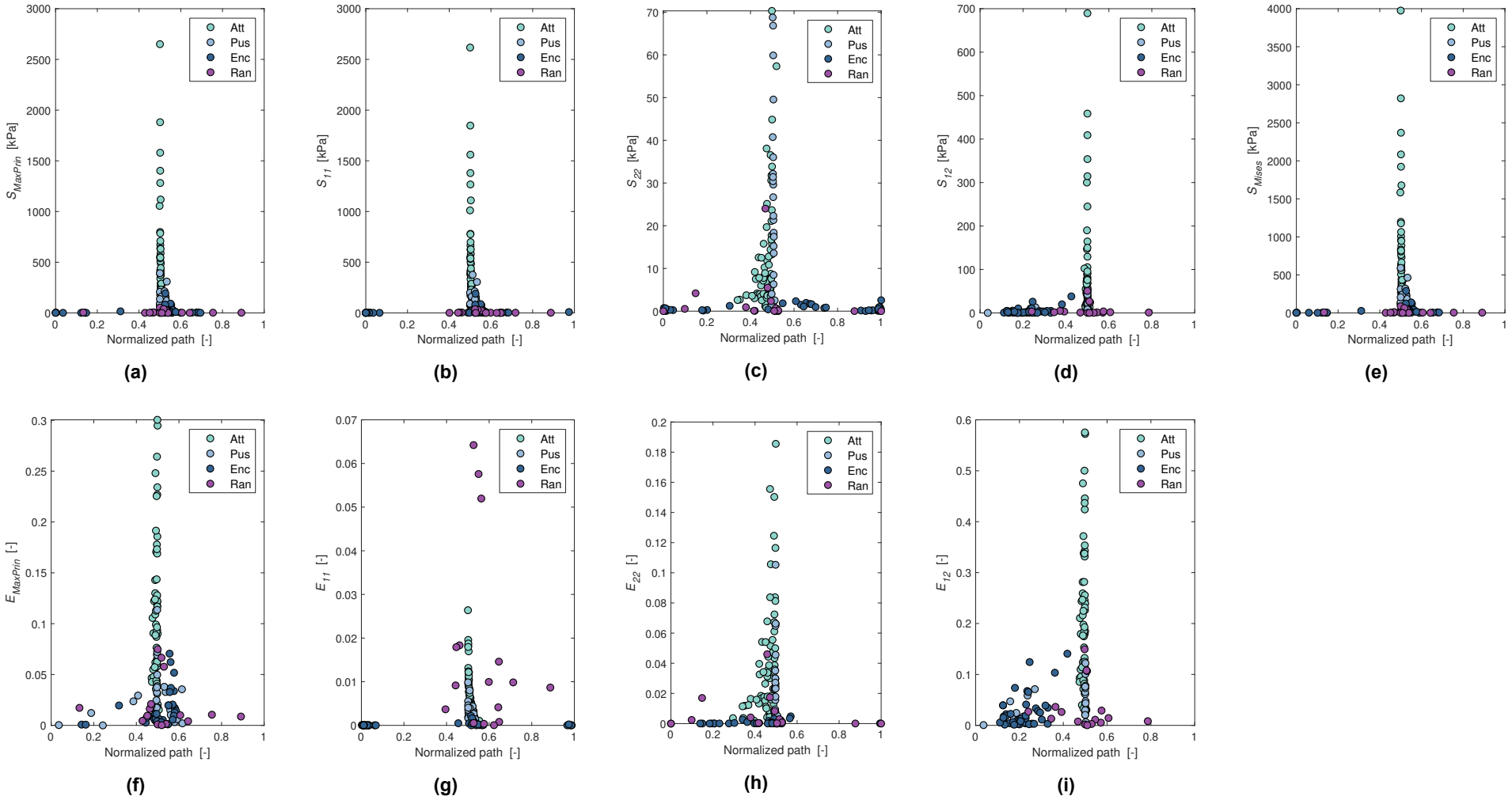

Figure 5.6: Path locations for each peak stress and strain metric. (a) Maximum principal stress, (b) stress along fibers, (c) stress across fibers, (d) shear stress between fibers, (e) Von Mises stress, (f) Maximum principal strain, (g) strain across fibers, (h) strain across fibers, (i) shear strain between fibers. Att is Attached pattern, Pus is Pushed Aside pattern, Enc is Encircling pattern, and Ran is Random pattern.

5.3. Correlations Between Stress and Strain Metrics

Some stress and strain metrics from the previous section showed the same trends, for example maximum principal stress, stress across fibers and Von Mises stress (Figure 5.5a, 5.5b & 5.5e), or maximum principal strain and shear strain (Figure 5.5f & 5.5i). It might be therefore well possible that these stresses and strains show the same response to variations in the three geometric parameters D_{norm}, W_{norm} & A_{calc}. Thus, before performing the multiple regression analysis, a correlation test is done to see which stress and strain metrics show the same trends. Correlation tests were done between the peak values of each stress and strain metric. If two stress or strain metrics are highly correlated to each other, their response to the three geometric parameters, and thus the multiple regression, will be the same. Correlations are calculated using the Pearson correlation test, as explained in Chapter 4, Section 4.2.

Attached pattern

The correlations between all the stress and strain metrics for the Attached pattern are shown in Table 5.1. It can be observed that many of the metrics are strongly positively correlated, meaning that most of the metrics show the same behaviour for changing values of the three driving parameters. All values for r_p are > 0.85, except for one stress metric: the stress across fibers (S_{22}). This metric has all of its correlation coefficients r_p < 0.770, meaning that this metric can have a different response to the three driving parameters than the other metrics. These lower correlations are highlighted in bold in Table 5.1. It is noteworthy that this also means that there is no strong correlation between stress across fibers and strain across fibers (r_p = 0.668, P < 0.05), which might be caused by the anisotropy of the material.

Table 5.1: Pearson correlation for all stress and strain metrics, for the Attached pattern.

		Correlations (r_p)								
		1	*2*	*3*	*4*	*5*	*6*	*7*	*8*	*9*
1	S_{Mises}	1								
2	$S_{MaxPrin}$	1.000	1							
3	S_{11}	1.000	1.000	1						
4	S_{22}	**0.746**	**0.748**	**0.746**	1					
5	S_{12}	0.985	0.985	0.984	**0.769**	1				
6	$E_{MaxPrin}$	0.902	0.901	0.900	**0.679**	0.875	1			
7	E_{11}	0.945	0.945	0.946	**0.758**	0.904	0.937	1		
8	E_{22}	0.909	0.908	0.906	**0.668**	0.901	0.952	0.885	1	
9	E_{12}	0.898	0.897	0.896	**0.670**	0.869	0.999	0.934	0.952	1

All correlations are significant at the 0.05 level.

Pushed Aside pattern

Correlations for the Pushed Aside pattern are shown in Table 5.2. The correlations between stress and strain metrics for this fiber pattern are very similar to the correlations calculated for the Attached pattern, with high positive correlations r_p > 0.850 for all metrics, except stress across fibers (S_{22}). This stress metric again shows correlations which are clearly lower than all other correlations, with r_p values < 0.660. Again, a low correlation between stress and strain in the 2 direction is observable: r_p = 0.430, P < 0.05. The lower correlations are highlighted in bold in Table 5.2.

Encircling pattern

Values for r_p for the Encircling pattern are shown in Table 5.3. Results for this fiber pattern are different from the correlations for the Attached and Pushed Aside pattern; it again shows strong correlations for

Table 5.2: Pearson correlation for all stress and strain metrics, for the Pushed Aside pattern.

		Correlations (r_p)								
		1	*2*	*3*	*4*	*5*	*6*	*7*	*8*	*9*
1	S_{Mises}	1								
2	$S_{MaxPrin}$	1.000	1							
3	S_{11}	1.000	1.000	1						
4	S_{22}	**0.634**	**0.635**	**0.641**	1					
5	S_{12}	0.961	0.961	0.962	**0.534**	1				
6	$E_{MaxPrin}$	0.946	0.946	0.942	**0.500**	0.921	1			
7	E_{11}	0.981	0.981	0.980	**0.559**	0.956	0.960	1		
8	E_{22}	0.919	0.919	0.913	**0.430**	0.904	0.988	0.949	1	
9	E_{12}	0.945	0.946	0.950	**0.654**	0.945	0.900	0.930	0.857	1

All correlations are significant at the 0.05 level.

stress and strain metrics except S_{22} (r_p values < 0.580), but also lower values for strain along fibers (E_{11}). While S_{22} has no strong correlation with E_{22} (r_p = 406, P < 0.05), there still is a strong correlation between S_{11} and E_{11} (r_p = 0.846, P < 0.05). The weaker correlations are highlighted in bold in Table 5.3.

Table 5.3: Pearson correlation for all stress and strain metrics, for the Encircling pattern.

		Correlations (r_p)								
		1	*2*	*3*	*4*	*5*	*6*	*7*	*8*	*9*
1	S_{Mises}	1								
2	$S_{MaxPrin}$	1.000	1							
3	S_{11}	0.999	0.999	1						
4	S_{22}	**0.362**	**0.358**	**0.354**	1					
5	S_{12}	0.959	0.959	0.952	**0.221***	1				
6	$E_{MaxPrin}$	0.901	0.900	0.890	**0.303***	0.965	1			
7	E_{11}	0.836	0.836	0.846	**0.578**	**0.660**	**0.586**	1		
8	E_{22}	0.969	0.968	0.964	**0.406**	0.951	0.941	**0.766**	1	
9	E_{12}	0.900	0.900	0.889	**0.302***	0.965	1.000	**0.586**	0.940	1

All correlations are significant at the 0.05 level, except for values marked with *.

Random pattern

The correlations for the Random pattern are more complicated than for the other fiber patterns. For this fiber pattern the 1 and 2 directions are not along and across the fibers, but are the circumferential and radial directions. There is no material anisotropy in this case, and these directions are thus not linked to this property like in the other three fiber patterns. It can be observed from Table 5.4 that there are weaker correlations between S_{22} and some other metrics: S_{22} & S_{11} (r_p = 0.661, P < 0.05), S_{22} & $E_{MaxPrin}$ (r_p = 0.738, P < 0.05) and S_{22} & E_{11} (r_p = 0.628, P < 0.05). There are also weaker correlations between E_{22} and some other metrics: E_{22} & S_{11} (r_p = 0.690, P < 0.05), E_{22} & $E_{MaxPrin}$ (r_p = 0.783, P < 0.05), and E_{22} & E_{11} (r_p = 0.661, P < 0.05). However, E_{22} is still highly correlated to S_{Mises}, $S_{MaxPrin}$ & S_{11}. The lower correlations are highlighted in bold in Table 5.4.

Table 5.4: Pearson correlation for all stress and strain metrics, for the Random pattern.

		Correlations (r_p)								
		1	*2*	*3*	*4*	*5*	*6*	*7*	*8*	*9*
1	S_{Mises}	1								
2	$S_{MaxPrin}$	1.000	1							
3	S_{11}	0.971	0.971	1						
4	S_{22}	0.821	0.822	**0.661**	1					
5	S_{12}	0.988	0.988	0.924	0.894	1				
6	$E_{MaxPrin}$	0.976	0.975	0.974	**0.738**	0.949	1			
7	E_{11}	0.948	0.947	0.983	**0.628**	0.903	0.982	1		
8	E_{22}	0.835	0.835	**0.690**	0.975	0.894	**0.783**	**0.661**	1	
9	E_{12}	0.983	0.983	0.957	0.801	0.973	0.992	0.961	0.836	1

All correlations are significant at the 0.05 level.

5.4. Impact of Calcification Geometry on Interface Biomechanics

Interface stresses/strains does not only depend on the fiber pattern, but also the morphometric properties of the calcifications within each fiber pattern category. Regression models are constructed in this section, to investigate how the stress and strain outcomes can be predicted by the three main calcification geometric features: normalized distance D_{norm}, normalized width W_{norm} and aspect ratio A_{calc}.

These regression models are equations, where the response variable (outcome) is a stress or strain metric, and the predictor variables are the three geometric parameters. Predictive terms are included if their coefficient is significantly different from zero ($P < 0.05$) in the t-test. This is done by first calculating the coefficient estimates and corresponding P-values of all terms, and removing the terms having a $P > 0.05$. First, the z-score (subtracting the mean and dividing by the standard deviation afterwards) is calculated for all parameter values. The parameter values are standardized this way, and coefficients in the regression equation can be directly compared to each other. The goodness of fit of the final regression model compared to a model without predictive terms (constant term only) is calculated with the F-test. Then, a modified R^2 value is reported, which is adjusted for the number of predictor terms added to the model. The regular R^2 value still *increases* if non-significant predictors are added to the model, but the modified R^2 value will *decrease* if the model becomes over determined, and is always lower than the regular R^2 value.

5.4.1. Multiple Regressions Per Fiber Pattern

The previous section showed that stress and strain metrics might show similar trends. For all four fiber patterns the stress across fibers (S_{22}) was different from all other metrics, while the rest strongly correlated to each other. For the Encircling pattern the strain along fibers (E_{11}) is also different. This means that for the Attached pattern, Pushed Aside pattern and Random pattern it is only necessary to create two multiple regression models: S_{22} and one of the other metrics. For ease of interpretation, stress along fibers (S_{11}) is chosen for this. For the Encircling pattern three regression models will be constructed; one for S_{11}, one for S_{22}, and one for E_{11}.

1) Attached pattern

Stress along fibers S_{11} Two response variables are determined for the Attached pattern: stress along fibers S_{11} and across fibers S_{22}. Results of the regression for stress along fibers indicate that the final model explains 87% (adjusted R^2 of 0.87) of the variance in the data and that the model is a significant predictor of the stress along fibers, $P < 0.0005$ (of the F-test), meaning that the calcification

geometric parameters indeed are predictors of this stress metric. The terms that significantly add to the regression model are summarized in Table 5.5, showing the coefficient estimates, their 95% confidence intervals, and their P values from the t-test.

Table 5.5: Coefficient estimates for the regression model of S_{11}, for the Attached pattern.

	Estimate	*95% CI*	*P value*
$Intercept$	601	[542, 661]	< 0.0005
D_{norm}	-81	[-123, -38]	< 0.0005
W_{norm}	383	[306, 460]	< 0.0005
A_{calc}	722	[637, 809]	< 0.0005
$W_{norm} : A_{calc}$	396	[298, 494]	<0.0005

Normalized distance D_{norm} has a small negative coefficient, this means that stress along fibers increases as the calcification is closer to the lumen. A possible explanation is that close to the lumen the tissue deformations are larger. Positive coefficients are found for both normalized width W_{norm} (coefficient of 383) and aspect ratio A_{calc} (coefficient of 722), indicating that stress along fibers increases for increasing values of normalized width and aspect ratio of a calcification. The coefficient of the aspect ratio is approximately twice as large as the coefficient of the normalized width, indicating that its unique effect is also twice as large.

It is possible that the effect of one variable on the stress/strain outcome depends on the value of another variable, this is called an interaction effect in regression analysis. If interactions are present, the goodness of fit (R^2 value) of the regression equation will significantly improve if interaction terms are included. $W_{norm} : A_{calc}$ is an interaction between normalized width and aspect ratio. These parameters thus have not only direct effects on the stress, but the total effect of aspect ratio also depends on the value of normalized width and vice versa. This effect is visualized in Figure 5.7, where it can be appreciated that for increasing values of normalized width the effect of aspect ratio on stress increases. The parameters were standardized by taking the z-score, parameter ranges in this plot and the ones to follow show these standardized values. The final regression equation for stress along fibers for the Attached pattern is as follows:

$$S_{11} = 601 - 81D_{norm} + 383W_{norm} + 723A_{calc} + 396W_{norm}A_{calc}. \tag{5.1}$$

Equation 5.1 (and following equations) is based on standardized values of the three parameters; coefficients for original parameter values will be different.

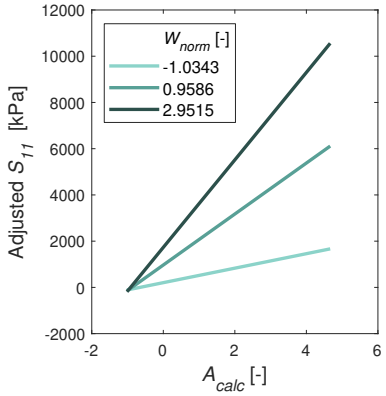

Figure 5.7: Interaction between normalized width W_{norm} and aspect ratio A_{calc} for the regression of stress S_{11}, for the Attached pattern.

Stress across fibers S_{22} Stress across fibers S_{22} is also predicted by the three parameters (P < 0.0005), but less variance can be explained by the model this time (adjusted R^2 of 0.65). The terms that significantly add to the model are summarized in Table 5.6, along with the 95% confidence intervals.

Table 5.6: Coefficient estimates for the regression model of S_{22}, for the Attached pattern.

	Estimate	*95% CI*	*P value*
$Intercept$	17	[14, 20]	< 0.0005
W_{norm}	8	[12, 21]	< 0.0005
A_{calc}	16	[4, 12]	< 0.0005
$D_{norm} : W_{norm}$	6	[3, 9]	< 0.0005
$W_{norm} : A_{calc}$	9	[4, 14]	<0.0005

Again, the aspect ratio has a coefficient twice as large as normalized width. Distance to the lumen is not a significant direct predictor of S_{22}. Its influence is only indirect; through the positive effect of normalized width, with a coefficient of six, the smallest coefficient in this regression. The interaction between these two parameters is visualized in Figure 5.8a, where it can be observed that the effect of normalized width on S_{22} increases as the normalized distance increases. Aspect ratio and normalized width have the same interaction as in the regression of S_{11} (see Figure 5.8b). The coefficients for each term in this regression are lower than the coefficients for the regression for stress along fibers, because the stresses across fibers are in general lower than stresses across fibers. The final regression equation for stress across fibers for the Attached pattern is:

$$S_{22} = 17 + 8W_{norm} + 16A_{calc} + 6D_{norm}W_{norm} + 9W_{norm}A_{calc}. \tag{5.2}$$

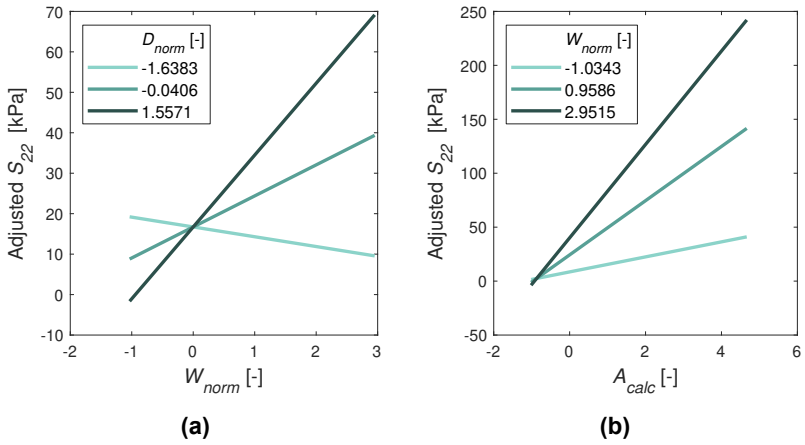

Figure 5.8: Interaction between normalized distance D_{norm} and normalized width W_{norm} (a), and interaction between normalized width W_{norm} and aspect ratio A_{calc} (b) for the regression of stress S_{22}, for the Attached pattern.

2) Pushed Aside pattern

Stress along fibers S_{11} Stress along fibers S_{11} is predicted by the calcification geometric features (P < 0.0005), and 91% of the variance can be explained by the final regression model (adjusted R^2 = 0.91), indicating a good fit of the model to the measured stresses. The terms that add significantly to the regression model are listed in Table 5.7.

The regression for this stress metric shows that the normalized distance has a negative effect (coefficient of -51) on the stress along fibers (like for the Attached pattern), meaning that the closer the

Table 5.7: Coefficient estimates for the regression model of S_{11}, for the Pushed Aside pattern.

	Estimate	*95% CI*	*P value*
$Intercept$	133	[120, 146]	< 0.0005
D_{norm}	-51	[-64, -38]	< 0.0005
W_{norm}	95	[76, 114]	< 0.0005
A_{calc}	61	[46, 77]	< 0.0005
$D_{norm} : A_{calc}$	-20	[-34, -6]	0.008
$W_{norm} : A_{calc}$	60	[43, 77]	<0.0005

calcification is to the lumen, the higher this stress. Normalized width and aspect ratio again have a positive direct effect on the stress, but unlike for the Attached pattern, the direct contribution of normalized width has a larger coefficient (coefficient of 95) than the direct contribution of aspect ratio (coefficient of 61).

The total contribution of aspect ratio also depends on the values of normalized distance and normalized width, and vice versa. The interaction between aspect ratio and normalized distance has a negative coefficient (-20), this effect is visualized in Figure 5.9a; for larger values of normalized distance (thus further away from the lumen) the positive effect of aspect ratio on stress decreases. The interaction between aspect ratio and normalized width is positive (coefficient of 60), meaning that for larger values of normalized width the positive effect of the aspect ratio increases (see Figure 5.9b). For low values of normalized width the aspect ratio almost has no influence on the stress. The final regression equation for stress along fibers for the Pushed Aside pattern is as follows:

$$S_{11} = 133 - 51D_{norm} + 95W_{norm} + 61A_{calc} - 20D_{norm}A_{calc} + 60W_{norm}A_{calc}. \tag{5.3}$$

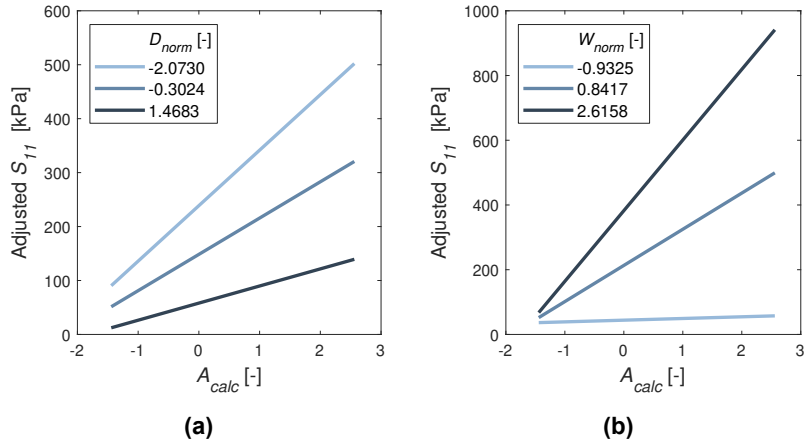

Figure 5.9: Interaction between normalized distance D_{norm} and aspect ratio A_{calc} (a), and interaction between normalized width W_{norm} and aspect ratio A_{calc} (b) for the regression of stress S_{11}, for the Pushed Aside pattern.

Stress across fibers S_{22} Stress across fibers for the Pushed Aside pattern is also significantly predicted by the driving parameters (P = 0.002). This time, 42% of the variance can be explained by the model (adjusted R^2 = 0.42). The parameters that significantly add to the model can be found in Table 5.8.

Like for the Attached pattern, normalized width and aspect ratio have direct positive effects on the stress across fibers, while normalized distance has no direct effect. Again, its effect is indirect, via the

Table 5.8: Coefficient estimates for the regression model of S_{22}, for the Pushed Aside pattern.

	Estimate	*95% CI*	*P value*
$Intercept$	28	[21, 34]	< 0.0005
W_{norm}	11	[4, 18]	0.034
A_{calc}	8	[1, 15]	0.006
$D_{norm} : W_{norm}$	15	[5, 25]	0.007

interaction with normalized width (coefficient of 15), where for small values of normalized distance the effect of normalized width is negative, and for large values of normalized distance the effect of normalized width is positive (see Figure 5.10). This time, aspect ratio has no indirect effect with normalized width, and its direct effect is smaller (coefficient of 8) than that of normalized width (coefficient of 11). The coefficients for this fiber pattern are in general smaller than the coefficients of the stress along fibers regression, as these stresses are lower. The final regression equation for stress across fibers for the Pushed Aside pattern is as follows:

$$S_{22} = 28 + 11W_{norm} + 8A_{calc} + 15D_{norm}W_{norm}. \tag{5.4}$$

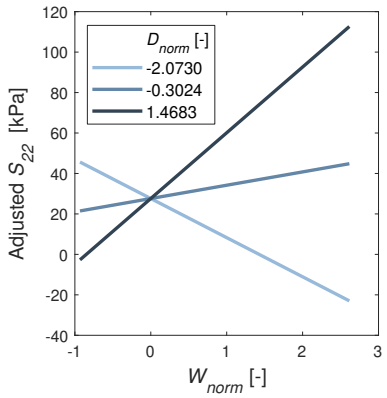

Figure 5.10: Interaction between normalized distance D_{norm} and normalized width W_{norm} for the regression of stress S_{22}, for the Pushed Aside pattern.

Encircling pattern

Stress along fibers S_{11} The final regression for stress along fibers S_{11} for the Encircling pattern significantly predicted the stress (P < 0.0005), and has a good fit where 93% of the variance can be explained by the model (adjusted $R^2 = 0.93$). The terms that significantly add to this prediction are listed in Table 5.9.

All parameters and their interactions are included in this regression. Normalized distance has a negative direct effect (coefficient of -5), and interacts with both aspect ratio and normalized width. Normalized width and aspect ratio both have positive direct effects, and aspect ratio has a larger direct effect (coefficient of 26) than normalized width (coefficient of 18). Aspect ratio also has an indirect effect on the stress via a negative interaction (coefficient of -8) with normalized distance (see Figure 5.11a) and via a positive interaction (coefficient of 13) with normalized width (see Figure 5.11b). Normalized width has a indirect negative effect (coefficient of -8) via an interaction with normalized distance (see Figure 5.11c).

Table 5.9: Coefficient estimates for the regression model of S_{11}, for the Encircling pattern.

	Estimate	*95% CI*	*P value*
$Intercept$	19	[15, 22]	< 0.0005
D_{norm}	-5	[-9, -2]	0.003
W_{norm}	18	[15, 22]	< 0.0005
A_{calc}	26	[23, 30]	< 0.0005
$D_{norm} : A_{calc}$	-8	[-11, -5]	0.008
$W_{norm} : A_{calc}$	13	[9, 17]	<0.0005
$D_{norm} : W_{norm}$	-8	[-13, -4]	0.001

In overall, the coefficients for this stress are lower than the coefficients for the Attached and the Pushed Aside pattern, indicating that the stress along fibers for this fiber pattern is in general lower compared to the Attached and Pushed Aside patterns. This is also observable in Figure 5.5b in Section 5.2. The final regression equation for stress along fibers for the Encircling pattern is as follows:

$$S_{11} = 19 - 5D_{norm} + 18W_{norm} + 26A_{calc} - 8D_{norm}A_{calc} + 13W_{norm}A_{calc} - 8D_{norm}W_{norm}. \quad (5.5)$$

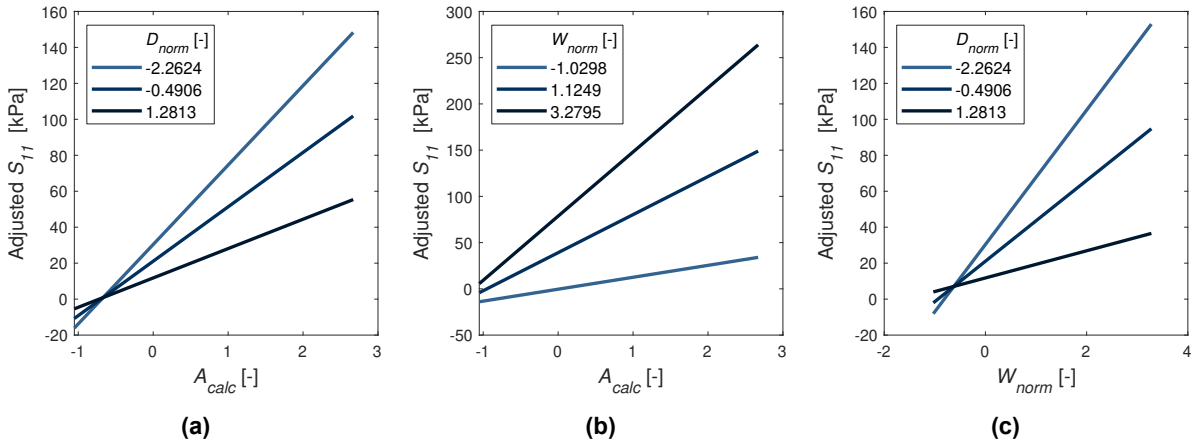

Figure 5.11: Interaction between normalized distance D_{norm} and aspect ratio A_{calc} (a), between normalized width W_{norm} and aspect ratio A_{calc} (b), and between normalized distance D_{norm} and normalized width W_{norm} for the regression of stress S_{11}, for the Encircling pattern.

Stress across fibers S_{22} Regression of the stress across fibers for this fiber pattern is also significant (P < 0.0005), and 80% of the variance can be explained by the final model (R^2 = 0.80). The terms that significantly add to the final model are listed in Table 5.10.

All parameters and their interactions are included in the regression model. Normalized distance has a negative direct effect (coefficient of -0.31). Normalized width has a negative direct effect on stress; its coefficient is -0.16. Aspect ratio has a relatively large positive direct effect, with a coefficient of 0.40. The indirect effect of aspect ratio is positive if it interacts with normalized distance (coefficient of 0.18, see Figure 5.12a) and negative if it interacts with normalized width (coefficient of -0.17, see Figure 5.12b). The interaction between normalized width and normalized distance has a positive effect on stress, with a coefficient of 0.27 (see Figure 5.12c). The small coefficient values for this regression reflect the small values for this stress metric. The final regression equation for stress across fibers for the Encircling pattern is as follows:

Table 5.10: Coefficient estimates for the regression model of S_{22}, for the Encircling pattern.

	Estimate	*95% CI*	*P value*
$Intercept$	0.73	[0.63, 0.83]	< 0.0005
D_{norm}	-0.31	[-0.41, -0.20]	< 0.0005
W_{norm}	-0.16	[-0.28, -0.04]	0.008
A_{calc}	0.40	[0.30, 0.50]	< 0.0005
$D_{norm} : A_{calc}$	0.18	[0.09, 0.28]	< 0.0005
$W_{norm} : A_{calc}$	-0.17	[-0.30, -0.03]	0.015
$D_{norm} : W_{norm}$	0.27	[0.12, 0.41]	0.001

$$S_{22} = 0.73 - 0.31D_{norm} - 0.16W_{norm} + 0.40A_{calc} + 0.18D_{norm}A_{calc} - 0.17W_{norm}A_{calc} + 0.27D_{norm}W_{norm}. \quad (5.6)$$

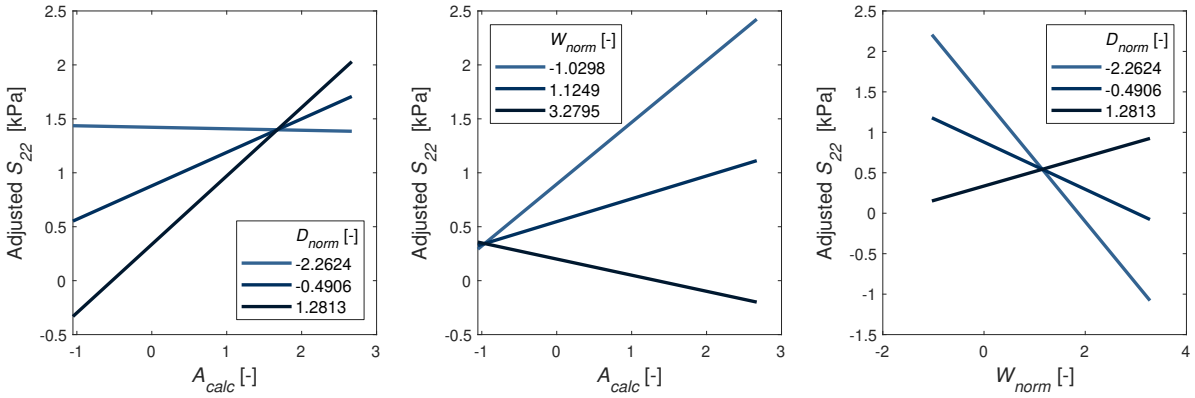

Figure 5.12: Interaction between normalized distance D_{norm} and aspect ratio A_{calc} (a), between normalized width W_{norm} and aspect ratio A_{calc} (b), and between normalized distance D_{norm} and normalized width W_{norm} for the regression of stress S_{22}, for the Encircling pattern.

Strain along fibers $\mathbf{E_{11}}$ For this fiber pattern the strain along fibers (E_{11}) is not significantly correlated to other stress or strain metrics, and a separate regression model is generated for this metric. The final model predicted the strain significantly (P < 0.0005) and explains 71% of the variance in the data (adjusted R^2 = 0.71). The terms that significantly add to the prediction are listed in Table 5.11.

Table 5.11: Coefficient estimates for the regression model of E_{11}, for the Encircling pattern.

	Estimate	*95% CI*	*P value*
$Intercept$	0.21E-3	[0.13E-3, 0.28E-3]	< 0.0005
A_{calc}	0.35E-3	[0.27E-3, 0.42E-3]	< 0.0005
$D_{norm} : A_{calc}$	-0.10E-3	[-0.16E-3, -0.03E-3]	0.009

Only two parameters are sufficient to predict the strain along fibers. Only aspect ratio has a direct effect on the strain (coefficient of 0.35E-3), the second parameter is normalized distance, which has an interaction with aspect ratio (coefficient of -0.10E-3). This interaction is visualized in Figure 5.13.

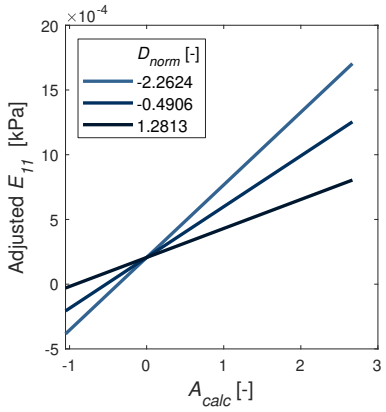

Figure 5.13: Interaction between normalized distance D_{norm} and aspect ratio A_{calc} for the regression of strain E_{11}, for the Encircling pattern.

The final regression equation for strain along fibers for the Encircling pattern is as follows:

$$E_{11} = 0.21 \cdot 10^{-3} + 0.35 \cdot 10^{-3} A_{calc} - 0.10 \cdot 10^{-3} D_{norm} A_{calc}. \tag{5.7}$$

This regression equation has only two predictor variables and one response variable, making it a surface in 3D space which can be graphically represented. The plot of this surface, together with the measured data, is visualized in Figure 5.14.

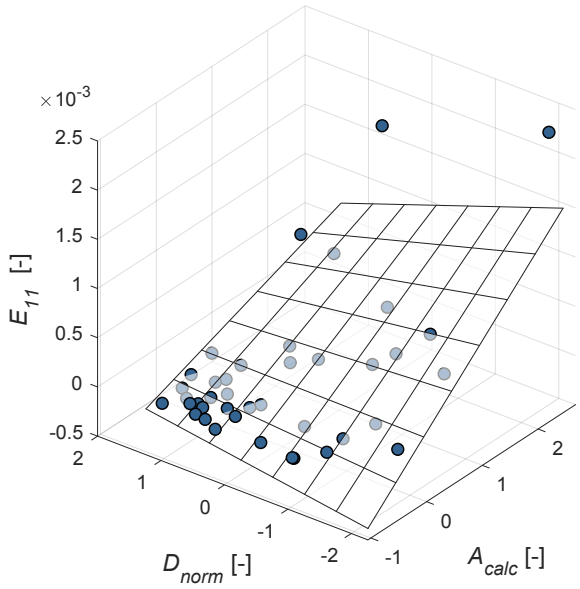

Figure 5.14: The regression equation for strain E_{11} for the Encircling pattern plotted as a surface. The points are the measured data.

Random pattern

Stress along fibers S_{11} The regression model for stress along fibers for the Random pattern predicted the stress significantly (P < 0.0005), and 92% of the variance can be explained by this model (R^2 = 0.92). The terms that significantly add to the model are listed in Table 5.12.

Table 5.12: Coefficient estimates for the regression model of S_{11}, for the Random pattern.

	Estimate	*95% CI*	*P value*
$Intercept$	8	[5, 10]	< 0.0005
W_{norm}	8	[5, 10]	< 0.0005
A_{calc}	7	[5, 9]	< 0.0005
$W_{norm} : A_{calc}$	7	[4, 10]	0.001
$D_{norm} : W_{norm}$	3	[0, 5]	0.037

All three parameters add significantly to the prediction of stress along fibers. Normalized width and aspect ratio are direct predictors, with coefficients of 8 and 7, respectively. These two parameters also have an interaction with each other (coefficient of 7), which is visualized in Figure 5.15a. The third parameter, normalized distance, only has an indirect effect, depending on the value of normalized width (coefficient of 3). This interaction is visualized in Figure 5.15b. The final regression equation for stress along fibers for the Random pattern is as follows:

$$S_{11} = 8 + 8W_{norm} + 7A_{calc} + 7W_{norm}A_{calc} + 3D_{norm}W_{norm}. \tag{5.8}$$

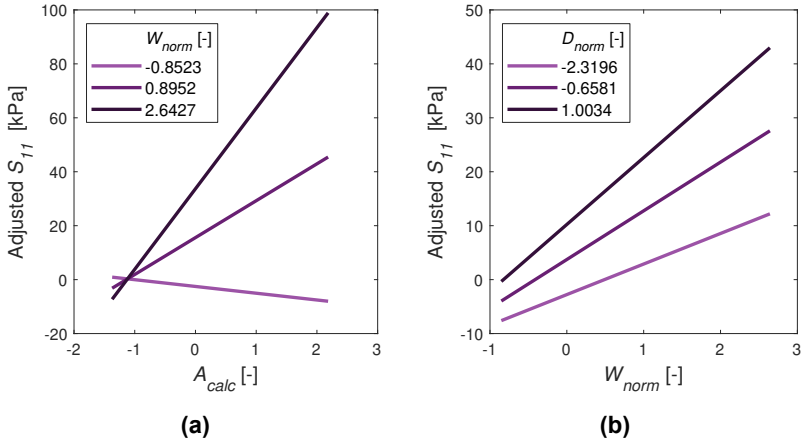

Figure 5.15: Interaction between normalized width W_{norm} and aspect ratio A_{calc} (a), and interaction between normalized distance D_{norm} and normalized width (b) for the regression of stress S_{11}, for the Random pattern.

Stress across fibers S_{22} The regression for stress across fibers for this model is significant (P < 0.0005), and the prediction explains 94% of the variance (adjusted R^2 = 0.94). The terms that add significantly to the prediction are listed in Table 5.13.

Table 5.13: Coefficient estimates for the regression model of S_{22}, for the Random pattern.

	Estimate	*95% CI*	*P value*
D_{norm}	-1.9	[-2.8, -1.0]	< 0.0005
$D_{norm} : W_{norm}$	-3.8	[-4.4, -3.2]	< 0.0005

This stress metric only has the normalized distance as direct predictor (coefficient of -1.9), and the normalized width as indirect predictor, depending on the value of normalized distance (coefficient of

-3.8). See Figure 5.16 for the interaction between these two parameters. The coefficients are in the same range as the coefficients of stress along fibers for this fiber pattern, implying that the magnitude of these two stresses do not differ as much from each other as it does for the Attached and Pushed Aside patterns.

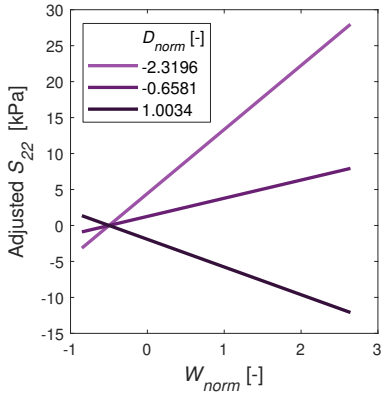

Figure 5.16: Interaction between normalized distance D_{norm} and normalized width W_{norm} for the regression of stress S_{22}, for the Random pattern.

The final regression equation for stress across fibers for the Random pattern is as follows:

$$S_{22} = -1.9D_{norm} - 3.8D_{norm}W_{norm}. \tag{5.9}$$

This regression equation is in 3D space: two predictor variables and one response variable, and can thus be plotted with respect to the measured values. The equation is plotted as a surface in Figure 5.17.

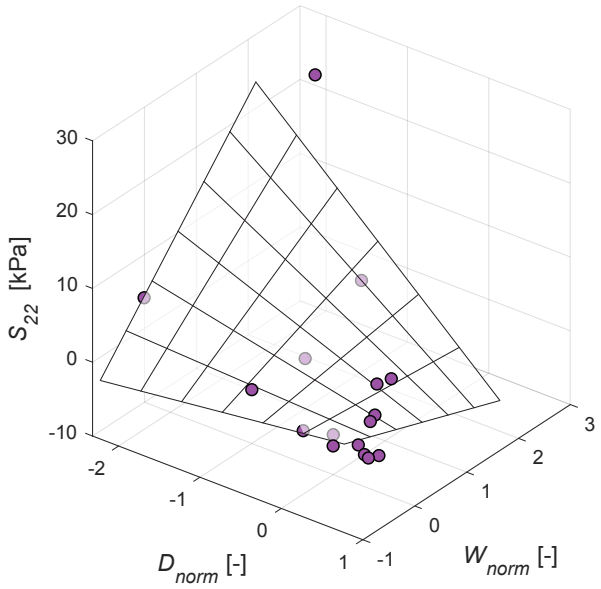

Figure 5.17: The regression equation for stress S_{22} for the Random pattern plotted as a surface. The points are the measured data.

6

Discussion

This study consisted of two distinct parts: the morphometric analysis of plaque tissue, and the biomechanical modeling part based on this analysis. This two-staged structure resulted in two separate results sections (Chapter 3 & Chapter 5). Results of both chapters will be discussed next. First the results of the morphometric analysis will be discussed, followed by a discussion of the modeling results, where a connection will be made with the morphometric results.

6.1. Morphometric Analysis

The morphometric analysis revealed that there are four main fiber alignment patterns present in plaque tissue surrounding calcifications: 1) the Attached pattern, where local fiber alignment is not disrupted or altered by the calcification, 2) the Pushed Aside pattern, where fibers are pushed aside by the calcification in radial direction, 3) the Encircling pattern, where a small band of fibers encircling the calcification is observable and 4) the Random pattern, where the local fiber alignment is random, effectively making it isotropic. See Figure 3.1 in Chapter 3 for an example of each of the four main patterns.

The Attached pattern was found to be the most prevalent pattern (38%), followed by the Encircling pattern (23%), Pushed Aside pattern (15%) and lastly the Random pattern (9%). Combinations of these patterns at the calcification border were also possible, and were found for 15% of the segmented calcifications (see Chapter 3, Figure 3.2). The Random pattern was located at the abluminal, outer region of the plaque mostly, while other patterns were found to be uniformly distributed in the plaque (Chapter 3, Figure 3.4c). A possible explanation for this is that fibers close to the lumen are aligned with the lumen boundary, and are less organized deep in the plaque [70]. Disorganized fibrous structures are therefore not commonly observed close to the lumen.

Calcifications belonging to the Attached pattern showed larger aspect ratios (Chapter 3, Figure 3.5c), and were in general larger than calcifications belonging to the other three patterns (Chapter 3, Figures 3.5a & 3.5b). There were no major correlations found between the measured geometric parameters, but it was found that in general the calcification length L_{calc} increases with its width W_{calc} (Chapter 3, Figure 3.10), indicating a general increase in calcification size as both length and width increases.

The calcification morphology could be described with only three parameters: normalized distance D_{norm}, normalized width W_{norm} and aspect ratio A_{calc}. These parameters were based on the measured geometric features of the calcification (see Chapter 2, Section 2.2.3). Normalized distance D_{norm} described the location of the calcification in the plaque, ranging from zero at the lumen to one at the abluminal side of the plaque, normalized width W_{norm} was the calcification width normalized with respect to the local plaque thickness, also ranging from zero (calcification occupied no plaque width) to one (calcification occupied whole plaque width). Length of the calcification could be obtained by multiplying this width measure with aspect ratio A_{calc}. As previously mentioned, the Attached pattern showed the largest values for calcification size and aspect ratio, and values for W_{norm} and A_{calc} were therefore

also larger for this pattern compared to the other three fiber patterns. The Random pattern was found more abluminally than the other three fiber patterns, and had therefore the largest values for D_{norm}.

The Attached pattern is distinct from the other three patterns; the fiber alignment is not disrupted for this pattern, and fiber structure of fibrous tissue is visible inside the calcifications that belong to this pattern. This indicates that it is the fiber structure itself that is mineralized in this type of calcification. A possible explanation might be that the calcification progression is across the fiber alignment as well, but mainly along the fiber alignment. It is reported that calcification process is directed by fiber alignment [28], this is a possible explanation why calcifications belonging to the Attached pattern show the largest aspect ratios. The calcification structure of the Attached pattern is found to be correlated to bone formation in plaques [29], this pattern is therefore possibly related to the active calcification pathway involving osteoblast-like and osteoclast-like cells, which is present in more advanced stages of atherosclerosis [27, 30]. The endarterectomy samples of this study consist of advanced plaques far in their developmental stage, explaining why the Attached pattern was, consistent with literature [29], the most prevalent pattern.

For the Pushed Aside and Encircling patterns the calcification process is limited to a void or defect between fibers, where for these patterns there is no calcification of the fibers themselves observable. The agglomeration of the calcifying vesicles and apoptotic cells is limited to these voids, explaining the smaller aspect ratios and sizes observed for these patterns. For calcifications belonging to the Random pattern it is not clear what the underlying calcification mechanism is. The randomly aligned fibers themselves might get calcified, or the calcification can develop in a void between the random fibers.

The morphometric analysis was based on carotid endarterectomy samples. As mentioned in the introduction, this surgical procedure is only performed if the plaque is highly stenotic, and thus clinically considered as a high-risk plaque. Only advanced plaques were thus included in this study, but calcifications are only present in advanced stages of plaques, making these endarterectomy samples relevant for this study.

The processing of the samples for histology might induce damage to the cross-sectional slices however, and the more calcified a sample was, the higher the chance of tissue damage, and thus the higher the chance that a cross-section had to be excluded. This possibly introduced a small bias towards the size of the calcifications included. However, large-sized calcifications were still present in the study (see Chapter 3, Figure 3.6).

The Pushed Aside pattern was not easily definable; the exact fiber alignment, their angles with respect to the calcification at each position, was not easily measurable. In the end, a representative alignment, obtained from potential flow was used. This was not exactly the same as the real fiber pattern, but is however used in other biomechanical solutions as well to represent directionality of tissue [82, 83].

6.2. Biomechanical Modeling

The aim of this part of the study was to investigate stress/strain metrics that possibly cause damage in the fibrous tissue. Therefore, only the deviatoric part of the measured interface stresses was regarded in this study. Stress is build of two distinct parts; the hydrostatic pressure and the deviatoric stress. Hydrostatic pressure causes volume change of a body, and the deviatoric stress causes distortion (see Chapter 4, Section 4.1.6). Since the tissue materials in this study were incompressible, the hydrostatic part of the stress tensor does not add to the distortion or damage of the tissue, and was therefore left out of the stress measurements. Shear stress has no hydrostatic part, and the Von Mises stress is already based on the deviatoric part only.

Biomechanical models of the same representative geometry, but different fiber patterns demonstrated that stress along fibers S_{11} was larger than stress across fibers S_{22} and shear stress S_{12}. Fibers are the main load bearing structures in the plaque, and stress showed therefore the largest magnitude along fiber direction. For the specific geometry in this comparison, which was based on measured

parameters, the three stress metrics showed values which were in the same range or larger than stress at the lumen. For example the stress along fibers S_{11} had a maximum value of 293 kPa at the lumen, and interface stresses for the Attached pattern and Pushed Aside pattern had peak values of 373 kPa and 300 kPa respectively (Chapter 5, Figure 5.2). Lower peak stresses were found for the Encircling pattern and Random pattern: 165 kPa and 72 kPa. For stress across fibers S_{22} the Attached pattern and Pushed Aside pattern also showed peak values in the range of the maximum value attained at the lumen, together with the Random pattern (Chapter 5, Figure 5.3). For shear stress S_{12} all four fiber patterns had interface stresses larger than the maximum value attained at the lumen (Chapter 5, Figure 5.4).

This study demonstrated that peak stresses develop at the interface and could reach levels that are in the same range or surpass those at the lumen, a natural high stress region in plaques because of the intraluminal pressure. A possible explanation for these high interface stresses is the stiffness mismatch between the stiff inclusion (calcification) and the soft tissue surrounding it.

For the Random pattern the 1 and 2 directions were defined as circumferential and radial direction respectively, as this pattern had no organized fiber directionality. Values for these stresses were generally lower compared to the other three fiber patterns, except for shear stress, but shearing between fibers cannot be defined by these two directions for this fiber pattern. The low values correspond with lower stresses found in literature for isotropic material properties compared to anisotropic [55, 84]. These studies used orthotropic material properties for their anisotropic materials however, the fibers added in this study further increased this difference. The low interface stresses for isotropic materials is a possible reason why studies were more inclined to investigate lumen stresses (e.g. see [68]) or the effect of calcification on fibrous cap stress (e.g. see [66]). Lumen stress was higher in this study compared to other studies using generic plaque shapes (e.g. see [55, 61]), but again, these studies did not implement the fibers of the fibrous tissue. The only other study using this fiber model showed a significant increase in stress in high stress regions compared to the isotropic case [70].

The FE models for the 145 unique calcifications segmented in the morphometric analysis confirm the findings of the direct comparison. Stresses for the Attached pattern and Pushed Aside pattern were in general significantly larger than stresses for the Encircling pattern and Random pattern (Chapter 5, Figures 5.5a-5.5e). Only for shear stress S_{12} had the Pushed Aside pattern no significantly larger peak stresses (Figure 5.5d). The Attached pattern had the largest peak stresses of all four fiber patterns, also significantly larger than stresses of the Pushed Aside pattern for maximum principal stress $S_{MaxPrin}$ (Figure 5.5a), stress along fibers S_{11} (Figure 5.5b) and Von Mises stress S_{Mises} (Figure 5.5e).

Peak values for stress along fibers S_{11} were significantly larger than peak values for stress across fibers S_{22} and shear stress S_{12}, and approximately as large as peak values for maximum principal stress $S_{MaxPrin}$. Maximum principal stress is calculated from the stress tensor by rotating the local coordinates such that the stress tensor becomes diagonal (consisting of only normal stress components). Because of the large values for S_{11} and the relatively low values for the other components of the deviatoric stress tensor $\mathbf{S}$, the following approximation can be made:

$$\mathbf{S} = \begin{bmatrix} S_{11} & S_{12} & S_{13} \\ S_{21} & S_{22} & S_{23} \\ S_{31} & S_{32} & S_{33} \end{bmatrix} \approx \begin{bmatrix} S_{11} & 0 & 0 \\ 0 & 0 & 0 \\ 0 & 0 & 0 \end{bmatrix}, \tag{6.1}$$

and thus: $S_{MaxPrin} \approx S_{11}$, explaining the similarity between these two stress metrics in this study. Von Mises stress S_{Mises} showed the same trends as S_{11} and $S_{MaxPrin}$, but with higher peak values. This stress metric is calculated from the deviatoric part of the stress tensor: $S_{Mises} = \sqrt{\frac{3}{2}\mathbf{S} : \mathbf{S}}$ (see Chapter 4, Section 4.1.6), and using the same assumption is reduced to: $S_{Mises} = \sqrt{\frac{3}{2}S_{11}^2}$, explaining the same trends, but with larger peak values. The clear relation between maximum principal stress and Von Mises stress in fibrous tissue might explain why there is no consensus in literature on which of these two is most relevant [51]; they only differ in magnitude for the anisotropic fibrous tissue.

For strains too the Attached pattern showed generally the largest values (Chapter 5, Figures 5.5f-5.5i), followed by the Pushed Aside pattern which had significantly larger strains compared to the Encircling pattern and Random pattern for strain along fibers E_{11} (Figure 5.5g) and strain across fibers E_{22} (Figure 5.5h). Strain E_{11} for the Random pattern was large compared to the other fiber patterns, this is because E_{11} is defined as along the stiff fibers in the other three fiber patterns, while for the Random pattern it is strain of a less stiff isotropic material in circumferential direction. Shear strain E_{12} was in general larger than the other strain metrics, and therefore predicted maximum principal strain $E_{MaxPrin}$ (with a factor of two difference in magnitude because ABAQUS reports strain γ_{ij}, with is two times as large as tensorial strain ϵ_{ij}).

All relevant peak stresses and strains were attained at the tip of the calcification; only for small peak values the locations showed variation along the calcification boundary (Chapter 5, Figures 5.6a-5.6i). Reason for these peak values to be at the calcification tip might be the high curvature of the calcification at this location. This curvature is positioned in the circumferential direction of the plaque, the main loading direction in circular structures after a pressure is applied. This also explains why the Attached pattern and Pushed Aside pattern generally showed larger stresses compared to the other two fiber patterns in the comparison: the fiber alignment was closer to the circumferential direction for these patterns than for the Encircling pattern, and the Random pattern had no organized alignment at all.

The implementation of a realistic fiber material model in biomechanical models of calcified plaques revealed peak stresses and strains that remain undiscovered when using isotropic material models. These peak stresses and strains, at the interface of the calcification, can be a possible explanation for the fissures observed at these interfaces on histology [50]. Stress and strain are the first part of material failure; the second being material strength. Strength will be different for the 1 direction (along fibers) than for the 2 direction (across fibers). Although stress along fibers was larger in this study, the material might still fail due to the stress across fibers or shear stress between fibers, as the tissue strength may be smaller in these directions. The same argument holds for the case if the material fails due to strain: shear strain had the largest peak values of the strain metrics, but fibrous tissue, being less compliant along its direction, possibly fails at lower strain levels in this direction. The high stress and strain levels for the Attached pattern might be a reason for the controversy found in literature on calcifications and plaque vulnerability: this calcification type is related to the active calcification developmental pathway, and thus prevents inflammation in the plaque from further spreading, thereby biologically stabilizing the plaque [27, 29]. However, biomechanically, it leads to stress concentration. The fibers themselves become calcified during the calcification process, while for the other patterns the fibers are able to realign, possibly to prevent adverse mechanical states.

Stress/strain at the calcification interface could be predicted by the calcification geometric features. Many stress/strain metrics showed the same response to changes in geometric features, and in the end, it was found that for three of the four fiber patterns only stress along fibers S_{11} and stress across fibers S_{22} were needed to predict the stress/strain response at the calcification interface, for the Encircling pattern also strain along fibers E_{11} was needed (Chapter 5, Tables 5.1-5.4). In general, stress and strain increased if the calcification was moved closer to the lumen (decreasing values for normalized distance D_{norm}) (Chapter 5, Section 5.4.1). This agrees with medical studies showing that ruptured plaques had more superficial calcifications (e.g. see [43]) and other biomechanical studies showing increased stresses for calcifications close to the lumen (e.g. see [55, 61]). Reason for this is that stresses and strains already are larger at the lumen, because of the blood pressure on the lumen wall. Stress and strain also increased for increasing values of calcification length/width ratio A_{calc}, an effect that is also found in biomechanical modeling [55], and possibly caused by the increased curvature at the calcification tip for increasing values of A_{calc}. Stress and strain also increased for increasing values of normalized width W_{norm}, indicating that stresses and strains are larger for increasing calcification size. Results on this feature are controversial in literature; some biomechanical studies found that large calcifications can be destabilizing [53], while other studies found that only small calcifications, in the micrometer range, increase stresses [60].

The contribution of each of the parameters to the stress/strain metrics differed per fiber pattern; e.g. for the Attached pattern calcification aspect ratio A_{calc} had a contribution which was twice as large as the contribution of normalized width W_{norm} (Tables 5.5 & 5.6), while for the Pushed Aside pattern

normalized width had a larger contribution than aspect ratio (Tables 5.7 & 5.8).

The Attached pattern had the largest stresses in the direct comparison between fiber patterns, and the morphometric analysis showed that calcifications belonging to this pattern could develop the largest aspect ratio structures of the four fiber patterns. These two features combined resulted in the large stress differences observed between this pattern and the other three fiber patterns. The Random interaction was mostly found deep in the plaque tissue in the morphometric analysis. Its interface stress, already lower in the direct comparison between fiber patterns, was therefore even lower because interface stresses decreased for increasing lumen distance.

For the biomechanical modeling part, a generic non patient-specific 2D geometry was used. Patient specific models will give more accurate stress results, as these results are highly dependent on plaque geometry. However, this study was parametric and aimed at stress differences between fibrous tissue patterns and how stresses can be predicted by calcification geometric features. The generic geometries therefore served the purpose of this study well; only relative stresses were important. For these 2D geometries a plane strain assumption was made, which is a fair assumption, because plaque geometry does not change significantly in axial direction.

The biomechanical models lacked the presence of a lipid pool, one of the key morphological features of a plaque. A soft inclusion like this will redistribute the stresses in the plaque significantly. However, this redistribution of stresses is not present in the FE models of this study. The effect of a lipid pool on the stresses around a calcification is complex and depends on the relative position of these two plaque constituents [65]. Investigating the effect of a lipid pool in the presence of the calcification and the fibrous tissue patterns is beyond the scope of this study, and would be a study on its own.

Another model design choice was that the calcification and the fibrous tissue were perfectly bonded together, while in reality different interface properties might exist. In the Attached pattern the fibers continue inside the calcification, in the other fiber patterns the calcification is between the fibers, and properties at these interfaces might differ. Damage at the interface might initiate for certain fiber patterns at loading conditions used in this study. However, these interface properties could not be incorporated in the models, since they are not available.

An uncertainty in the biomechanical models was the choice of the material parameters for all plaque tissues. Wide ranges of parameters are reported in literature for fibrous tissue [85] and calcifications [81]. Stiffness of the fibrous tissue might be patient-specific, and the stiffness of the calcification might differ between fiber patterns, because there are different developmental pathways for calcifications. However, it is found that stress computations are not very sensitive to variations in the calcification stiffness value [84].

7

Conclusions and Recommendations

Rupture of an atherosclerotic plaque is a mechanical failure of the fibrous plaque tissue, and the underlying cause of heart attack and stroke, the two leading causes of death worldwide [1, 3, 4]. A large lipid pool and a thin fibrous cap are well-accepted components that determine plaque vulnerability in both histopathological and biomechanical studies [37, 38]. Calcification is also a highly prevalent plaque component, however, its influence on plaque stability is still unclear. Clinical studies demonstrated a strong correlation of calcification amount and presence with cardiovascular symptomatology [40, 41]. Moreover, a recent histopathological study evidenced fibrous tissue fissures starting from or extending to calcification-fibrous tissue interfaces in plaques [50], potentially caused by an unfavourable mechanical state of the plaque at this interface. Contrarily, biomechanical studies majorly claim that calcifications help in stabilizing plaques by lowering plaque stresses [57, 58].

The disagreement between biomechanical studies and clinical findings might be due to 1) simplistic modeling of calcification-tissue interaction in computational studies by using isotropic material models for the anisotropic plaque tissue, and 2) calcification morphology (size, shape, location) might be determinant, however this is never analyzed in detail for its biomechanical impact.

The aim of this study was twofold. Hypothesizing that stress and strain concentrations are likely at the calcification-tissue interface and might lead to fissure initiation, this study investigated the impact of 1) local anisotropy of fibrous tissue surrounding the calcification and 2) calcification morphology on interface stresses. This study for the first time 1) identifies calcification shape, location, size and anisotropy of surrounding fibrous plaque tissue in detail, and 2) the impact of these geometric features on interface stresses and strains.

This study consisted of two main stages: a morphometric analysis of calcified plaques and a computational FE analysis for interface stress and strain assessment based on the results of morphometric analysis. The morphometric analysis was performed on carotid endarterectomy samples and each segmented calcification with its corresponding local fibrous tissue alignment was subsequently modeled in FE software for interface stress and strain analysis. The twofold aim of this study resulted in two research questions, which were addressed separately (see the introduction chapter). Concluding answers to these separate questions will be given next.

(i) How does local anisotropy of the fibrous tissue surrounding calcifications influence stresses and strains at the interface of these two plaque materials?

Four dominant fiber alignment patterns, that determine the anisotropy of fibrous tissue surrounding calcifications, are prevalent for atherosclerotic plaques: the Attached pattern, Pushed Aside pattern, Encircling pattern and the Random pattern. These four fiber patterns largely affect the stress and strain calculations at the calcification interface, and interface stresses can be as large or even larger than the stresses at the lumen. The Attached pattern resulted in the largest stresses and strains, followed by the Pushed Aside pattern. The Encircling pattern and Random pattern generally have low stresses

and strains at the interface compared to the other two fiber patterns. These differences are further emphasized by the series of computational models driven by the morphometric analysis measurements. Peak stress and strain values are attained at the tip of the calcification, in circumferential direction of the plaque.

(ii) How are these interface stresses and strains influenced by the calcification geometric features?

Interface stresses and strains are greatly dependent on the geometric features of the calcification, including location in the plaque, shape and size. The closer a calcification is to the lumen, the higher the interface stress and strain. Increasing the ellipticity (aspect ratio) of the calcification also increases the stress and strain at the calcification interface. Furthermore, stresses and strains increase if the calcification size is increased. The Attached pattern is associated with larger calcifications which can also have larger aspect ratios compared to the other fiber patterns. This, combined with the already larger interface stresses and strains for this fiber pattern, results in stresses and strains that are significantly larger than those at the interfaces of other calcifications.

The individual impact of each of the geometric features on the stress or strain differs for each of the fiber patterns, and the total effect of one of the geometric features on stress and strain can depend on values of the other geometric features via interactions. The total effect of calcification aspect ratio on stress and strain can depend on the distance of the calcification to the lumen for example.

This study was the first to investigate the orientation of collagen fibers in the vicinity of calcifications, its influence on stress and strain calculations and how these stresses and strains are influenced by the geometric features of the calcifications. It was able to discern distinct patterns of fiber alignment, and to segment and categorize calcifications accordingly. It thereby improved biomechanical modeling of atherosclerotic plaques by introducing material anisotropy in the FE models. This revealed peak stresses and strains which are not observable in previously used models, with isotropic material models. These peak stresses and strains co-localized with damage found on histology: at the interface between calcification and fibrous tissue [50]. This study therefore further emphasizes the predictive power of computational models in plaque vulnerability assessment. The clinical relevance of biomechanical modeling of plaques is to predict plaque rupture, by finding geometric features and materials which elevate plaque stresses or strains. By finding previously unobserved stress/strain concentration locations, this study increased the accuracy of rupture risk prediction in plaques. The peak stresses and strains indicate that calcifications, while biologically stabilizing the plaque in certain cases [27], might destabilize the plaque mechanically. This contradictory effect of calcifications on the overall stability of the plaque might explain the controversial results found in literature.

The stress and strain elevating calcification geometric features found in this study add to the clinical relevance by predicting which calcification shapes and locations destabilize the plaque. These features can be obtained when the plaque is imaged. Computed tomography (CT) imaging is a suited modality for this, as the dense calcifications show up as bright white spots on the grey surrounding tissue. However, no general trend between stress/strain outcome and calcification geometric features was found; the effect of the geometric features depend on the specific fiber pattern surrounding the calcification. Therefore, to accurately predict the vulnerability of the plaque of a patient, means of objectively obtaining the fiber alignment *in vivo* are needed. One possible solution is diffusion tensor imaging (DTI) [69], but to be able to detect local fiber orientation, spatial resolution of this modality needs to be improved.

Stresses and strains are one part of plaque vulnerability prediction, the second part is material strength. Damage initiation and progression would therefore significantly improve rupture prediction in FE models. It is known that rupture of plaque tissue can start or end at interfaces between calcifications and fibrous tissue [50], and this study clearly demonstrated that stress and strain concentrations develop at the calcification-tissue interface. It is important to find damage parameters for each fiber pattern individually; the Attached pattern has higher interface stresses, but the interface for this fiber pattern might also have a higher strength than the other fiber patterns for example. These damage parameters must describe if plaque tissue fails due to peak stresses or peak strains and specifically which stress or strain metrics are the cause of tissue failure. Studies investigating the micromechanical properties

at the interface of calcifications and fibrous tissue are therefore needed, together with the introduction of damage initiation and propagation in plaque biomechanical models, by using methods like the extended finite element method (XFEM) or cohesive zone modeling (CZM).

This study investigated fibrous tissue alignment patterns and calcification geometric features on carotid endarterectomy samples. An extension of this would be the investigation of patterns and geometric features on coronary plaques. It is possible that results differ between these vasculatures.

An addition to this parametric study would be a study investigating the effect of a lipid pool on the interface stresses. Now that the influence of fiber patterns and calcification geometric features on interface stress computations are known, the effect of a lipid pool on these stresses will be of additional value. Such a study can also be parametric, where shape, size and relative location (with respect to the calcification) of the lipid pool will be the driving parameters.

Bibliography

[1] *Fact sheet: Cardiovascular diseases (CVDs)*, World Health Organization (2015 (accessed May 31, 2018)), http://www.who.int/news-room/fact-sheets/detail/cardiovascular-diseases-(cvds).

[2] M. J and M. G, *The atlas of heart disease and Stroke, sheet N^o 13: Global burden of coronary heart disease*, World Health Organization (2004 (accessed May 31, 2018)), http://www.who.int/cardiovascular_diseases/en/cvd_atlas_13_coronaryHD.pdf?ua=1.

[3] E. Falk, P. K. Shah, and V. Fuster, *Coronary plaque disruption,* Circulation **92**, 657 (1995).

[4] L. G. Spagnoli, A. Mauriello, G. Sangiorgi, S. Fratoni, E. Bonanno, R. S. Schwartz, D. G. Piepgras, R. Pistolese, A. Ippoliti, and D. R. Holmes, *Extracranial thrombotically active carotid plaque as a risk factor for ischemic stroke,* Jama **292**, 1845 (2004).

[5] E. N. Marieb and K. Hoehn, *Human Anatomy & Physiology Tenth Edition Global Edition* (Pearson, 2016).

[6] S. A. I. Ghesquiere, *The role of phospholipases in atherosclerosis*, Ph.D. thesis, Maastricht University, Netherlands (2006).

[7] *Carotid Artery Disease*, Harvard Health Publishing (2015 (accessed June 23, 2018)), https://www.health.harvard.edu/heart-disease-overview/carotid-artery-disease-overview.

[8] D. N. Ku, D. P. Giddens, C. K. Zarins, and S. Glagov, *Pulsatile flow and atherosclerosis in the human carotid bifurcation. Positive correlation between plaque location and low oscillating shear stress.* Arteriosclerosis, thrombosis, and vascular biology **5**, 293 (1985).

[9] C. Slager, J. Wentzel, F. Gijsen, J. Schuurbiers, A. Van der Wal, A. Van der Steen, and P. Serruys, *The role of shear stress in the generation of rupture-prone vulnerable plaques,* Nature Reviews Cardiology **2**, 401 (2005).

[10] R. Ross, *The pathogenesis of atherosclerosis: a perspective for the 1990s,* Nature **362**, 801 (1993).

[11] H. C. Stary, A. B. Chandler, S. Glagov, J. R. Guyton, W. Insull, M. E. Rosenfeld, S. A. Schaffer, C. J. Schwartz, W. D. Wagner, and R. W. Wissler, *A definition of initial, fatty streak, and intermediate lesions of atherosclerosis. A report from the Committee on Vascular Lesions of the Council on Arteriosclerosis, American Heart Association.* Circulation **89**, 2462 (1994).

[12] H. C. Stary, A. B. Chandler, R. E. Dinsmore, V. Fuster, S. Glagov, W. Insull, M. E. Rosenfeld, C. J. Schwartz, W. D. Wagner, and R. W. Wissler, *A definition of advanced types of atherosclerotic lesions and a histological classification of atherosclerosis: a report from the Committee on Vascular Lesions of the Council on Arteriosclerosis, American Heart Association,* Circulation **92**, 1355 (1995).

[13] P. R. Moreno, K. R. Purushothaman, V. Fuster, and W. N. O'connor, *Intimomedial interface damage and adventitial inflammation is increased beneath disrupted atherosclerosis in the aorta: implications for plaque vulnerability,* Circulation **105**, 2504 (2002).

[14] K. Kohchi, S. Takebayashi, T. Hiroki, and M. Nobuyoshi, *Significance of adventitial inflammation of the coronary artery in patients with unstable angina: results at autopsy.* Circulation **71**, 709 (1985).

[15] S. Yusuf, S. Reddy, S. Ôunpuu, and S. Anand, *Global burden of cardiovascular diseases: part I: general considerations, the epidemiologic transition, risk factors, and impact of urbanization,* Circulation **104**, 2746 (2001).

[16] G. B. Ehret, P. B. Munroe, K. M. Rice, M. Bochud, A. D. Johnson, D. I. Chasman, A. V. Smith, M. D. Tobin, G. C. Verwoert, S.-J. Hwang, *et al.*, *Genetic variants in novel pathways influence blood pressure and cardiovascular disease risk,* Nature **478**, 103 (2011).

[17] A. J. Lusis, *Atherosclerosis,* Nature **407**, 233 (2000).

[18] J. A. Berliner, M. Navab, A. M. Fogelman, J. S. Frank, L. L. Demer, P. A. Edwards, A. D. Watson, and A. J. Lusis, *Atherosclerosis: basic mechanisms: oxidation, inflammation, and genetics,* Circulation **91**, 2488 (1995).

[19] S. M. Schwartz, R. Virmani, and M. E. Rosenfeld, *The good smooth muscle cells in atherosclerosis,* Current atherosclerosis reports **2**, 422 (2000).

[20] E. Falk, *Pathogenesis of atherosclerosis,* Journal of the American College of Cardiology **47**, C7 (2006).

[21] P. Libby, *Changing concepts of atherogenesis,* Journal of internal medicine **247**, 349 (2000).

[22] S. Glagov, E. Weisenberg, C. K. Zarins, R. Stankunavicius, and G. J. Kolettis, *Compensatory enlargement of human atherosclerotic coronary arteries,* New England Journal of Medicine **316**, 1371 (1987).

[23] R. Ross, *Atherosclerosis—an inflammatory disease,* New England journal of medicine **340**, 115 (1999).

[24] F. Otsuka, K. Sakakura, K. Yahagi, M. Joner, and R. Virmani, *Has Our Understanding of Calcification in Human Coronary Atherosclerosis Progressed? Significance,* Arteriosclerosis, thrombosis, and vascular biology **34**, 724 (2014).

[25] M. Naghavi, P. Libby, E. Falk, S. W. Casscells, S. Litovsky, J. Rumberger, J. J. Badimon, C. Stefanadis, P. Moreno, G. Pasterkamp, *et al.*, *From vulnerable plaque to vulnerable patient: a call for new definitions and risk assessment strategies: Part I,* Circulation **108**, 1664 (2003).

[26] J. Nelson, O. Wani, H. May, and M. Budoff, *Potential benefits of eicosapentaenoic acid on atherosclerotic plaques,* Vascular pharmacology **91**, 1 (2017).

[27] G. Pugliese, C. Iacobini, C. B. Fantauzzi, and S. Menini, *The dark and bright side of atherosclerotic calcification,* Atherosclerosis **238**, 220 (2015).

[28] J. D. Hutcheson, C. Goettsch, S. Bertazzo, N. Maldonado, J. L. Ruiz, W. Goh, K. Yabusaki, T. Faits, C. Bouten, G. Franck, *et al.*, *Genesis and growth of extracellular-vesicle-derived microcalcification in atherosclerotic plaques,* Nature materials **15**, 335 (2016).

[29] J. L. Hunt, R. Fairman, M. E. Mitchell, J. P. Carpenter, M. Golden, T. Khalapyan, M. Wolfe, D. Neschis, R. Milner, B. Scoll, *et al.*, *Bone formation in carotid plaques: a clinicopathological study,* Stroke **33**, 1214 (2002).

[30] A. P. Sage, Y. Tintut, and L. L. Demer, *Regulatory mechanisms in vascular calcification,* Nature Reviews Cardiology **7**, 528 (2010).

[31] J. J. Ricotta, A. AbuRahma, E. Ascher, M. Eskandari, P. Faries, and B. K. Lal, *Updated Society for Vascular Surgery guidelines for management of extracranial carotid disease,* Journal of vascular surgery **54**, e1 (2011).

[32] T. G. Brott, R. W. Hobson, G. Howard, G. S. Roubin, W. M. Clark, W. Brooks, A. Mackey, M. D. Hill, P. P. Leimgruber, A. J. Sheffet, *et al.*, *Stenting versus endarterectomy for treatment of carotid-artery stenosis,* New England Journal of Medicine **363**, 11 (2010).

[33] P. M. Rothwell and C. P. Warlow, *Prediction of benefit from carotid endar terectomy in individual patients: a risk-modelling study,* The Lancet **353**, 2105 (1999).

[34] P. K. Shah, *Mechanisms of plaque vulnerability and rupture,* Journal of the American college of cardiology **41**, S15 (2003).

[35] J. A. Schaar, J. E. Muller, E. Falk, R. Virmani, V. Fuster, P. W. Serruys, A. Colombo, C. Stefanadis, S. Ward Casscells, P. R. Moreno, *et al.*, *Terminology for high-risk and vulnerable coronary artery plaques,* European heart journal **25**, 1077 (2004).

[36] L. Badimon and G. Vilahur, *Thrombosis formation on atherosclerotic lesions and plaque rupture,* Journal of internal medicine **276**, 618 (2014).

[37] R. Virmani, F. D. Kolodgie, A. P. Burke, A. V. Finn, H. K. Gold, T. N. Tulenko, S. P. Wrenn, and J. Narula, *Atherosclerotic plaque progression and vulnerability to rupture: angiogenesis as a source of intraplaque hemorrhage,* Arteriosclerosis, thrombosis, and vascular biology **25**, 2054 (2005).

[38] A. C. Akyildiz, L. Speelman, H. van Brummelen, M. A. Gutiérrez, R. Virmani, A. van der Lugt, A. F. van der Steen, J. J. Wentzel, and F. J. Gijsen, *Effects of intima stiffness and plaque morphology on peak cap stress,* Biomedical engineering online **10**, 25 (2011).

[39] Z.-Y. Li, T. Tang, M. Graves, M. Sutcliffe, J. H. Gillard, *et al.*, *Assessment of carotid plaque vulnerability using structural and geometrical determinants,* Circulation Journal **72**, 1092 (2008).

[40] M. J. Budoff, L. J. Shaw, S. T. Liu, S. R. Weinstein, P. H. Tseng, F. R. Flores, T. Q. Callister, P. Raggi, D. S. Berman, and T. P. Mosler, *Long-term prognosis associated with coronary calcification: observations from a registry of 25,253 patients,* Journal of the American College of Cardiology **49**, 1860 (2007).

[41] A. H. Qazi, F. Zallaghi, N. Torres-Acosta, R. C. Thompson, and J. H. O'Keefe, *Computed tomography for coronary artery calcification scoring: mammogram for the heart,* Progress in cardiovascular diseases **58**, 529 (2016).

[42] M. Sakaguchi, T. Hasegawa, S. Ehara, K. Matsumoto, K. Mizutani, T. Iguchi, H. Ishii, M. Nakagawa, K. Shimada, and M. Yoshiyama, *New insights into spotty calcification and plaque rupture in acute coronary syndrome: an optical coherence tomography study,* Heart and vessels **31**, 1915 (2016).

[43] Y. Zhan, Y. Zhang, J. Hou, G. Lin, and B. Yu, *Relation between superficial calcifications and plaque rupture: an optical coherence tomography study,* Canadian Journal of Cardiology **33**, 991 (2017).

[44] G. A. Holzapfel, G. Sommer, and P. Regitnig, *Anisotropic mechanical properties of tissue components in human atherosclerotic plaques,* Journal of biomechanical engineering **126**, 657 (2004).

[45] M. A. Jankowska, M. Bartkowiak-Jowsa, and R. Bedzinski, *Experimental and constitutive modeling approaches for a study of biomechanical properties of human coronary arteries,* Journal of the mechanical behavior of biomedical materials **50**, 1 (2015).

[46] H. Barrett, E. Cunnane, E. Kavanagh, and M. Walsh, *On the effect of calcification volume and configuration on the mechanical behaviour of carotid plaque tissue,* Journal of the mechanical behavior of biomedical materials **56**, 45 (2016).

[47] J. Mulvihill, E. Cunnane, S. McHugh, E. Kavanagh, S. Walsh, and M. Walsh, *Mechanical, biological and structural characterization of in vitro ruptured human carotid plaque tissue,* Acta biomaterialia **9**, 9027 (2013).

[48] E. Cunnane, J. Mulvihill, H. Barrett, D. Healy, E. Kavanagh, S. Walsh, and M. Walsh, *Mechanical, biological and structural characterization of human atherosclerotic femoral plaque tissue,* Acta biomaterialia **11**, 295 (2015).

[49] P. J. Fitzgerald, T. A. Ports, and P. G. Yock, *Contribution of localized calcium deposits to dissection after angioplasty. An observational study using intravascular ultrasound.* Circulation **86**, 64 (1992).

[50] M. J. Daemen, M. S. Ferguson, F. J. Gijsen, D. S. Hippe, M. E. Kooi, K. Demarco, A. C. van der Wal, C. Yuan, and T. S. Hatsukami, *Carotid plaque fissure: an underestimated source of intraplaque hemorrhage,* Atherosclerosis **254**, 102 (2016).

[51] G. A. Holzapfel, J. J. Mulvihill, E. M. Cunnane, and M. T. Walsh, *Computational approaches for analyzing the mechanics of atherosclerotic plaques: a review,* Journal of biomechanics **47**, 859 (2014).

[52] P. D. Richardson, M. Davies, and G. Born, *Influence of plaque configuration and stress distribution on fissuring of coronary atherosclerotic plaques,* The Lancet **334**, 941 (1989).

[53] Z. Teng, A. J. Brown, P. A. Calvert, R. A. Parker, D. R. Obaid, Y. Huang, S. P. Hoole, N. E. West, J. H. Gillard, and M. R. Bennett, *Coronary plaque structural stress is associated with plaque composition and subtype and higher in acute coronary syndrome: the BEACON I (Biomechanical Evaluation of Atheromatous Coronary Arteries) study,* Circulation: Cardiovascular Imaging , CIRCIMAGING (2014).

[54] A. J. Brown, Z. Teng, P. A. Calvert, N. K. Rajani, O. Hennessy, N. Nerlekar, D. R. Obaid, C. Costopoulos, Y. Huang, S. P. Hoole, *et al.*, *Plaque Structural Stress Estimations Improve Prediction of Future Major Adverse Cardiovascular Events After Intracoronary ImagingCLINICAL PERSPECTIVE,* Circulation: Cardiovascular Imaging **9**, e004172 (2016).

[55] C. M. Buffinton and D. M. Ebenstein, *Effect of calcification modulus and geometry on stress in models of calcified atherosclerotic plaque,* Cardiovascular Engineering and Technology **5**, 244 (2014).

[56] D. Tang, C. Yang, J. Zheng, P. K. Woodard, J. E. Saffitz, G. A. Sicard, T. K. Pilgram, and C. Yuan, *Quantifying effects of plaque structure and material properties on stress distributions in human atherosclerotic plaques using 3D FSI models,* Journal of biomechanical engineering **127**, 1185 (2005).

[57] D. E. Kiousis, S. F. Rubinigg, M. Auer, and G. A. Holzapfel, *A methodology to analyze changes in lipid core and calcification onto fibrous cap vulnerability: the human atherosclerotic carotid bifurcation as an illustratory example,* Journal of biomechanical engineering **131**, 121002 (2009).

[58] H. Huang, R. Virmani, H. Younis, A. P. Burke, R. D. Kamm, and R. T. Lee, *The impact of calcification on the biomechanical stability of atherosclerotic plaques,* Circulation **103**, 1051 (2001).

[59] K. Imoto, T. Hiro, T. Fujii, A. Murashige, Y. Fukumoto, G. Hashimoto, T. Okamura, J. Yamada, K. Mori, and M. Matsuzaki, *Longitudinal structural determinants of atherosclerotic plaque vulnerability: a computational analysis of stress distribution using vessel models and three-dimensional intravascular ultrasound imaging,* Journal of the American College of Cardiology **46**, 1507 (2005).

[60] Y. Vengrenyuk, L. Cardoso, and S. Weinbaum, *Micro-CT based analysis of a new paradigm for vulnerable plaque rupture: cellular microcalcifications in fibrous caps,* Molecular and Cellular Biomechanics **5**, 37 (2008).

[61] Z.-Y. Li, S. Howarth, T. Tang, M. Graves, U. Jean, J. H. Gillard, *et al.*, *Does calcium deposition play a role in the stability of atheroma? Location may be the key,* Cerebrovascular diseases **24**, 452 (2007).

[62] A. Kelly-Arnold, N. Maldonado, D. Laudier, E. Aikawa, L. Cardoso, and S. Weinbaum, *Revised microcalcification hypothesis for fibrous cap rupture in human coronary arteries,* Proceedings of the National Academy of Sciences **110**, 10741 (2013).

[63] N. Maldonado, A. Kelly-Arnold, L. Cardoso, and S. Weinbaum, *The explosive growth of small voids in vulnerable cap rupture; cavitation and interfacial debonding,* Journal of biomechanics **46**, 396 (2013).

[64] N. Maldonado, A. Kelly-Arnold, Y. Vengrenyuk, D. Laudier, J. T. Fallon, R. Virmani, L. Cardoso, and S. Weinbaum, *A mechanistic analysis of the role of microcalcifications in atherosclerotic plaque stability: potential implications for plaque rupture,* American Journal of Physiology-Heart and Circulatory Physiology **303**, H619 (2012).

[65] T. Hoshino, L. A. Chow, J. J. Hsu, A. A. Perlowski, M. Abedin, J. Tobis, Y. Tintut, A. K. Mal, W. S. Klug, and L. L. Demer, *Mechanical stress analysis of a rigid inclusion in distensible material: a model of atherosclerotic calcification and plaque vulnerability,* American Journal of Physiology-Heart and Circulatory Physiology **297**, H802 (2009).

[66] K. K. Wong, P. Thavornpattanapong, S. C. Cheung, Z. Sun, and J. Tu, *Effect of calcification on the mechanical stability of plaque based on a three-dimensional carotid bifurcation model,* BMC cardiovascular disorders **12**, 7 (2012).

[67] I. Del Rincon, *Atherosclerosis in rheumatoid arthritis: What to look for in studies using carotid ultrasound,* (2010).

[68] Z. Teng, J. He, U. Sadat, J. R. Mercer, X. Wang, N. S. Bahaei, O. M. Thomas, and J. H. Gillard, *How does juxtaluminal calcium affect critical mechanical conditions in carotid atherosclerotic plaque? An exploratory study,* IEEE Transactions on Biomedical Engineering **61**, 35 (2014).

[69] A. C. Akyildiz, C.-K. Chai, C. W. Oomens, A. van der Lugt, F. P. Baaijens, G. J. Strijkers, and F. J. Gijsen, *3D fiber orientation in atherosclerotic carotid plaques,* Journal of structural biology **200**, 28 (2017).

[70] G. R. Douglas, A. J. Brown, J. H. Gillard, M. R. Bennett, M. P. Sutcliffe, and Z. Teng, *Impact of fiber structure on the material stability and rupture mechanisms of coronary atherosclerotic plaques,* Annals of biomedical engineering **45**, 1462 (2017).

[71] R. Virmani, F. D. Kolodgie, A. P. Burke, A. Farb, and S. M. Schwartz, *Lessons from sudden coronary death: a comprehensive morphological classification scheme for atherosclerotic lesions,* Arteriosclerosis, thrombosis, and vascular biology **20**, 1262 (2000).

[72] J. N. Redgrave, P. Gallagher, J. K. Lovett, and P. M. Rothwell, *Critical cap thickness and rupture in symptomatic carotid plaques: the oxford plaque study,* Stroke **39**, 1722 (2008).

[73] A. Mauriello, F. Servadei, G. B. Zoccai, E. Giacobbi, L. Anemona, E. Bonanno, and S. Casella, *Coronary calcification identifies the vulnerable patient rather than the vulnerable plaque,* Atherosclerosis **229**, 124 (2013).

[74] J. Krejza, M. Arkuszewski, S. E. Kasner, J. Weigele, A. Ustymowicz, R. W. Hurst, B. L. Cucchiara, and S. R. Messe, *Carotid artery diameter in men and women and the relation to body and neck size,* Stroke **37**, 1103 (2006).

[75] E. C. S. T. C. Group *et al.*, *Randomised trial of endarterectomy for recently symptomatic carotid stenosis: final results of the MRC European Carotid Surgery Trial (ECST),* The Lancet **351**, 1379 (1998).

[76] T. Ohara, K. Toyoda, R. Otsubo, K. Nagatsuka, Y. Kubota, M. Yasaka, H. Naritomi, and K. Minematsu, *Eccentric stenosis of the carotid artery associated with ipsilateral cerebrovascular events,* American Journal of Neuroradiology **29**, 1200 (2008).

[77] M. Wong, J. Edelstein, J. Wollman, and M. G. Bond, *Ultrasonic-pathological comparison of the human arterial wall. Verification of intima-media thickness.* Arteriosclerosis and thrombosis: a journal of vascular biology **13**, 482 (1993).

[78] M. Hokari, S. Kuroda, H. Yasuda, N. Nakayama, S. Abe, Y. Iwasaki, and H. Saito, *Lumen Morphology in Mild-to-Moderate Internal Carotid Artery Stenosis Correlates with Neurological Symptoms,* Journal of Neuroimaging **21**, 348 (2011).

[79] T. Saam, C. Yuan, B. Chu, N. Takaya, H. Underhill, J. Cai, N. Tran, N. L. Polissar, B. Neradilek, G. P. Jarvik, *et al.*, *Predictors of carotid atherosclerotic plaque progression as measured by noninvasive magnetic resonance imaging,* Atherosclerosis **194**, e34 (2007).

[80] T. C. Gasser, R. W. Ogden, and G. A. Holzapfel, *Hyperelastic modelling of arterial layers with distributed collagen fibre orientations,* Journal of the royal society interface **3**, 15 (2006).

[81] D. M. Ebenstein, D. Coughlin, J. Chapman, C. Li, and L. A. Pruitt, *Nanomechanical properties of calcification, fibrous tissue, and hematoma from atherosclerotic plaques,* Journal of Biomedical Materials Research Part A: An Official Journal of The Society for Biomaterials, The Japanese Society for Biomaterials, and The Australian Society for Biomaterials and the Korean Society for Biomaterials **91**, 1028 (2009).

[82] H. F. Choi and S. S. Blemker, *Skeletal muscle fascicle arrangements can be reconstructed using a laplacian vector field simulation,* PloS one **8**, e77576 (2013).

[83] G. G. Handsfield, B. Bolsterlee, J. M. Inouye, R. D. Herbert, T. F. Besier, and J. W. Fernandez, *Determining skeletal muscle architecture with Laplacian simulations: a comparison with diffusion tensor imaging,* Biomechanics and modeling in mechanobiology **16**, 1845 (2017).

[84] S. Williamson, Y. Lam, H. Younis, H. Huang, S. Patel, M. Kaazempur-Mofrad, and R. Kamm, *On the sensitivity of wall stresses in diseased arteries to variable material properties,* Journal of biomechanical engineering **125**, 147 (2003).

[85] A. C. Akyildiz, L. Speelman, and F. J. Gijsen, *Mechanical properties of human atherosclerotic intima tissue,* Journal of biomechanics **47**, 773 (2014).

A

Correlation Tables

Table A.1: Spearman's correlation for all parameters, for the attached fibers interaction. $|r_s| > 0.500$ Values are highlighted in bold.

		Correlations (r_s)								
		1	*2*	*3*	*4*	*5*	*6*	*7*	*8*	*9*
1	D_{bif}	1								
2	D_{inner}	0.248*	1							
3	D_{outer}	-0.041	**-0.515***	1						
4	D_{norm}	0.141	**0.859***	**-0.866***	1					
5	L_{calc}	-0.051	0.216	0.118	0.045	1				
6	W_{calc}	0.113	0.168	0.224	-0.024	**0.590***	1			
7	A_{calc}	-0.271*	0.028	-0.121	0.061	0.346*	-0.467*	1		
8	W_{norm}	0.055	-0.039	0.051	-0.038	0.429*	**0.863***	**-0.549***	1	
9	D_{cap}	0.181	**0.876***	**-0.645***	**0.863***	-0.054	-0.179	0.195	-0.328*	1

* Correlation is significant at the $P < 0.05$ level.

Table A.2: Spearman's correlation for all parameters, for the pushed aside fibers interaction. $|r_s| > 0.500$ Values are highlighted in bold.

		Correlations (r_s)								
		1	*2*	*3*	*4*	*5*	*6*	*7*	*8*	*9*
1	D_{bif}	1								
2	D_{inner}	0.116	1							
3	D_{outer}	-0.042	-0.165	1						
4	D_{norm}	0.178	**0.822***	**-0.648***	1					
5	L_{calc}	-0.103	-0.070	-0.045	-0.119	1				
6	W_{calc}	-0.261	-0.183	-0.090	-0.198	**0.861***	1			
7	A_{calc}	0.249	0.106	0.181	-0.025	0.272	-0.160	1		
8	W_{norm}	-0.229	-0.456*	-0.314	-0.256	**0.740***	**0.894***	-0.200	1	
9	D_{cap}	0.187	**0.969***	-0.121	**0.815***	-0.222	-0.362	0.132	**-0.602***	1

* Correlation is significant at the $P < 0.05$ level.

Table A.3: Spearman's correlation for all parameters, for the encircling fibers interaction. $|r_s| > 0.500$ Values are highlighted in bold.

		Correlations (r_s)								
		1	*2*	*3*	*4*	*5*	*6*	*7*	*8*	*9*
1	D_{bif}	1								
2	D_{inner}	0.248	1							
3	D_{outer}	-0.336*	-0.381*	1						
4	D_{norm}	0.363*	**0.869***	**-0.748***	1					
5	L_{calc}	-0.207	0.200	0.344*	-0.154	1				
6	W_{calc}	-0.154	0.095	0.301	-0.104	**0.776***	1			
7	A_{calc}	-0.105	-0.054	0.027	-0.020	0.438*	-0.178	1		
8	W_{norm}	-0.275	-0.403*	0.189	-0.408*	**0.573***	**0.755***	-0.148	1	
9	D_{cap}	0.254	**0.995***	-0.385*	**0.869***	-0.018	0.041	-0.034	-0.449*	1

* Correlation is significant at the $P < 0.05$ level.

Table A.4: Spearman's correlation for all parameters, for the random fibers interaction. $|r_s| > 0.500$ Values are highlighted in bold.

		Correlations (r_s)								
		1	*2*	*3*	*4*	*5*	*6*	*7*	*8*	*9*
1	D_{bif}	1								
2	D_{inner}	-0.105	1							
3	D_{outer}	-0.485	-0.099	1						
4	D_{norm}	0.343	**0.618***	**-0.787***	1					
5	L_{calc}	0.343	**-0.529***	0.012	-0.312	1				
6	W_{calc}	0.241	**-0.529***	0.386	**-0.624***	**0.776***	1			
7	A_{calc}	0.437	-0.238	**-0.645***	0.362	**0.582***	-0.012	1		
8	W_{norm}	0.225	**-0.776***	0.299	**-0.724***	**0.744***	**0.924***	0.065	1	
9	D_{cap}	-0.156	**0.979***	-0.159	**0.659***	**-0.556***	**-0.641***	-0.144	**-0.853***	1

* Correlation is significant at the $P < 0.05$ level.

B

Potential Flow and Conformal Mapping

> When a flow is both frictionless and irrotational, pleasant things happen
>
> F.M. White, Fluid Mechanics 4th ed.

The potential flow theory applied in Section subsection 4.1.3 of chapter 4 to mimic collagen fiber directions around a calcification in the Pushed Aside interaction has its origin in fluid mechanics, where external (fluid) flow around bodies (such as aerofoils) can be calculated using a potential function. It is assumed in potential flow theory that: (1) there is no vorticity present (called irrotational flow), (2) the fluid is incompressible, and (3) is inviscid (has no viscosity), the latter implying that it is also frictionless. Because of these simplifications, the analytical solution is relatively simple. Furthermore, only the steady-state flow is regarded, eliminating time dependent behaviour. The potential function describes the velocity field V around the body by taking its gradient[1]:

$$V = \nabla\phi \tag{B.1}$$

where $\phi\,(x, y)$ is the potential function and ∇ the gradient operator (in 2D space):

$$\nabla = \left(\frac{\partial}{\partial x}, \frac{\partial}{\partial y}\right) \tag{B.2}$$

so that fluid velocities in x and y directions can be calculated by taking partial derivatives:

$$u = \frac{\partial\phi}{\partial x} \qquad v = \frac{\partial\phi}{\partial y}. \tag{B.3}$$

In vector calculus it is known that the curl (or rotation) of a gradient is always zero, thus:

$$curl\,(\nabla\phi) = \nabla \times \nabla\phi \equiv 0 \tag{B.4}$$

which means that taking the curl of the left hand side of Equation B.1, yielding the rotation or vorticity of the velocity field, is also zero:

$$curl\,(V) = \nabla \times V \equiv 0 \tag{B.5}$$

and thus assumption (1) is enforced. This is also the reason why the fluid is assumed to be inviscid (3), as viscosity would induce friction forces and thereby introduce vorticity. The divergence of the velocity field indicates how much the fluid expands or shrinks, so under assumption (2) this also is equal to zero, and hence the right hand side of Equation B.1 is also zero:

$$div\,(V) = div\,(\nabla\phi) = \nabla \cdot \nabla\phi = \nabla^2\phi \equiv 0. \tag{B.6}$$

[1] Frank M White. Fluid Mechanics Fourth Edition, 2017

Equation B.6 is a linear Laplace's equation, which means that, under the superposition principle, if ϕ_1 and ϕ_2 are solutions to this equation, then $\phi_1 + \phi_2$ is also a solution. A complicated flow can thus easily be constructed by adding multiple flows together.

Another way of representing the velocity field is using a stream function ψ. The solution of this stream function is always orthogonal to the solution of the potential function ϕ, and is graphically represented as streamlines, which are tangent to the velocity vectors at each point. Using this orthogonality, the solution of the velocity field V (Equation B.1) can be related to ψ as follows:

$$V = \nabla \times \psi, \tag{B.7}$$

and the partial derivatives in Equation B.3 can be rewritten as[1]:

$$\frac{\partial \psi}{\partial y} = \frac{\partial \phi}{\partial x} = u \qquad -\frac{\partial \psi}{\partial x} = \frac{\partial \phi}{\partial y} = v. \tag{B.8}$$

ψ Also satisfies the Laplace's equation (not shown here), meaning that if ψ_1 and ψ_2 are solutions to the Laplace's equation, so is $\psi_1 + \psi_2$.

Calculation of a potential flow over an ellipse is achieved by first finding a solution for a flow over a circle, and then transforming this solution to an ellipse, using conformal mapping. Conformal mapping is most easily done using transformations in the complex plane, where the real values of x and y are projected onto the complex plane as follows:

$$z = x + iy \tag{B.9}$$

or, more conveniently for some intermediate solutions, in polar coordinates:

$$z = r\left(\cos\theta + i\sin\theta\right), \tag{B.10}$$

where r is radius, and θ angle. The relations in Equation B.8 are Cauchy-Riemann relations, which means that they are complex differentiable. Because of this property the following mapping of Equation B.9 can be made:

$$f(z) = w \qquad \Rightarrow \qquad f(x + iy) = \phi + i\psi. \tag{B.11}$$

As already explained, the superposition principle holds for both ϕ and ψ, and Equation B.11 can be used to add multiple streams together until a flow over a circle is established. A flow over a circle is achieved by adding the solutions of a free stream, a source and a sink together. First the source and sink are added together, forming a so called doublet flow, the resulting doublet is then added to the free stream.

A free stream in the positive x direction has the following potential and stream functions respectively:

$$\phi = V_\infty r\cos(\theta) \tag{B.12}$$

$$\psi = V_\infty r\sin(\theta), \tag{B.13}$$

where V_∞ is the uniform free-stream velocity. The free stream is defined in polar coordinates to make the summation of this stream with a doublet flow more convenient. An example of free stream potential lines and stream lines is shown in Figure B.1a.

A source or sink is a diverging or converging flow respectively. The velocity field thus only has a radial component, and has the following potential and stream functions:

$$\phi = \frac{\Lambda}{2\pi} ln(r) \tag{B.14}$$

$$\psi = \frac{\Lambda}{2\pi}\theta, \tag{B.15}$$

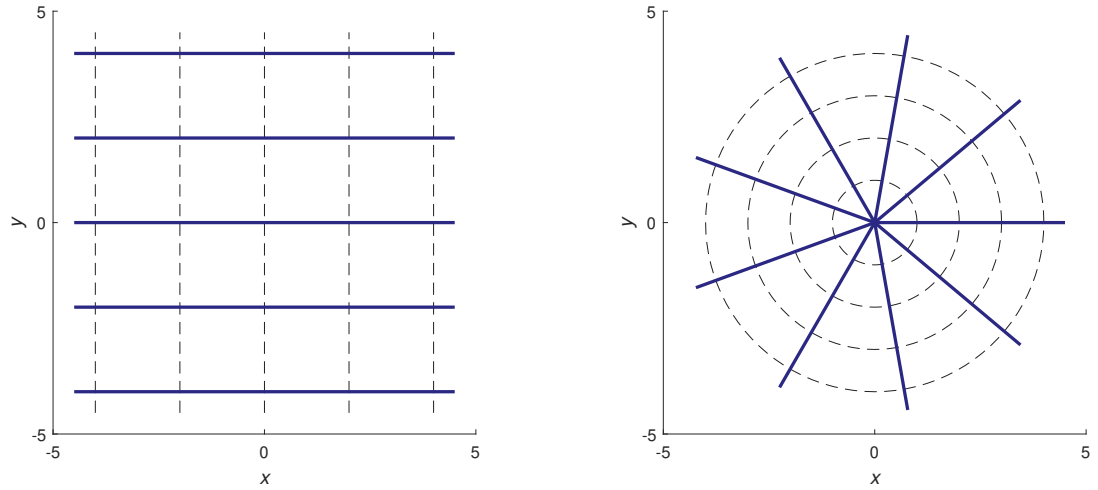

Figure B.1: Potential lines and stream lines of a free stream (a) and a source or sink (b). Dashed lines are the potential lines, dark blue lines the stream lines

where Λ is the strength of the source or sink, and is positive for a source and negative for a sink. Figure B.1b shows an example of a source or sink.
A doublet is created by placing a source and a sink at a certain distance from each other, and letting this distance shrink to zero. The resulting potential and stream functions are[1]:

$$\phi = \frac{\kappa}{2\pi}\frac{\cos(\theta)}{r} \tag{B.16}$$

$$\psi = -\frac{\kappa}{2\pi}\frac{\sin(\theta)}{r}, \tag{B.17}$$

where κ is the doublet strength. See Figure B.2a for an example of a doublet flow.

Now that we have a doublet, the free stream defined previously can be added using superposition to get the potential and stream functions of a flow over a circle:

$$\phi = \phi_{free\ stream} + \phi_{doublet} = V_\infty r\ \cos(\theta) + \frac{\kappa}{2\pi}\frac{\cos(\theta)}{r}, \tag{B.18}$$

$$\psi = \psi_{free\ stream} + \psi_{doublet} = V_\infty r\ \sin(\theta) - \frac{\kappa}{2\pi}\frac{\sin(\theta)}{r}. \tag{B.19}$$

The orthogonal velocity component is zero at the boundary between the doublet stream and the free stream (ψ = 0), and this boundary defines the radius R of the circle. Setting Equation B.19 to zero and solving for r yields the circle radius R:

$$\psi = 0 \quad \Rightarrow \quad V_\infty R\sin(\theta) = \frac{\kappa}{2\pi}\frac{\sin(\theta)}{R} \quad \Rightarrow \quad R^2 = \frac{\kappa}{2\pi V_\infty}. \tag{B.20}$$

Equations B.18 & B.19 can now be related to circle radius R:

$$\phi = V_\infty\left(r + \frac{R^2}{r}\right)\cos(\theta) \tag{B.21}$$

$$\psi = V_\infty\left(r - \frac{R^2}{r}\right)\sin(\theta). \tag{B.22}$$

The flow over a circle is visualized in Figure B.2b.

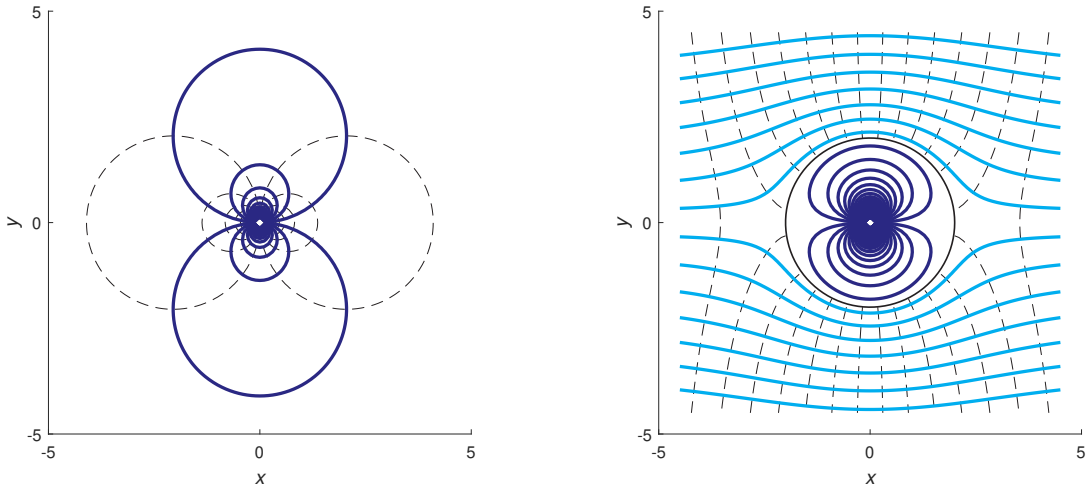

Figure B.2: Potential lines and stream lines of a doublet (a), and a flow over a circle (b). For clarity the potential lines of the doublet in (b) are left out. Dashed lines are potential lines, dark and light blue lines are stream lines. In (b) the circle is indicated with a solid black line.

To get velocity components in x and y directions (u and v), Equations B.21 & B.22 must be transformed back in Cartesian coordinates:

$$\phi = V_\infty \left(x + \frac{a^2 x}{x^2 + y^2} \right) \tag{B.23}$$

$$\psi = V_\infty \left(y - \frac{a^2 y}{x^2 + y^2} \right). \tag{B.24}$$

Combining these equations using Equation B.11 yields:

$$w\,(x,y) = V_\infty \left(x + \frac{a^2 x}{x^2 + y^2} \right) + i V_\infty \left(y - \frac{a^2 y}{x^2 + y^2} \right) \quad \Rightarrow \quad w\,(z) = V_\infty \left(z + \frac{R^2}{z} \right). \tag{B.25}$$

Differentiating Equation B.25 with respect to z then gives the velocities u & v:

$$\frac{\mathrm{d}w}{\mathrm{d}z} = u - iv \quad \Rightarrow \quad \frac{\mathrm{d}w}{\mathrm{d}z} = V_\infty \left(1 - \frac{a^2}{z^2} \right) \tag{B.26}$$

Next, the obtained flow over a circle is transformed to a flow over an ellipse using conformal mapping. The conformal mapping technique transforms potential lines and stream lines from the $z = x + iy$ plane to the $\zeta = \chi + i\eta$ plane, while maintaining the orthogonality between these lines. In Equation B.11 a function has to be chosen for ζ so that the circle is mapped to an ellipse described by:

$$\frac{x^2}{a^2} + \frac{y^2}{b^2} = 1, \tag{B.27}$$

where a is the semi-major axis of the ellipse and b the semi-minor axis. The candidate function for this is the Joukowski transformation function:

$$\zeta\,(z) = z + \frac{\lambda^2}{z}, \tag{B.28}$$

λ is the transformation parameter, and determines the resulting shape of the transformation. Rewriting this transformation to polar coordinates for a circle of radius R yields:

$$
\begin{aligned}
\zeta &= R\left(\cos\left(\theta\right) + i\sin\left(\theta\right)\right) + \frac{\lambda^2}{R\left(\cos\left(\theta\right) + i\sin\left(\theta\right)\right)} \\
&= R\left(\cos\left(\theta\right) + i\sin\left(\theta\right)\right) + \frac{\lambda^2}{R}\frac{\left(\cos\left(\theta\right) - i\sin\left(\theta\right)\right)}{\left(\cos^2\left(\theta\right) + \sin^2\left(\theta\right)\right)} \\
&= R\left(\cos\left(\theta\right) + i\sin\left(\theta\right)\right) + \frac{\lambda^2}{R}\left(\cos\left(\theta\right) - i\sin\left(\theta\right)\right) \\
&= \cos\left(\theta\right)\left(R + \frac{\lambda^2}{R}\right) + i\sin\left(\theta\right)\left(R - \frac{\lambda^2}{R}\right) = \chi + i\eta \\
&\Rightarrow \chi = \cos\left(\theta\right)\left(R + \frac{\lambda^2}{R}\right), \qquad \eta = \sin\left(\theta\right)\left(R - \frac{\lambda^2}{R}\right) \\
&\Rightarrow \cos\left(\theta\right) = \frac{\chi}{\left(R + \frac{\lambda^2}{R}\right)}, \qquad \sin\left(\theta\right) = \frac{\eta}{\left(R - \frac{\lambda^2}{R}\right)} \\
&\Rightarrow \cos^2\left(\theta\right) + \sin^2\left(\theta\right) = 1 \\
&\Rightarrow \frac{\chi^2}{\left(R + \frac{\lambda^2}{R}\right)^2} + \frac{\eta^2}{\left(R - \frac{\lambda^2}{R}\right)^2} = 1.
\end{aligned}
\tag{B.29}
$$

This expression describes an ellipse (see Equation B.27), with its semi-major axis a and semi-minor axis b related to circle diameter R and transformation parameter λ:

$$
a = R + \frac{\lambda^2}{R} \qquad b = R - \frac{\lambda^2}{R} \tag{B.30}
$$

For a desired ellipse with semi-major axis a and semi-minor axis b these two equations can be solved for the corresponding values of λ and R, which are needed to first calculate the potential flow over a circle (Equation B.25), and then do the actual conformal mapping of this solution to the desired ellipse (Equation B.28). An example of a Joukowski transformation of the circle in Figure B.2b is given in figure B.3.

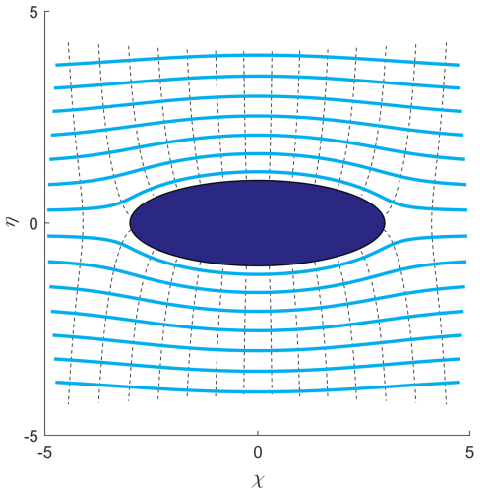

Figure B.3: Joukowski transformation of a circle to an ellipse. Dashed lines are potential lines, light blue lines are stream lines.

Because of the Joukowski transformation, z is now dependent of ζ, and Equation B.26 now is:

$$
\frac{\mathrm{d}w}{\mathrm{d}z}\frac{\mathrm{d}z}{\mathrm{d}\zeta} = \frac{\mathrm{d}w}{\mathrm{d}z}\frac{1}{\frac{\mathrm{d}\zeta}{\mathrm{d}z}} = V_\infty\left(\frac{1 - \frac{a^2}{z^2}}{1 - \frac{\lambda^2}{z^2}}\right) \tag{B.31}
$$

C

Example Meshes

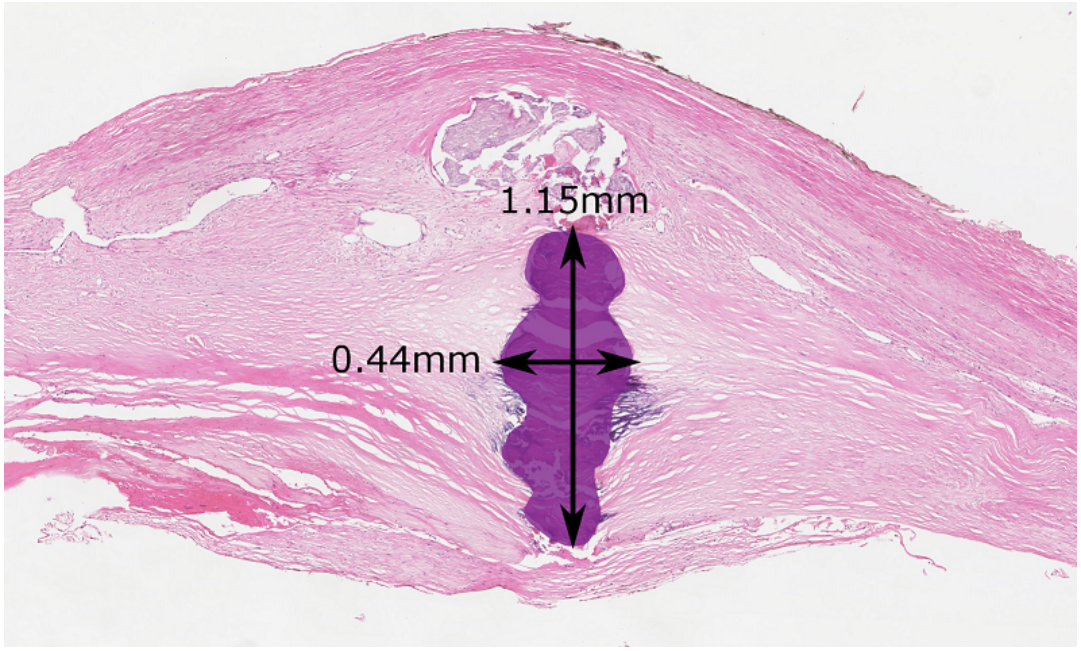

(a)

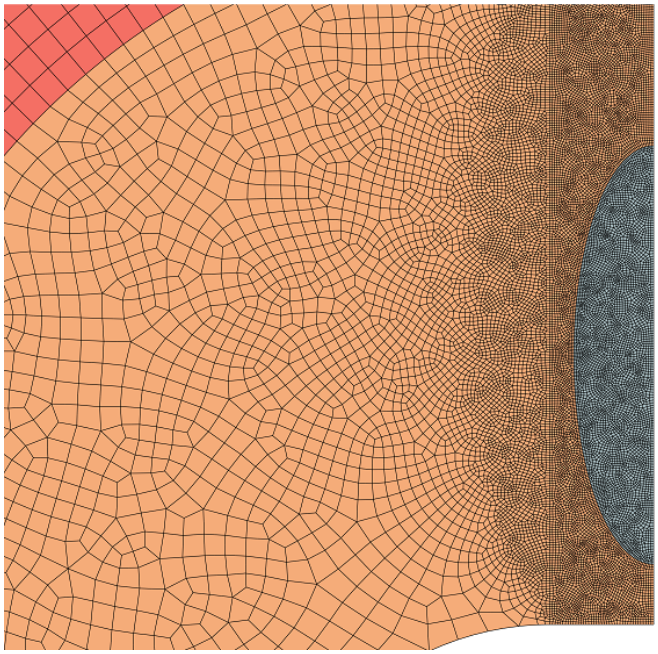

(b)

Figure C.1: Mesh of low aspect ratio calcification. a) histology image, b) mesh.

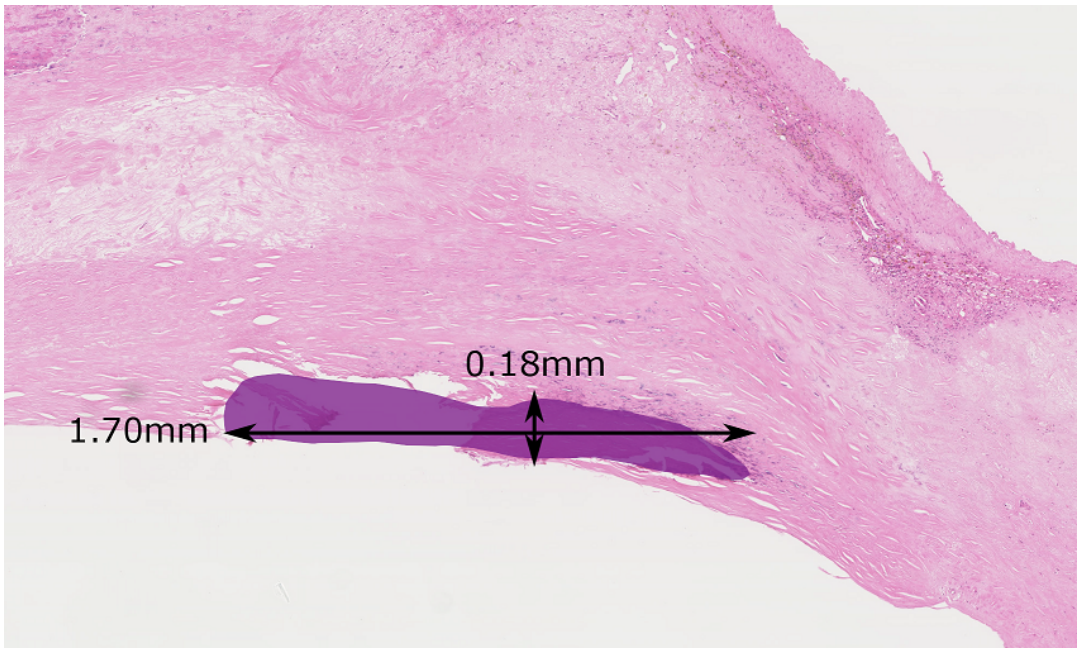

(a)

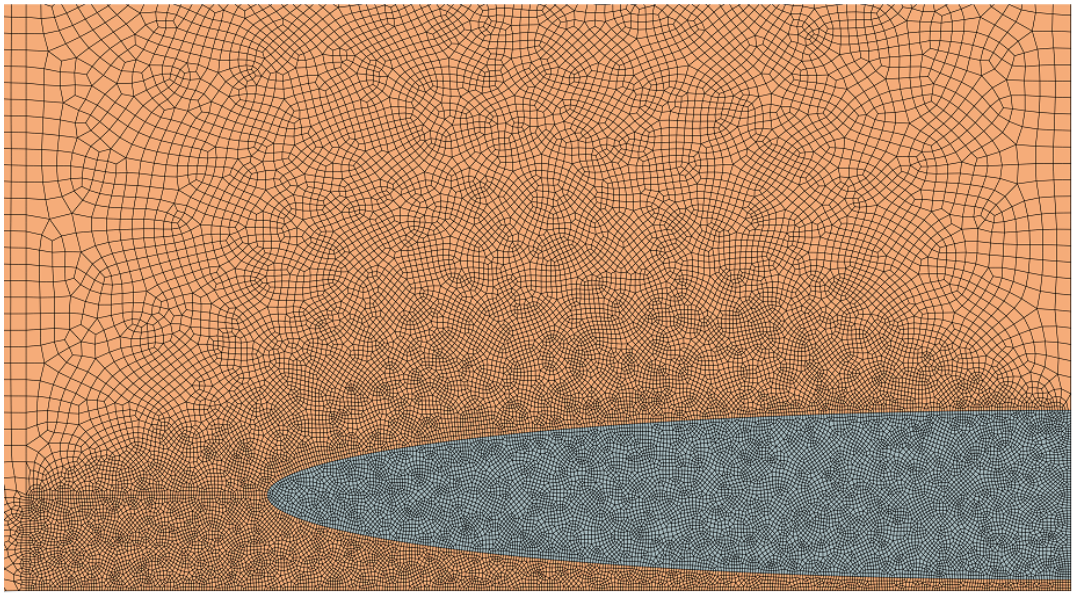

(b)

Figure C.2: Mesh of large aspect ratio calcification. a) histology image, b) mesh.

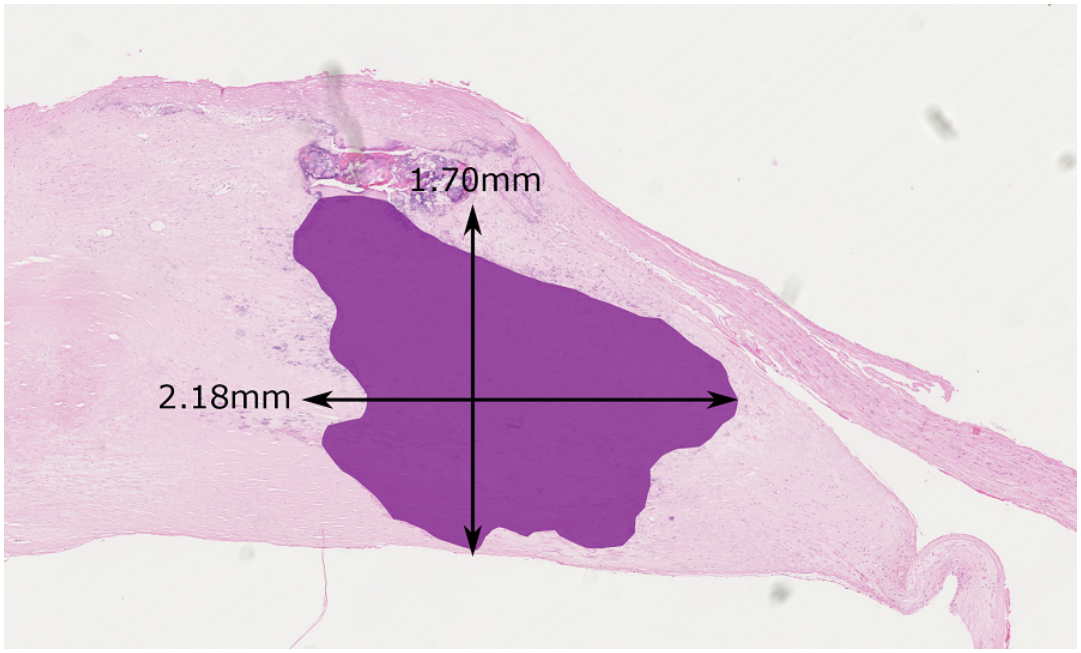

(a)

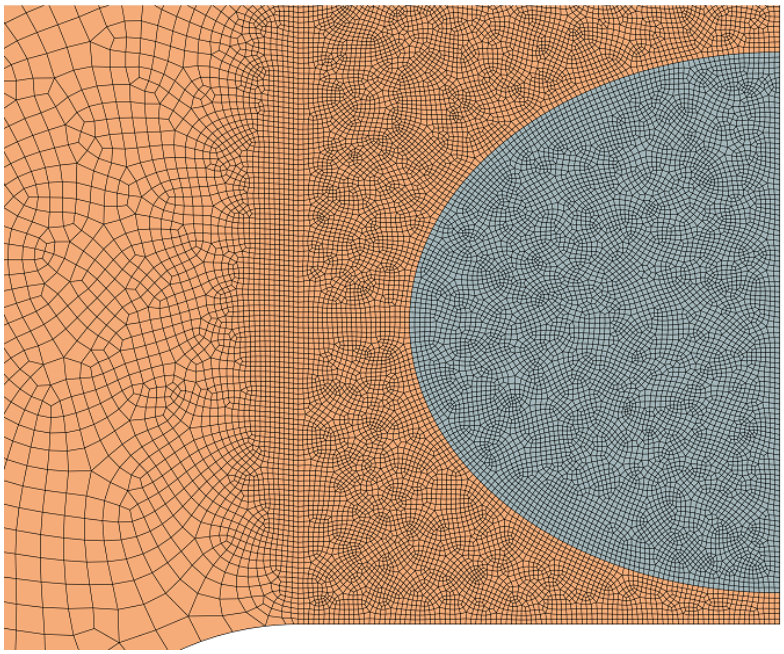

(b)

Figure C.3: Mesh of large size calcification. a) histology image, b) mesh.

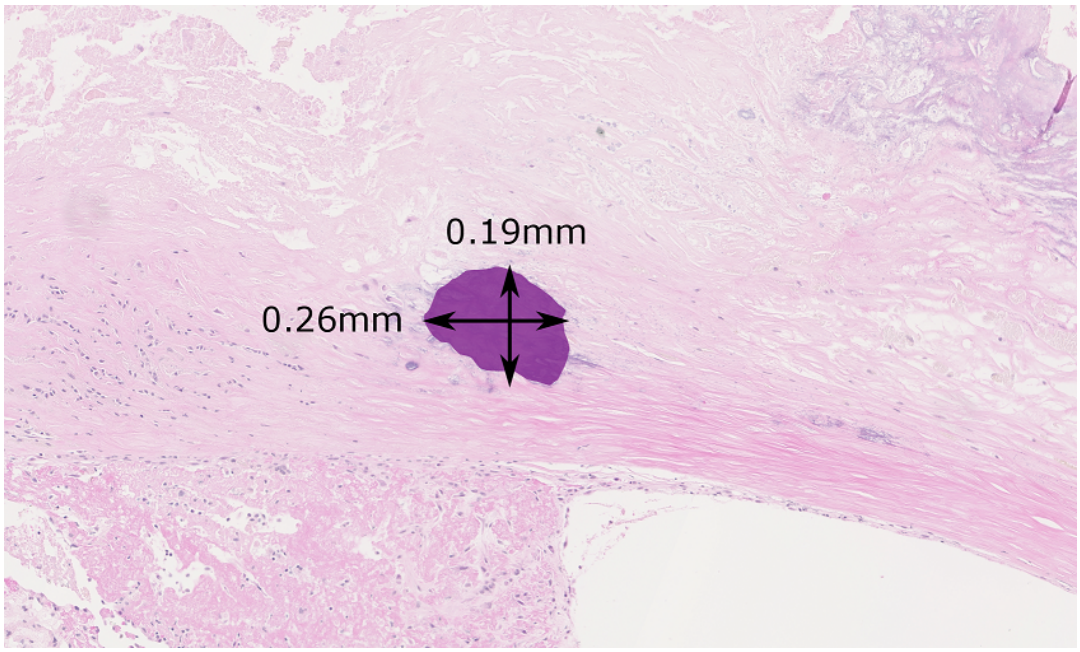

(a)

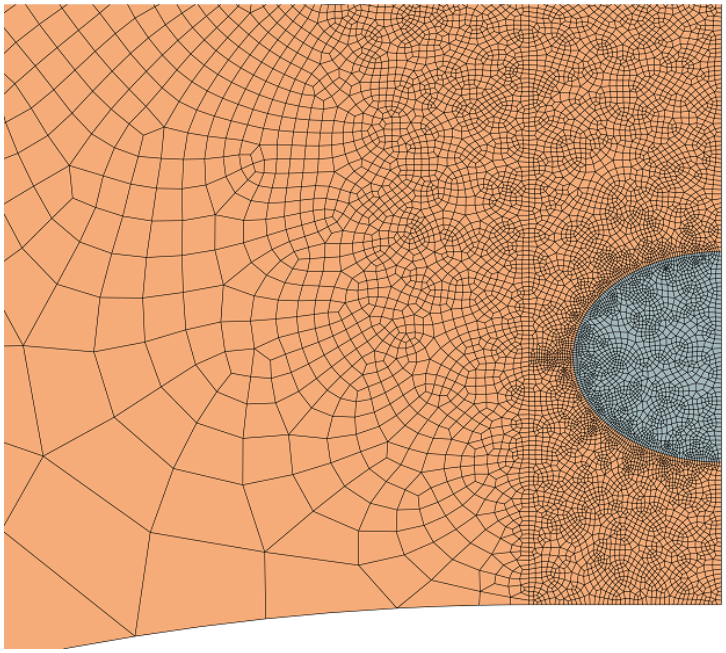

(b)

Figure C.4: Mesh of small size calcification. a) histology image, b) mesh.

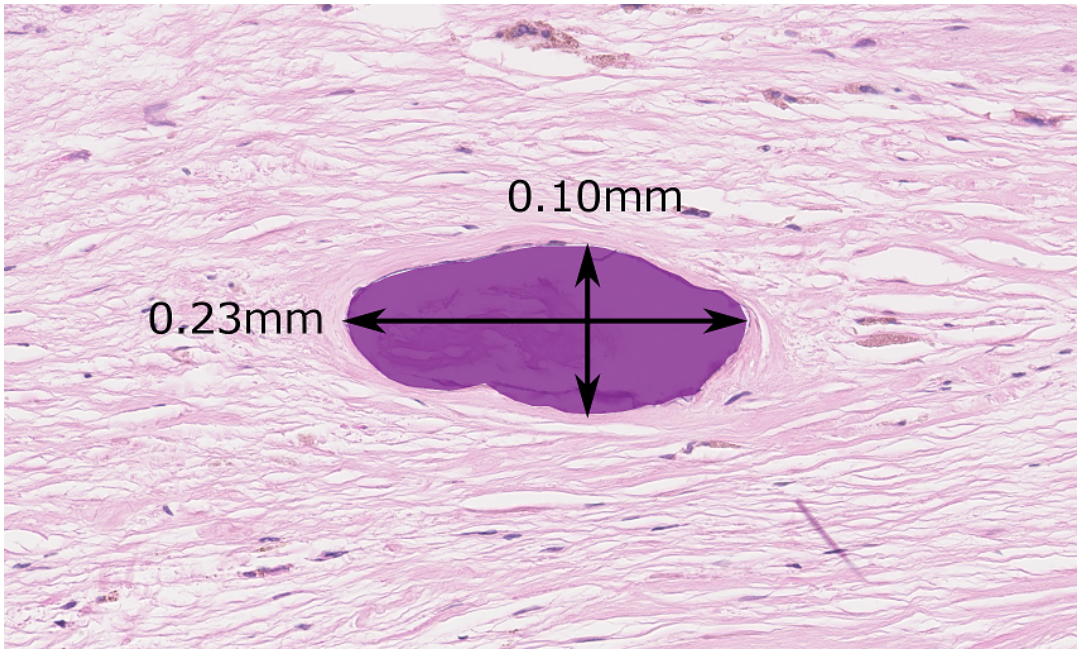

(a)

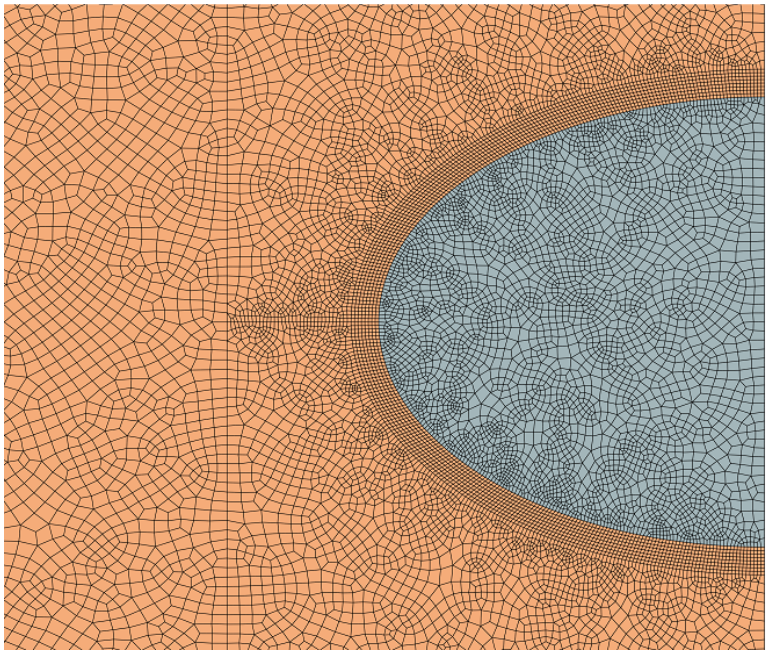

(b)

Figure C.5: Mesh of small size calcification with Encircling fiber pattern. a) histology image, b) mesh.